Generation of optical coherent state superpositions for quantum information processing

Tipsmark, Anders

Publication date:
2012

Document Version
Publisher's PDF, also known as Version of record

Generation of optical coherent state superpositions for quantum information processing

Supervisor
Professor, Ulrik L. Andersen FYS•DTU Quantum Information Group

March 2012

This thesis is submitted in partial fulfilment of the requirements for the Ph.D. degree at the Technical University of Denmark

Resume

I dette projektarbejde med titlen "*Generation of optical coherent state superpositions for quantum information processing*" har målet været at generere optiske kat-tilstande. Dette er en kvantemekanisk superpositions tilstand af to koherente tilstande med stor amplitude. Sådan en tilstand er interessant indenfor kvanteinformations behandling, da den, hvis den kan dannes tillader implementeringen af kvantekomputere udelukkende ved hjælp af lineære optiske komponenter.
Kat-tilstande kan tilnærmelsesvis genereres ved at trække en enkelt foton ud af en squeezed tilstand. En squeezed tilstand er en tilstand, hvor kvantestøjen er reduceret i en af de to kvadratur variable, amplitude eller fase. Dette gøres ved at sende intenst laserlys gennem en ikke-lineær krystal. Herved dannes der foton par ved spontan nedkonvertering, hvor en foton fra laseren spontant spalter i to fotoner med den halve energi. Herefter tappes en brøkdel, ca. 5%, af det genererede squezede lys, til en enkelt foton detektor, som når den detekterer en foton, laver en konditionel præparering af en kat-tilstand i det resterende lys.
Dette bliver så herefter karakteriseret ved hjælp af homodyn detektion, så man kan rekonstruere tæthedsmatricen og Wigner-funktionen, som er en grafisk representation af den generede kat-tilstand. Denne fremgangsmåde kan dog kun bruges til at preparere kat-tilstande med forholdsvis små amplituder. For virkeligt at kunne anvendes i kvanteinformatik kræver det kat-tilstande med større amplitude. Disse kan prepareres på forskellige måder. En metode er at trække flere fotoner ud af den squeezede tilstand. Denne fremgangsmåde er dog ikke praktisk da det vil give en drastisk reduktion i genereringfrekvensen.
I stedet udviklet har vi en ny metode, hvor vi tager 2 små kat-tilstande og kombinere dem for at lave en større. Denne kombination sker ved inteferens på en beamsplitter og efterfølgende måling af det ene output fra denne. Hvis resultatet af denne måling ligger indenfor et bestemt område vil det andet output være prepareret i en større kat-tilstand.
I denne afhandling er der arbejdet med de udfordringer, som er involveret i genereringen af disse tilstande. Der er gennemført en grundig analyse af effektiviteten af den

protokol, som ønskes anvendt til generering af kat-tilstande med små amplituder. Efter denne analyse en gennemgang af den mulige protokol, som kan bruges til at generere en større kat-tilstand fra 2 mindre tilstande. Dog blev denne protokol aldrig testet da fokus for projektet skiftede undervejs.
Protokollen til generering af små kat-tilstande blev dog implementeret og testet med succes. Kat-tilstande med fideliteter på mere end 50% blev demonstreret for kat-amplituder op til $\alpha \approx 1.3$. Samtidigt blev det demonstreret at tilstandende kunne opnå negative værdier, $W(0,0) \approx -0.05 \pm 0.01$ i fase-rums fordelingen, også kaldet Wigner funktionen, hvilket er et af de stærkeste beviser på kvante-naturen af de generede tilstande. Alle dele af protokollen blev grundigt testet eksperimentielt og optimeret med henblik på at realisere den succesfulde subtraktion af fotoner fra squeezede tilstande.
Efter den succesfulde implementering af dette blev en kvantegate baseret på disse kat-tilstande demonstreret. Dette var en Hadamard gate, som er en enkelt-mode gate, som kan rotere kvantetilstande "45°", og derigennem skifte mellem den linære og den diagonale basis. Denne rotation er ikke veldefineret for kat-tilstande, hvilket gør denne implementering af en Hadamard gate særlig, og ekstra udfordrende. Det lykkedes dog at opnå gennemsnitsfideliteter for gaten på $F \approx 70\%$ og dermed demonstrere den særlige kvante-natur af protokollen.
Til sidst blev en række mulige protokoller baseret på kat-tilstande præsenteret. Det drejer sig om en protokol til dæmpning af amplituden af en kat-tilstand, en protokol til "rengøring" af en "ødelagt" kat-tilstand og en protokol, som kan dreje en kat-tilstand over i en anden kat-tilstand. Alle disse protokoller er baseret på linære komponenter og Gaussiske målinger, hvilket gør dem ekstra interessante. Med disse protokoller kan en kat-tilstand manipuleres på måder, som potentielt gør det muligt at distribuere kat-tilstande over store afstande vha. fibre, hvilket kan have store muligheder i forhold til f.eks. kvantekommunikation eller distribueret kvantekomputation.

Acknowledgments

This thesis is the wistful conclusion to a remarkable, highly rewarding and at times very frustrating journey. A journey that has lasted not only the 3+ years of my PhD studies here at the Technical University of Denmark, DTU, but also the 5+ years spent here during my Master studies. Most of this time has been spent in and around the optical labs here at the Department of Physics. First, under the guidance of Professors Preben Buchhave and Peter Tidemand-Lichtenberg and finally under the guidance of Professor Ulrik L. Andersen, new group leader of the Quantum Optics Group.

The 7+ years spent working at the front line of, not only quantum optics, but experimental optics in general, have been both rewarding and frustrating, both on a professional and a personal level. I have learned more about quantum physics, lasers and optics in general than most people will, or intend to ever learn in a lifetime. I feel grateful for having had the opportunity to work at the forefront of quantum optics research and grateful for all the lively, challenging and enlightening discussions on various topics within physics. Everything, something that has enabled me to gain insight into the fundamental nature of quantum mechanics and learn about new ways to understand the world around us.

Many individuals have had a huge influence on my PhD studies here at DTU. Naming and thanking them all would result in a very long list, but a few deserve a special thank you:

First and foremost Ulrik, for agreeing to be my thesis supervisor. It has probably not always been easy but you have held out and survived these last 3 years with me. I am truly thankful for that. I would like you to know how much I appreciate you giving me this opportunity to explore one of the most intriguing aspects of the physical world. Superpositions is to me one of the most fascinating consequences of the quantum mechanical description of nature, and I have tremendously enjoyed being allowed to delve into this subject and learned a lot in the process. Finally I would like to thank you for your continued effort to motivate and inspire me to strive towards new goals and always providing me with brilliant (and sometimes insane!)

ideas.
Then a special thank you must also be given to Miroslav and Ruifang, for assisting me in the experimental work, and their great motivation to share their knowhow and experience and allowing me to learn from them. Without your assistance I do not think the experimental work would have gotten as far as it did during my three years here at DTU. Also, your continued dedication and inspiration have helped me stay motivated and enabled me to carry on through with my PhD studies. Finally a thank you and good luck must also be given to Amine, my fellow PhD student, who will carry on the torch in our lab. Thank you for keeping me on my toes and asking the good questions, and I wish you good luck with your final work towards you PhD degree.
I would also like to say thank you to our dedicated collaborators from around the world, especially at the Niels Bohr Institute at Copenhagen University, the Department of Optics at Palacký University in the Czech Republic and from the Max-Planck Institute at Erlangen University in Germany.
Finally I would like to thank all the extraordinary people from "the real world", who are also part of my life. Thank you for putting up with my frustrations, celebrations and boringly long explanations of my research area. Without you as part of my life outside the bubble here at DTU, the last three years would not have been as much fun as it has been. A special thank you to my very understanding family with whom I have shared many of both the positive and negative sides of being on this journey of personal and professional development.

Table of contents

Chapter 1

Introduction

Ever since the famous Schrödinger [1] and Einstein-Podolsky-Rosen [2] *Gedankenexperiments* the concept of quantum superpositions has been the topic of much debate and intense research [3]. The idea that a system can be in a state where, at the same time, it is in *both* one *and* another of two (or more) mutually exclusive states is fascinating, and from an everyday perspective highly perplexing. This is, however, a real effect in quantum mechanics and has been experimentally verified in both solid-state and optical systems. Such superpositions of macroscopic states are often referred to as Schrödinger Cat States in honor of the original proposal.
The possibility to have superpositions is what enables the implementation of certain quantum mechanical systems, which can perform information processing tasks, not tractable using classical systems. Computing [4], cryptography [5] and metrology [6] are just a few examples of information research areas where the quantum superposition can significantly enhance the performance compared to classical solutions.
The most advanced implementations of quantum algorithms have been realized using nuclear magnetic resonance techniques [7]. In these systems the information is encoded in mixed states and the measurements are across ensembles, meaning they are not ultimately scalable. Another option is systems with trapped ions, where high-fidelity two-qubit quantum gates have been implemented [8]. Also, solid-state systems such as q-dots and defects in diamonds have been investigated [9] and show promise of good scalability [10]. Today the most promising candidate for implementing multiple qubit operations on a chip is the superconducting flux qubits [11]. These systems all rely on some kind of solid-state physics. A different approach is to use optical systems to encode the information [12].
In optical systems the information can be encoded in the "external" degrees of freedom of individual photons. Single photons have certain advantages, that make them ideal for storing information. They can be well isolated from the environment, and

the manipulation and control can be achieved at the individual level. For single photons the most commonly used external degree of freedom to encode information is the polarization. Using this degree of freedom single mode gates can be readily implemented with simple phase plates and the two-mode quantum C-NOT gate has been implemented [13]. Moreover "macroscopic" 6- and 8-photon entanglement has been demonstrated [14, 15, 16]. The two-mode gate and entanglement for photons are, however, all realized in a probabilistic setting due to the lack of deterministic photon-photon interactions for the polarization degree of freedom.

Another way of encoding information in optical systems is to use the "internal" quadrature degree of freedom. Using this type of encoding quantum systems can be grouped into two approaches. The first is the Gaussian approach. This approach to quantum information processing, where all states and operations are Gaussian, is a matured research field. First, the preparation of squeezed states - the ubiquitous resource in many Gaussian protocols - has experienced large progress, resulting in states with high purity and high squeezing degrees [17, 18, 19, 20]. Second, Gaussian measurement projectors can be implemented using homodyne detection, which is capable of reaching near-unity detection efficiency [17]. Finally, practical implementations of operations such as displacement and feedback have been proposed and implemented [21, 22, 23, 24]. This progress has allowed for the implementation of Gaussian protocols, such as quantum teleportation, quantum key distribution, quantum cloning, quantum secret sharing and quantum computation [25, 26, 27, 28, 29, 30].

However, several no-go theorems exist for systems consisting of purely Gaussian operations. It has been proven that it is not possible to distill entanglement from Gaussian states using only Gaussian operations [31, 32, 33]. Quantum error correction using only Gaussian states and operations has also been deemed impossible for combating Gaussian noise [34]. Finally, Bell tests, universal quantum computing and quantum bit commitment have been proven impossible if only Gaussian states and operations are allowed [35, 36, 37, 38].

In order to realize the above mentioned protocols, non-Gaussian approaches are required. This non-Gaussianity can be injected into the system at different stages. It can enter through a non-Gaussian measurement strategy [39, 40, 41], non-Gaussian noise characteristics [42], or it can be incorporated through a non-Gaussian state preparation strategy [43, 44, 45, 46, 47, 48]. In the latter, instead of using squeezing as a resource for quantum protocols, certain pre-prepared non-Gaussian states are used as the resource. These non-Gaussian states can be either single-photons [49] or Coherent state superpositions (CSS) [50, 51].

In this thesis we report on the initial progress of our work towards the preparation of non-Gaussian states for quantum information processing. Our motivation for starting up work within this area of research is an expectation that it can provide new insight into the fundamentals of quantum mechanics. The goal of this work is to successfully implement the subtraction protocol [52] to prepare the small amplitude coherent state superposition (CSS). Once successful at this, different routes can be pursued. One goal is to "build" CSS's with larger amplitude using small amplitude CSS's as the resource [44]. Another goal is to attempt the implementations of quantum gates based on the CSS's as the resource.

This thesis is organized as follows. In Ch. 2 we start out with a brief review of quantum optics theory. Then in Ch. 3 we do a thorough investigation of the system intended to prepare the small and large amplitude CSS's. In Chs. 4 and 5 we will present a detailed discussion on the experimental system built so far and the first experimental tests performed on the system. In Ch. 6 we present and discuss the experimental implementation of a Hadamard gate for CSS's. Finally, in Chs. 7 and 8 we present theoretical investigations of new protocols based on CSS's and discuss potential directions for further research.

Chapter 2

Theory of quantum optics

Preparing coherent state superpositions is a non-trivial task. In order to establish the foundations for a thorough presentation and discussion of our current progress towards the generation of large-amplitude CSS's, we will start with a brief review of quantum optics theory.
We start by establishing how to treat quantum states. We do this by first presenting different ways of representing states in quantum optics. We will also present the quantum mechanical description of the optical field, the quantum mechanical harmonic oscillator. After this, a discussion of the consequences of this description will be presented by describing various states of the harmonic oscillator.
Following this we will present the primary process of most quantum optics experiments. Today non-linear frequency conversion of coherent fields is used to prepare the initial states of most experiments involving non-classical effects. Finally we will present a review of techniques for establishing the quantum nature of the light, by presenting different detection and characterization techniques regularly utilized in quantum optics.

2.1 Describing a quantum state

In quantum optics a number of different ways to represent the state of the optical field is utilized. There is a one-to-one correspondence between them, and which one to use is most often determined by the task at hand. They all have some benefits that will make them practical in certain applications.

2.1.1 Density matrix formalism

The standard way to describe a quantum state existing in a Hilbert space, $\mathbb{H}$, is through the Dirac bracket-notation, $|\psi\rangle$. In this formalism a pure state is easily identifiable, since it can be written as a single ket, which again can be expanded as a superposition across a complete orthonormal basis, [53, 54],

$$|\psi\rangle = \sum_n c_n |\varphi_n\rangle . \tag{2.1}$$

$$\langle\varphi_n|\ \varphi_m\rangle = \delta_{nm},\ \sum_n |\varphi_n\rangle\langle\varphi_n| = \mathbb{1}, \tag{2.2}$$

This superposition can be thought of as a superposition of basis vectors, $\{|\varphi_n\rangle\}$, spanning the complete system in which the state-ket, $|\psi\rangle$, is existing. The expectation value of an observable on the system represented by the operator, $\hat{A}$, can be found by the inner matrix product with the state,

$$\left\langle \hat{A} \right\rangle = \langle\psi| \hat{A} |\psi\rangle \tag{2.3}$$

$$= \sum_{n,m} c_n^* c_m \langle\varphi_n| \hat{A} |\varphi_m\rangle . \tag{2.4}$$

If the Hamiltonian, $\hat{H}$, governing the system is time-independent, the time evolution of a quantum state is given by the unitary operator, $\hat{U}(t) = e^{-i\hat{H}t/\hbar}$, $|\psi(t)\rangle = \hat{U}(t)|\psi(0)\rangle$. For the remainder of the theoretical part, for simplicity, we will make the definition $\hbar = 1$, which has no practical consequences. The quantum state in Eq. 2.1 was existing in a single Hilbert space. Often quantum states exist in a Hilbert space, which in itself consists of multiple sub-Hilbert spaces, $\mathbb{H}_1,\ \mathbb{H}_2, ...$ In this case the full Hilbert space can be expressed as a tensor product of the constituting Hilbert spaces, $\mathbb{H} = \mathbb{H}_1 \otimes \mathbb{H}_2 \otimes ....$ Equivalently, the state ket of a quantum state existing in the larger Hilbert space, can be decomposed into state kets existing in the lower Hilbert spaces,

$$|\psi\rangle = \sum_n a_n |\varphi_n\rangle \tag{2.5}$$

$$= |\psi\rangle \otimes |\sigma\rangle \tag{2.6}$$

$$= \sum_k b_k |\varphi_k\rangle \otimes \sum_m c_m |\lambda_m\rangle , \tag{2.7}$$

where $|\varphi_n\rangle = |\varphi_k\rangle \otimes |\lambda_m\rangle$ are the eigenvectors spanning the larger Hilbert space. Sometimes a quantum state cannot be expressed as in Eq. (2.6) even though it is expressed as in Eq. (2.5). Such a state is said to be entangled.

A more general description of quantum states in the Dirac bracket-notation is that of density operators. In this description a quantum state is generally thought of as being in a mixture of multiple pure states. To describe this we use the notion of a density operator, $\hat{\rho}$,

$$\hat{\rho} \quad = \quad \sum_{n,m} a_{n,m} \left|\varphi_n\right\rangle \left\langle\varphi_m\right| , \tag{2.8}$$

where $a_{n,m}$ are the expansion coefficients, and $\left|\varphi_n\right\rangle \left\langle\varphi_m\right|$ can be thought of as the matrix extension of the eigenvectors in Eq. (2.1). It can be proven that a physically acceptable density operator must satisfy the conditions [54],

$$\mathrm{Tr}\hat{\rho} \;=\; 1 \qquad \Rightarrow \qquad \sum_n \rho_n \;=\; 1, \tag{2.9}$$

$$\hat{\rho} \;=\; \hat{\rho}^\dagger \qquad \Rightarrow \qquad \rho_n \;=\; \rho_n^*, \tag{2.10}$$

$$\left\langle v\right| \hat{\rho} \left|v\right\rangle \;\geq\; 0 \;\text{ for all }\; \left|v\right\rangle \qquad \Rightarrow \qquad \rho_n \;\geq\; 0, \tag{2.11}$$

where ρ_n are the eigenvalues of $\hat{\rho}$. From these requirements it can also be proven that physically acceptable density operator can always be diagonalized into some basis,

$$\hat{\rho} \quad = \quad \sum_n \rho_n \left|\lambda_n\right\rangle \left\langle\lambda_n\right| . \tag{2.12}$$

This can be thought of as a weighted sum of probabilities across multiple pure states, where the weights are given by the eigenvalues of the density operator. From this it is also seen that a density operator with only one eigenvalue, $\rho_n = 1$ for one particular n, is in itself a pure state. From Eqs. (2.9) to (2.12) it can also be proven that $\mathrm{Tr}\hat{\rho}^2 \leq 1$, with a pure state saturating the inequality. The equivalent of Eq. (2.3) for a density operator is [55],

$$\left\langle \hat{A} \right\rangle \quad = \quad \mathrm{Tr}(\hat{A}\hat{\rho}). \tag{2.13}$$

Using Eqs. (2.3) and (2.12) it can be shown that the expectation value will just be the weighted average of expectation values for the individual pure states, equivalent to (2.12). The similarity between two quantum states, also called the fidelity, is generally given by [56],

$$F(\hat{\rho}_1, \hat{\rho}_2) \quad = \quad \left(\mathrm{Tr}\left[\sqrt{\sqrt{\hat{\rho}_1}\hat{\rho}_2\sqrt{\hat{\rho}_1}} \right] \right)^2 . \tag{2.14}$$

This expression is however not normally used. We are often interested in the similarity between a prepared state, $\hat{\rho}$ and a pure state, $|\varphi\rangle$, which ideally should be prepared by the implemented process. In this case the fidelity is found simply by the inner matrix product of the two states,

$$F(\hat{\rho}_1, |\varphi\rangle\langle\varphi|) \quad = \quad \mathrm{Tr}(|\varphi\rangle\langle\varphi|\,\hat{\rho}_1) \;=\; \langle\varphi|\,\hat{\rho}_1\,|\varphi\rangle\,. \tag{2.15}$$

2.1.2 The wave function

From [54, 57] we know that the Hamiltonian describing the optical field is equivalent to the one for a quantum-mechanical harmonic oscillator,

$$\hat{H} \quad = \quad \frac{1}{2}(\hat{x}^2 + \hat{p}^2), \tag{2.16}$$

where $\hat{x}, \hat{p}$ are the dimensionless Hermitian operators attributed to position and momentum. These operators satisfy the commutation relation $[\hat{x}, \hat{p}] = i$. Since these operators do not commute, the observables they represent cannot be simultaneously determined to arbitrary precision. They are said to be conjugate variables of the harmonic oscillator and must satisfy the uncertainty relation,

$$\langle(\Delta\hat{x})^2\rangle\langle(\Delta\hat{p})^2\rangle \quad \geq \quad \frac{|[\hat{x}, \hat{p}]|}{4} \;=\; \frac{1}{4} \tag{2.17}$$

which is usually referred to as Heisenberg's uncertainty relation. The operators have a corresponding set of eigenstates, fulfilling, $\hat{x}\,|x\rangle = x\,|x\rangle\,, \quad \langle x'|\,x\rangle = \delta(x' - x)$ and, equivalently, for $\hat{p}$. Both of these sets are complete

$$\int_{-\infty}^{\infty} |x\rangle\langle x|\,dx \;=\; \mathbb{1} \quad \vee \quad \int_{-\infty}^{\infty} |p\rangle\langle p|\,dp, \tag{2.18}$$

so they meet the same requirements as given in Eq. (2.2). The only difference being that now the variable is continuous as opposed to the discrete case earlier. Also, we know that $|x\rangle$ and $|p\rangle$ are related through the Fourier transform [58],

$$|p\rangle \;=\; \frac{1}{\sqrt{2\pi}} \int_{-\infty}^{\infty} |x\rangle\, e^{ixp} dx. \tag{2.19}$$

For the electric field the position and momentum operators can be interpreted as describing the amplitude, $\hat{x}$, and the momentum, $\hat{p}$. These two variables are often called quadrature variables and satisfy the same restrictions as the position and momentum for a harmonic oscillator. We can also imagine being in a rotated frame

relative to x and p, in which we can define a new set of quadrature operators,

$$\hat{q}_\theta \quad = \quad \cos\theta\hat{x} + \sin\theta\hat{p}, \tag{2.20}$$

where θ is the angle of the rotated frame with respect to the x direction of the old frame. Often $\hat{q}_\theta$ is used to refer to a general quadrature variable as is the case in Eq. (2.20) and also for the remainder of this work. For the harmonic oscillator it is often also useful to define a set of non-Hermitian operators

$$\hat{a} \;=\; \frac{\hat{x} + i\hat{p}}{\sqrt{2}} \quad \vee \quad \hat{a}^\dagger \;=\; \frac{\hat{x} - i\hat{p}}{\sqrt{2}}, \tag{2.21}$$

with $[\hat{a}, \hat{a}^\dagger] \;=\; 1$, and a hermitian operator $\hat{n} \;=\; \hat{a}^\dagger\hat{a} \;=\; 1/2(\hat{x}^2 + \hat{p}^2 - 1)$. Using this we can find a set of eigenstates for the Hamiltonian in Eq. (2.16). We denote these eigenstates by the kets, $|n\rangle\,, \;\; n \;=\; 0, 1, 2, ...$, and they fulfill the conditions

$$\hat{a}\,|n\rangle \;=\; \sqrt{n}\,|n-1\rangle\,, \;\; \hat{a}^\dagger\,|n\rangle \;=\; \sqrt{n+1}\,|n+1\rangle\,, \;\; \langle m|\,n\rangle \;=\; \delta_{mn}. \tag{2.22}$$

Since these states are orthonormal eigenstates of the Hamiltonian, they all have different energies. The energy of the individual states is proportional to n. For this reason n is often also called the excitation of the harmonic oscillator. The full energy spectrum for the harmonic oscillator can be found to be, $E_n \;=\; n+1/2$. From this it is clear how the optical field can be interpreted as a harmonic oscillator. A light field can be excited by any discrete number of photons, $|n\rangle$, and the energy of the light field is proportional to the number of photons, $E_n \;\propto\; n$. However, we can see that even if no photons are left in the state, some energy, $E_0 \;=\; 1/2$, still remains. This is a result of the uncertainty relation, (2.17). These eigenstates of the Hamiltonian, $|n\rangle$, are called Fock states when dealing with the optical field, and are typically the states of choice when expressing the quantum state in the density matrix formalism

$$\hat{\rho}_{opt} \quad = \quad \sum_{nm} a_{nm}\,|n\rangle\,\langle m|\,. \tag{2.23}$$

Given a certain density operator representing a state of the optical field, it is possible to define a probability density for the quadrature operator,

$$\mathrm{pr}_\theta(q) \quad \equiv \quad \langle q_\theta|\,\hat{\rho}\,|q_\theta\rangle \;=\; \sum_{nm} a_{nm}\,\langle q_\theta|\,n\rangle\,\langle m|\,q_\theta\rangle \tag{2.24}$$

where $\langle q_\theta |\, n\rangle \equiv \psi_n(q)_\theta$ is called the wave function for the n-photon Fock state. Its mathematical expression can be shown to be [1]

$$\psi_n(q)_\theta = \frac{1}{\sqrt{\sqrt{\pi}2^n n!}} H_n(q) e^{-\frac{1}{2}q^2} e^{-i\theta\left(n+\frac{1}{2}\right)} \tag{2.25}$$

where $H_n(x)$ is the Hermite polynomial of n'th order. Using this it can be proven that the Fock states satisfy the uncertainty relation, Eq. (2.17),

$$\langle (\Delta\hat{q}_\theta)^2 \rangle = \int_{-\infty}^{\infty} q^2 |\psi_n(q)_\theta|^2 dq = n + \frac{1}{2}. \tag{2.26}$$

This does not depend on the phase θ, meaning $\langle (\Delta\hat{q}_\theta)^2 \rangle = \langle (\Delta\hat{x})^2 \rangle = \langle (\Delta\hat{p})^2 \rangle$. From this it is easily verified that the Fock states satisfy the uncertainty relation, with the lowest Fock state, the vacuum state $|n = 0\rangle$, fulfilling the equality. Such a state is typically called a minimum uncertainty state.

2.1.3 Phase space and the Wigner quasi-probability distribution

We know from ordinary mechanics that the state of a harmonic oscillator, x and p, at a given time can be represented by a point in phase space [59]. The temporal evolution of the harmonic oscillator can then be described by the propagation of this point around in space, typically in circles if no damping or driving is present. However, from Eq. (2.17) we have that conjugate quadratures of a harmonic oscillator, $\hat{x}$ and $\hat{p}$, cannot be simultaneously well-defined with arbitrary precision. For this reason the state of the oscillator in phase space can no longer be described by a single point, but would have to be described by a continuum of points around the central expectation value. The situation is sketched in Fig. 2.1. The radius of the disc is typically thought of as the uncertainty on the observable $\sqrt{\langle (\Delta\hat{q}_\theta)^2 \rangle}$, which means that the area will then be given by Eq. (2.17). This is the ultimate precision with which we can determine the phase space position of a quantum mechanical harmonic oscillator. It turns out that this extension of the definition of phase space is quite practical. It allows a nice graphical way to present quantum states and illustrates features, which can be quite difficult to intuitively see in the density matrix formalism. The disc in phase space is the cross section of a function known as the Wigner quasi-probability distribution after E. Wigner who first proposed it in 1932

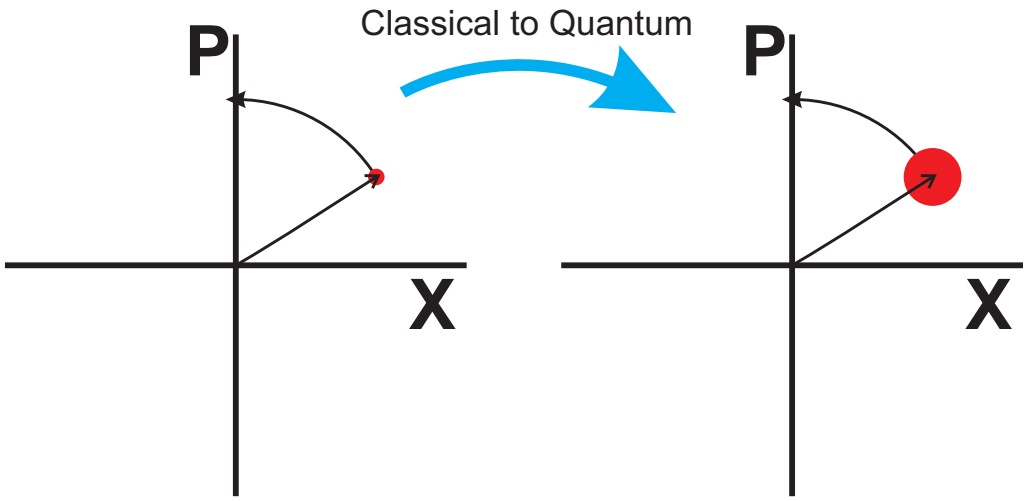

Fig. 2.1: The concept of phase space for classical and quantum mechanics. In classical mechanics the amplitude and phase of a harmonic oscillator can be known simultaneously to arbitrary precision illustrated by a single point. In quantum mechanics this is fundamentally prevented, so the best precision we can achieve is a disc around a certain center point.

[60]. The formal definition is given by

$$W(x,p) \quad = \quad \frac{1}{\pi}\int_{-\infty}^{\infty} \langle x-y|\,\hat{\rho}\,|x+y\rangle\, e^{2ipy}dy. \tag{2.27}$$

The definition in Eq. (2.27) can be shown to fulfill the conditions for being accepted as a phase space distribution [61, 62],

$$\int_{-\infty}^{\infty}\int_{-\infty}^{\infty} W(x,p)dxdp \quad = \quad \mathrm{Tr}\hat{\rho} \;=\; 1, \tag{2.28}$$

$$\int_{-\infty}^{\infty} W(q_\theta, q_{\theta+\pi/2})dq_{\theta+\pi/2} \quad = \quad \langle q_\theta|\,\hat{\rho}\,|q_\theta\rangle \;\equiv\; \mathrm{pr}(q_\theta). \tag{2.29}$$

Using this and Eq. (2.15) it can be shown that the fidelity between two quantum states is simply the overlap integral of their respective Wigner distributions if, and only if, one of the states is a pure state. To the best of our knowledge, no direct equivalent to Eq. (2.14) exists for Wigner distributions [63]. A special case of the overlap integral is the expectation value of an operator, Eq. (2.13), $\left\langle \hat{A} \right\rangle \;=\; 2\pi\int_{-\infty}^{\infty} W(x,p)W_A(x,p)dxdp$ where $W_A(x,p)$ is the "Wigner-distribution" for the operator $\hat{A}$. We can also find the general expression for a Wigner distribution belonging to a quantum state given by Eq. (2.23), as this will come in handy later in this work. Inserting Eq. (2.23) into Eq. (2.27) and using (2.25) it can be shown

that $W_{\hat{\rho}}(x,p) = \sum_{n,m} a_{nm} W_{nm}(x,p)$ with [64, 65],

$$W_{nm}(x,p) = \begin{cases} \frac{1}{\pi} e^{-x^2-p^2} (-1)^m (ip-x)^{m-n} \sqrt{2^{m-n} \frac{n!}{m!}} L_n^{m-n}(2x^2+2p^2), & m \geq n \\ \frac{1}{\pi} e^{-x^2-p^2} (-1)^m (ip+x)^{n-m} \sqrt{2^{n-m} \frac{m!}{n!}} L_m^{n-m}(2x^2+2p^2), & m < n \end{cases} \quad (2.30)$$

where L_k^α are the associated Laguerre polynomials.
The Wigner distribution is usually referred to as a quasi-probability distribution. The reason for this being, that it is in no way restricted to positive values everywhere in phase space. This is in contradiction to the classical understanding of a probability distribution, where negative probabilities are not conceivable. But nevertheless, this is a consequence in quantum mechanics. And using Eqs. (2.30), (2.9) and (2.11) we can easily verify that these negative values can indeed be seen. All we have to do is to evaluate the value of the Wigner distribution in the origin, $W(0,0)$,

$$W(0,0) = \frac{1}{\pi} \sum_n (-1)^n a_{nn} \quad (2.31)$$

Since $0 \leq a_{nn} \leq 1$, $\sum_n a_{nn} = 1$ the value at the origin can be anywhere in the range $[-1/\pi : 1/\pi]$.

2.2 States of the optical field

In Sec. 2.1.2 we saw how the optical field could be described by a quantum mechanical harmonic oscillator. This also means that the states of the harmonic oscillator can be reproduced in the optical field. In this section we will provide a review of some of the most common states of the harmonic oscillator. These states can roughly be categorized in three groups; the pure Gaussian states, the pure non-Gaussian states and an intermediate region of impure states which can be either Gaussian or non-Gaussian. Of the two pure types, the Gaussian states are the simplest to realize in a quantum optics laboratory, since only second-order nonlinearities are needed to prepare these. This is in opposition to the preparation of pure non-Gaussian states, which is a highly non-trivial task, requiring access to at least a third-order nonlinearity [62, 30]. The intermediate region of impure states can be either trivial or non-trivial mixtures of Gaussian states.

2.2.1 Gaussian states

The coherent state

The simplest of the pure Gaussian states is the coherent state. It is defined as the eigenstate of the annihilation operator $\hat{a}$, Eq. (2.21), $\hat{a}\,|\alpha\rangle = \alpha\,|\alpha\rangle$. Here, $\alpha = |\alpha|e^{i\varphi}$ is called the complex amplitude. Following this definition it can be shown to be the superposition of Fock states given by [57]

$$|\alpha\rangle = e^{-\frac{|\alpha|^2}{2}} \sum_{n=0}^{\infty} \frac{\alpha^n}{\sqrt{n}} |n\rangle\,. \tag{2.32}$$

$$\hat{\rho}_\alpha = e^{-|\alpha|^2} \sum_{n,m} \frac{\alpha^n (\alpha^*)^m}{\sqrt{n!m!}} |n\rangle\langle m|\,, \tag{2.33}$$

From the last line it is seen that the photon number distribution given by the diagonal elements is Poissonian with a mean photon number $\langle \hat{n} \rangle = |\alpha|^2$. Finding the Wigner function, it becomes obvious why the coherent state is called a Gaussian state,

$$W_\alpha(x,p) = \frac{1}{\pi} e^{-(x-x_0)^2-(p-p_0)^2}, \quad \alpha = \frac{x_0 + ip_0}{\sqrt{2}}. \tag{2.34}$$

This is a symmetric Gaussian function centered at (x_0, p_0). The noise in x, p, and any rotated coordinate system can be shown to be $\mathrm{Var}(x) = \mathrm{Var}(p) = 1/2$. Therefore the coherent state minimizes Eq. (2.17) and is thus a minimum uncertainty state, regardless of α. For this reason $|\alpha\rangle$ is usually interpreted as the quantum mechanical analog of the classical phase space point, meaning it can be represented by the disc shown in Fig. 2.1. From Eq. (2.32) an operator with the property $\hat{D}(\alpha)\,|0\rangle = |\alpha\rangle$ can also be defined. An operator that takes the vacuum state $|0\rangle$, and translates it into a coherent state with an amplitude α,

$$\hat{D}(\alpha) = e^{\alpha\hat{a}^\dagger - \alpha^*\hat{a}} \tag{2.35}$$

This operator can easily be verified to be unitary; $\hat{D}^\dagger\hat{D} = \mathbb{1}$.

The squeezed state

The Wigner distribution,

$$W_r(x,p) = \frac{1}{\pi} e^{-(e^{-r}x - x_0)^2 - (e^r p - p_0)^2} \tag{2.36}$$

is still a Gaussian shaped bell fulfilling Eq. (2.17), $\mathrm{Var}(\hat{x})\mathrm{Var}(\hat{p}) = 1/4$, although having a different peak position, $(x_0 e^r, p_0 e^{-r})$. The main difference is that the shape of the Gaussian bell is no longer symmetric, but has been stretched in one direction and squeezed in the orthogonal direction. As it turns out, the quantum state described by this Wigner distribution is an acceptable physical state, also called the single-mode squeezed state. Its Fock state expansion can be shown to be, for $\alpha = x_0 = p_0 = 0$,

$$|\zeta\rangle = \frac{1}{\sqrt{\cosh(r)}} \sum_{n=0}^{\infty} \frac{\sqrt{(2n)!}}{n!} \left[-\frac{1}{2} e^{i\nu} \tanh(r)\right]^n |2n\rangle , \tag{2.37}$$

where $\zeta = re^{i\nu}$ is called the squeezing parameter, with $r \geq 0$ and $\nu \in [0 : 2\pi[$ being the squeezing strength and direction, respectively. Finding the variances of the quadrature variables, $\mathrm{Var}(x) = e^{2r}/2$ and $\mathrm{Var}(p) = e^{-2r}/2$, we see that the squeezed state saturates the uncertainty relation and is thus, as the coherent state, a minimum uncertainty state. The noise has just been shifted around. As for the coherent state, an operator can be derived, which will take a vacuum state into a squeezed state, $\hat{S}(\zeta) = e^{1/2\zeta(\hat{a}^\dagger)^2 - 1/2\zeta^* \hat{a}^2}$. Although this operator does not commute with the displacement operator, any pure Gaussian state can be reached from the vacuum state by applying these two operators,

$$\begin{aligned} |\alpha, \zeta\rangle &= \hat{D}(\alpha)\hat{S}(\zeta)\,|0\rangle , \\ \hat{\rho}_{\alpha,\zeta} &= |\alpha, \zeta\rangle\,\langle\alpha, \zeta| \end{aligned} \tag{2.38}$$

This state can be uniquely described by only its first and second order moments, i.e. its position in phase space (x_0, p_0) and its variances $\mathrm{Var}(x), \mathrm{Var}(p)$.

Gaussian mixtures

The coherent state and the single-mode squeezed state are examples of pure states as they satisfy $\mathrm{Tr}[\hat{\rho}^2] = 1$. However, often mixtures are of interest, since these tend to be what exists in the lab[1]. Any combination of Gaussian states is a physical acceptable state itself, provided [67]

$$\hat{\rho}_G = \int G(\alpha, \zeta)\,|\alpha, \zeta\rangle\,\langle\alpha, \zeta|\,d\alpha d\zeta, \qquad \int G(\alpha, \zeta) d\alpha d\zeta = 1, \tag{2.39}$$

[1]The coherent state can be prepared to within statistical precision and pure squeezed states have been demonstrated [66].

where $G(\alpha,\zeta) = G(|\alpha|,\varphi,r,\nu)$ is a weight distribution. This distribution can have a more or less involved expression. Two of the more commonly appearing mixtures are the thermal state with a mean number of photons $(\Delta|\alpha|)^2/2$,

$$G(|\alpha|,\varphi) = \frac{1}{2\pi^{3/2}(\Delta|\alpha|)} e^{-|\alpha|^2/(\Delta|\alpha|)^2}, \tag{2.40}$$

and the phase diffused coherent state with amplitude $|\beta|$ and phase diffusion $f(\varphi)$,

$$G(|\beta|,\varphi) = \delta(|\beta|-|\alpha|)f(\varphi). \tag{2.41}$$

A simpler form of Eq. (2.39) was first presented by E. Sudarshan [68] and R. Glauber [69], with only the coherent states as the basis,

$$\hat{\rho} = \int P(\alpha)\,|\alpha\rangle\langle\alpha|\,d^2\alpha, \tag{2.42}$$

since the coherent states satisfy a closure relation. The Wigner distributions for both the coherent state, Eq. (2.34), the squeezed vacuum state, Eq. (2.37), and the Gaussian mixtures, Eqs. (2.41) and (2.40), are plotted in Fig 2.2. In the Wigner dis-

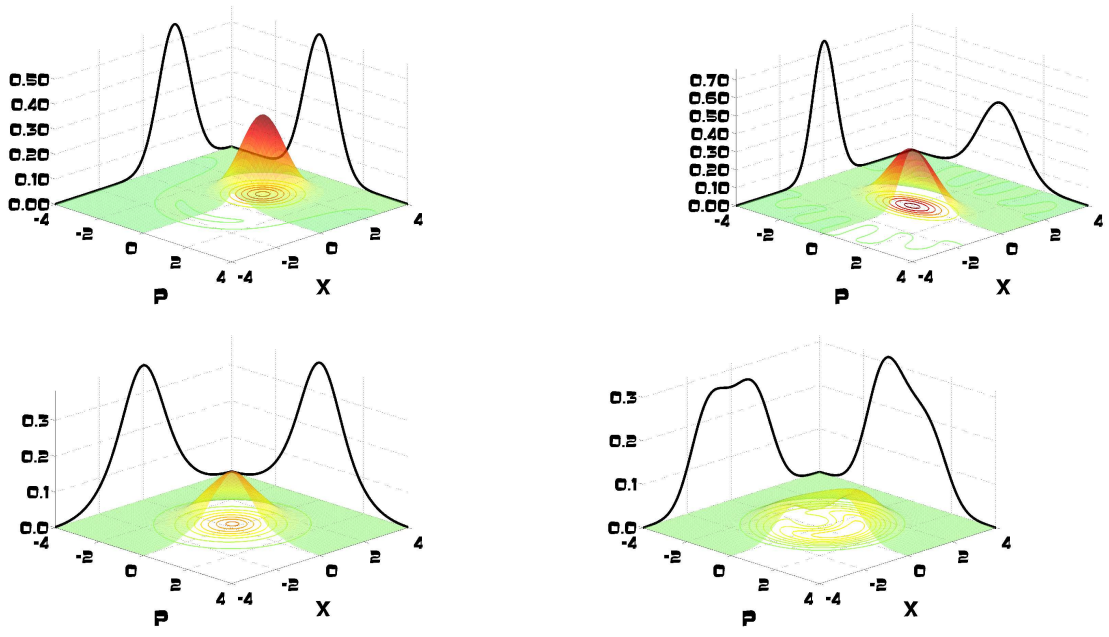

Fig. 2.2: Wigner distributions for a coherent state, a squeezed, a thermal state and a phase diffused coherent state.

tributions the Gaussian shaped bells for the coherent, squeezed and thermal states

are clearly seen. However, the phase diffused coherent state clearly cannot be described by a Gaussian Wigner distribution as the ones given in Eqs. (2.34) or (2.36). Hence we refer to it as a non-Gaussian state, or do we?

2.2.2 Non-Gaussian states

In Fig. 2.2 it is clearly seen that the phase diffused coherent state cannot be described by a simple Gaussian Wigner distribution. This begs the question: is it a non-Gaussian state? In order to describe the state we need a non-trivial mixture of Gaussian states; the weight function, G, contains a singularity of δ-function type. But from [69] we have that any such state will have a classical analog, although being non-Gaussian. In fact, all states that can be described by Eq. (2.42) with $P(\alpha)$-distributions with at most δ-function singularities will have classical analogues. The squeezed state does not meet this criterion, hence it has no classical analogue, even though the Wigner distribution is strictly positive [70]. This seems to lead to a possible conclusion, that any state, which can be described by Eq. (2.39) with at most δ-function singularities in $G(\alpha, \zeta)$ is part of the family of Gaussian states. So what can we then refer to as true non-Gaussian states? According to Hudson [71] the Wigner distribution for any pure non-Gaussian state will attain negative values in some region of phase space. This suggest that a possible way to classify a state as being non-Gaussian is the appearance of negative values in the Wigner distribution. Recently a more rigorous and operational limit has been proposed to identify when a state cannot be described as a mixture of Gaussian states [67]. It is based on finding operational limits on the coefficients of the density matrix for Gaussian states and is capable of identifying states which cannot be described by Eq. (2.39).

The Fock states

Remembering the Wigner distributions for the Fock states, Eq. (2.30),

$$W_n(x,p) \quad = \quad \frac{(-1)^n}{\pi} L_n(2x^2+2p^2)e^{-x^2-p^2}, \tag{2.43}$$

it is seen that for $n > 0$ these states are clearly not described by a simple Gaussian shaped bell. They can further obtain negative values, with $W_n(0,0) = (-1)^n/\pi$. Clearly something that distinguishes them from the states given by Eq. (2.39). The Wigner distributions for the first 4 Fock states, $n = 0,..,3$ can be seen in Fig. 2.3. The lowest, $n = 0$, is a Gaussian shaped bell as expected, while the excited Fock states show stronger and stronger oscillations expanding out from the origin.

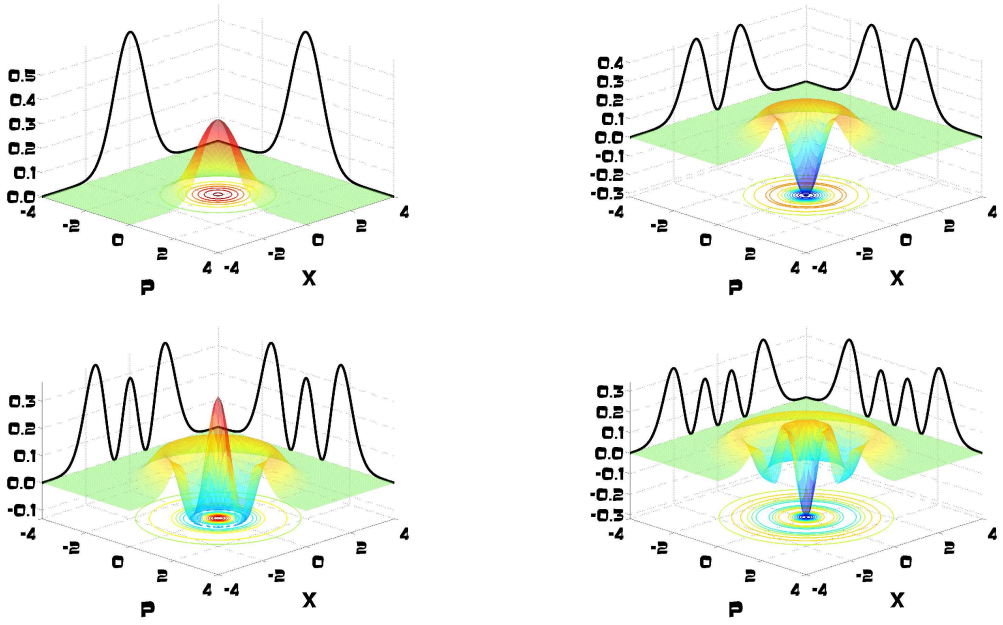

Fig. 2.3: Wigner distibutions for the first 4 Fock states, $n = 0, 1, 2, 3$. The oscillations are seen to become more pronounced as the excitation number increases. Also it is seen that more and more gaps appear in the marginal distributions.

All states are eigenstates of the harmonic oscillator Hamiltonian and thus also of the photon number operator, $\hat{n}$, meaning they have a perfectly defined number of photons, while the phase is completely undetermined. This can be used to state a somewhat ambiguous uncertainty relation between the photon number and the phase, $\mathrm{Var}(\hat{n})\mathrm{Var}(\hat{\varphi}) \geq C$, where C is some constant. This relation is not strictly valid since no phase-operator, $\hat{\varphi}$, can be formulated for the quantum mechanical harmonic oscillator. States of this type have been experimentally demonstrated up to $n = 2$ in a number of experiments in recent years [49, 72, 73].

Coherent state superpositions

Ever since E. Schrödinger first proposed quantum states of this type [74], the so-called cat states have been the subject of much debate and intense research. The present interpretation not being that of the physiological state of a cat trapped inside a box, "dead" or "alive", but the superposition of states which are distinguishable using only classical means. For the optical field the most classical-like states we have are the coherent states. Therefore it makes sense to consider a superposition of two coherent states [75] as the practical realization of Schrödingers *Gedankenexperiment*.

For this reason superpositions of coherent states are often named cat-states,

$$|\text{😺}(\alpha,\varphi)\rangle \quad = \quad \frac{1}{\sqrt{N(\alpha,\varphi)}}(|\alpha\rangle + e^{i\varphi}\,|-\alpha\rangle) \tag{2.44}$$

where $N = 2(1+\cos(\varphi)e^{-2|\alpha|^2})$ is the normalization factor. Without loss of generality we can assume α is real, since this is merely a rotation of phase space, which does not alter the state. Calculating the Wigner distribution for this state we find

$$W_{\text{😺}} \quad = \quad \frac{1}{N(\alpha,\varphi)}\Big[W_0(x-x_0,p)+W_0(x+x_0,p)+2\cos(4x_0p+\varphi)W_0(x,p)\Big], \tag{2.45}$$

where $W_0(x,p)$ is the vacuum Wigner distribution. The two first parts describe the Gaussian-shaped functions of the individual coherent states placed at $\pm x_0$. The last term is an interference term, which oscillates faster with increasing distance between the coherent states. The open possibility to create superpositions between any two macroscopically distinct states and naming the result a Schrödinger cat-state in honor of the original proposal can lead to confusion. So in order to remain clear, the state given in Eq. (2.44) will for the remainder of this work be referred to by the more precise "Coherent state superposition" (CSS). A few examples of coherent state superpositions are shown in Fig. 2.4. Looking at the Wigner distributions it is seen that the two constituting Gaussian lumps, $|\pm\alpha\rangle$, are clearly visible, with the interference in between. This interference is seen to go from high at the origin, $\varphi = 0$, over zero, $\varphi = \pi/2$, to low $\varphi = \pi$. Finally a smaller coherent state superposition with $\alpha = 0.75$ is shown. This state is seen to be similar to a single photon Fock state, only with a slight squeeze along one direction.
Looking at the Fock state decomposition of Eq. (2.44) can provide more insight into the features of the coherent state superposition

$$|\text{😺}(\alpha,\varphi)\rangle \quad = \quad \frac{1}{\sqrt{N(\alpha,\varphi)}}\sum_{n=0}^{\infty}\frac{\alpha^n+e^{i\varphi}(-1)^n\alpha^n}{\sqrt{n!}}\,|n\rangle \tag{2.46}$$

From this we can see that if $\varphi = 0$ ($\varphi = \pi$), only even (odd) terms are left in the superposition. For this reason these states are called the even (odd) coherent state superpositions. Taking $P(\alpha') = 1/2\delta(\alpha'-\alpha)+1/2\delta(\alpha'+\alpha)$ in Eq. (2.42) we find the statistical mixture of the same two coherent states, $1/2\,|\alpha\rangle\langle\alpha| + 1/2\,|-\alpha\rangle\langle-\alpha|$.

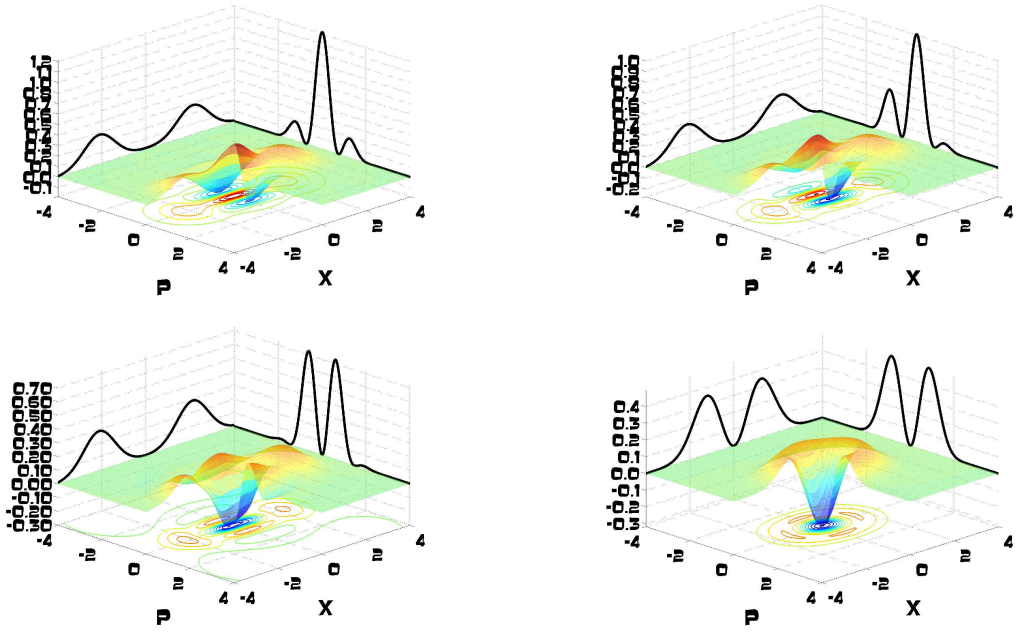

Fig. 2.4: Wigner distributions for coherent state superpositions for $\alpha = 1.5$, going from the even, $\varphi = 0$, over the "circular", $\varphi = \pi/2$, to the odd, $\varphi = \pi$, superposition. Finally, the odd superposition is also shown for $\alpha = 0.75$.

This state would have the Wigner distribution

$$W_{\pm\alpha}(x,p) = \frac{1}{2}(W_0(x-x_0,p) + W_0(x+x_0,p). \tag{2.47}$$

From this we see that a main difference between superpositions and mixtures of Gaussian states is the ability of the former to attain interference and negative values in the Wigner distribution. Looking at the marginal distributions, we can get an idea of how similar and yet how different the coherent state superposition and coherent state mixture really are. The marginals for $\hat{x}$ and $\hat{p}$ are shown in Fig. 2.5, for $\alpha = 2$ for both $\varphi = 0$ and π. Looking at the marginals for the $\hat{x}$-quadrature it is seen that the states are virtually identical. The reason for this is, that along this phase space direction, the main contributors to the marginal distribution are the two coherent states. The main difference is the $\hat{x}(0) = 0$ value for the odd coherent state superposition, while the coherent state mixture and the even superposition have finite values at $\hat{x}(0)$. Looking at the $\hat{p}$-quadrature on the other hand, a clear difference can be seen. The coherent state mixture looks exactly like the vacuum state, while both the even and odd superpositions show strong oscillations.

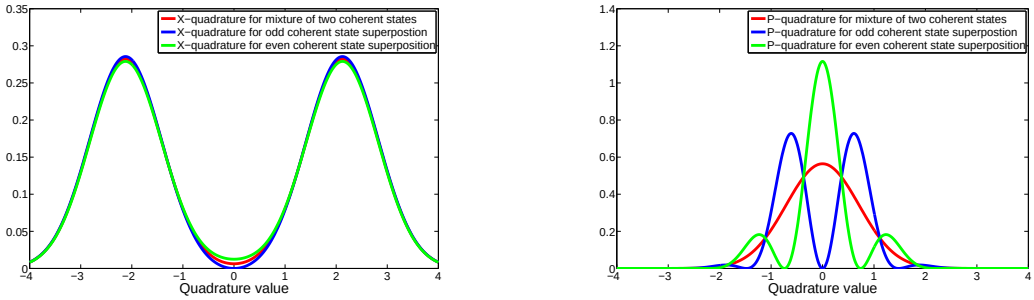

Fig. 2.5: Marginal distributions for the $\hat{x}$- and $\hat{p}$-quadratures for a mixture of two coherent states (red), an even coherent state superposition (green) and an odd coherent state superposition (blue).

2.3 Nonlinear optics

Having seen how a series of exotic states can be prepared in the optical field, the question now is how to prepare these states. Using only linear transformations such as the displacement operator, only states given by Eq. (2.42) can be prepared. Allowing for non-linear transformations will greatly extend the potential for preparing optical states. Non-linear interaction in the optical field is a highly matured research field. This is spurred by the discovery of various highly efficient non-linear dielectric materials and the constant progress within material engineering.

Even though non-linear interactions to arbitrary order can in principle occur in a dielectric medium we can often limit ourselves to certain orders. We are mostly interested in the second or third order non-linearities since these enables us to prepare the states presented in the previous section. The squeezed states (one- and two-mode) can be prepared using the second order non-linearity while the third order non-linearity allows for the preparation of coherent state superpositions [76].

In this work non-linear interactions between optical fields is a key tool, and we will provide a discussion of some of the aspects to keep in mind when implementing these interactions. The starting point when treating electromagnetic waves is Maxwell's equations. From [77] we have

$$\begin{aligned} \nabla \times \mathbf{E}(t) &= -\frac{\partial}{\partial t}\mathbf{B}(t), \\ \nabla \times \mathbf{H}(t) &= \epsilon_0 \frac{\partial}{\partial t}\mathbf{E}(t) + \mathbf{J}_c(t) + \frac{\partial}{\partial t}\mathbf{P}(t), \end{aligned} \tag{2.48}$$

where $\mathbf{J}_c(t)$ is the conduction current density and $\mathbf{P}(t)$ is the polarization induced in the media by the electromagnetic field given by $\mathbf{E}(t)$, $\mathbf{B}(t)$. In optics, including

quantum optics, we are usually only dealing with dielectric, non-magnetic media, with no free charges. Under these constraints a vector equation governing the traveling electrical field in the media can be derived

$$\begin{aligned} \nabla \times \nabla \times \mathbf{E}(t) &= -\frac{1}{c^2}\frac{\partial^2}{\partial t^2}\mathbf{E}(t) - \mu_0 \frac{\partial^2}{\partial t^2}\mathbf{P}(t), \\ \nabla \times \nabla \times \mathbf{E}(\omega) &= \frac{\omega^2}{c^2}\mathbf{E}(\omega) + \omega^2 \mu_0 \mathbf{P}(\omega), \end{aligned} \tag{2.49}$$

where the first equation is expressed in terms of the temporal components and the second in terms of the frequency components, related through the Fourier transform. Expressing the polarization in terms of its linear and non-linear parts, $\mathbf{P}(\omega) = \epsilon_0 \chi^{(1)} \mathbf{E}(\omega) + \mathbf{P}^{NL}(\omega)$, Eq. (2.49) can be re expressed as [78]

$$\nabla \times \nabla \times \mathbf{E}(\omega) = \frac{\omega^2}{c^2}\epsilon(\omega) \cdot \mathbf{E}(\omega) + \omega^2 \mu_0 \mathbf{P}^{NL}(\omega), \tag{2.50}$$

where $\epsilon(\omega) = 1 + \chi^{(1)}(-\omega; \omega)$ is the linear dielectric tensor and $\mathbf{P}^{NL}(\omega) = \sum_{n=2}^{\infty} \mathbf{P}^{(n)}(\omega)$ is the nonlinear polarization of the media. Equivalently for the temporal evolution of the field and polarization,

$$\nabla \times \nabla \times \mathbf{E}(t) = \mu_0 \int_{-\infty}^{\infty} d\omega' (\omega + \omega')^2 \epsilon(\omega) \cdot \mathbf{E}(\omega) e^{-i(\omega+\omega')t} - \mu_0 \frac{\partial^2}{\partial t^2}\mathbf{P}^{NL}(t). \tag{2.51}$$

2.3.1 Parametric interaction

The non-linear polarization in Eq. (2.50) will often be dominated by a single term, typically the second or third order non-linear induced polarization. In this work we are only concerned with the second order non-linearity,

$$\mathbf{P}^{(2)}(\omega) = \epsilon_0 \chi^{(2)}(-\omega; \omega_1, \omega_2) : \mathbf{E}_1(\omega_1) \otimes \mathbf{E}_2(\omega_2), \tag{2.52}$$

where $\chi^{(2)}(-\omega; \omega_1, \omega_2)$ is the second order non-linear dielectric tensor, relating the frequency ω with the frequencies $\omega_{1,2}$. Also, we are mainly concerned with traveling wave solutions to the equations, which cannot be assumed to be monochromatic,

$$\mathbf{E}(\omega) = \hat{\mathbf{E}}(\omega) e^{i\mathbf{k}\cdot\mathbf{r}} \tag{2.53}$$

Here $\mathbf{k}(\omega) = (\omega[n(\omega) + i\kappa(\omega)]/c)\mathbf{s}$ is the wave vector in direction $\mathbf{s}$, with $n(\omega)$ and $\kappa(\omega)$ being the real and imaginary refractive indices related through the Kramers-

Kronig relations [79, 80]. In general the envelope function $\hat{\mathbf{E}}(\omega)$ incorporates both amplitude and phase information about the wave and is a function of all three spatial coordinates. Inserting Eqs. (2.53) and (2.52) into Eq. (2.50), differential equations can be derived for the different frequency components.

$$\begin{aligned}\nabla \times \nabla \times [\hat{\mathbf{E}}(\omega)e^{i\mathbf{k}\cdot\mathbf{r}}] \;=\; & \frac{\omega^2}{c^2}\epsilon(\omega)\hat{\mathbf{E}}(\omega)e^{i\mathbf{k}\cdot\mathbf{r}} \\ & + \omega^2\mu_0\epsilon_0\chi^{(2)}(-\omega;\omega_1,\omega_2) : \hat{\mathbf{E}}_1(\omega_1)\hat{\mathbf{E}}_2(\omega_2)e^{i(\mathbf{k}_1+\mathbf{k}_2)\cdot\mathbf{r}}\end{aligned} \tag{2.54}$$

In the general case, Eq. (2.54) is difficult to solve. However, some important conclusions may be drawn from the result. In order for the interacting fields to couple efficiently, the following conditions must often be met,

$$\omega \;=\; \begin{cases} \omega_1+\omega_2 \\ 2\omega_{1,2} \\ \omega_1-\omega_2 \\ 0 \end{cases} \quad \vee \quad \mathbf{0} \;=\; \begin{cases} \mathbf{k}-\mathbf{k}_1-\mathbf{k}_2 \\ \mathbf{k}-2\mathbf{k}_{1,2} \\ \mathbf{k}-\mathbf{k}_1+\mathbf{k}_2 \\ \mathbf{k}+\mathbf{k}_1+\mathbf{k}_2 \end{cases}. \tag{2.55}$$

The first condition can be interpreted as energy conservation while the second can be interpreted as momentum conservation. The first two cases will result in a field with a higher frequency, $\omega > \omega_{1,2}$ and are referred to as Sum-frequency generation and Second-harmonic generation (SFG and SHG). The third case is generally referred to difference frequency generation (DFG) and will result in a field with lower frequency. The last condition will induce a constant polarization in the dielectric material. In this work the SHG and DFG effects are exploited in preparing non-classical states of the light-field.

Second-harmonic generation

SHG is the effect where two identical fields (in practice just one field) at a low frequency ω interact to prepare the second-harmonic 2ω. In this case, the momentum conservation yields $\mathbf{k}_{2\omega} - 2\mathbf{k}_\omega = \mathbf{0}$. Fulfilling this momentum condition is generally referred to as phase-matching and is an important task in parametric interaction. Achievement of phase-matching is dependent on both the spatial shape of the interacting fields as well as their spectral distribution. As we remember, $\mathbf{k}$ depends on ω in a non-trivial way through $n(\omega)$ and $\kappa(\omega)$. In most dielectric materials of interest we can assume that absorption is negligible so $\kappa(\omega) = 0$. In that case, we only have to concern ourselves with the refractive index $n(\omega)$. This dependence can in general

not be predicted, but is inferred from experiments. This is done by measuring the refractive index at a series of known wavelengths. Then these measurements are fitted to an assumed wavelength dependence, which enables the prediction of the refractive index, for the particular material. Such expressions ate typically referred to as Sellmeier equations. If we only consider the paraxial part of the phase-matching Eq. (2.55) simplifies to

$$\Delta k \;=\; 2\omega[n(2\omega) - n(\omega)] \;=\; 0. \tag{2.56}$$

Given that this condition is fulfilled, Boyd and Kleinmann were able to find the optimal solution for focusing of Gaussian beams in parametric interaction [81]. In general, Eq. (2.56) cannot be fulfilled due to the dispersion $n(2\omega) \neq n(\omega)$, so other means have to be employed in order to achieve phase-matching.

Difference-frequency generation

Difference frequency generation is the effect where two fields at different frequencies $\omega_{1,2}$ interact to generate a third field at the difference frequency $\omega = \omega_1 - \omega_2$. This process is subject to the same constraints as SHG meaning the paraxial phase-matching condition can be expressed as

$$\Delta k \;=\; (\omega_1 - \omega_2)n(\omega_1 - \omega_2) - \omega_1 n(\omega_1) - \omega_2 n(\omega_2) \;=\; 0. \tag{2.57}$$

Again dispersion prevents this from being fulfilled in general. We can also see how this process has more freedom than the SHG. In SHG all frequencies are determined by the low-frequency field, ω. In DFG there are three fields meaning there are two degrees of freedom. In principle, this enables one to reach any frequency by choosing $\omega_{1,2}$ in an appropriate manner. The special case $\omega = \omega_2 = 1/2\omega_1$ will be interesting later. In this case

$$\Delta k \;=\; \omega n(\omega) - 2\omega n(2\omega) + \omega n(\omega) \;=\; 0, \tag{2.58}$$

which is exactly the same condition as in Eq. (2.56) for SHG. Thus, the processes of combining one field with itself to generate the second-harmonic and the process of a field mixing with its second-harmonic to generate itself are complementary. The conditions for both will be fulfilled at the same time. The relative phase between the fields determines which of the processes dominates.

Spontaneous parametric interaction

Both the SHG and the DFG processes are referred to as three-wave-mixing processes. The SHG is a special case where two of the waves are identical and thus considered as one wave. But both processes require at least two of the fields to have initial non-zero amplitudes. If this is not the case, the classical description has only the trivial non-interacting solution. Changing to the quantum picture the situation is different. In this picture it is often more advantageous to work in the temporal domain. Exchanging the field amplitudes with the quantum mechanical field operators,

$$\begin{aligned} \hat{\mathbf{E}}^{(-)}(\omega) &= i\left(\frac{\omega c}{2n(\omega)}\right)^{1/2}\hat{\mathbf{a}}(\omega), \\ \mathbf{E}^{(-)}(\mathbf{r},t) &= \frac{1}{\sqrt{2\pi}}\int_{-\infty}^{\infty} d\omega \hat{\mathbf{E}}^{(-)}(\omega)e^{-i\omega t+i\mathbf{k}\cdot\mathbf{r}}, \end{aligned} \tag{2.59}$$

and inserting into the nonlinear polarization, one finds [57]

$$\mathbf{P}^{(2)}(\mathbf{r},t) = \frac{\epsilon_0}{2\pi}\int_{-\infty}^{\infty}\int_{-\infty}^{\infty} d\omega_s d\omega_p \chi^{(2)}(\omega_i;-\omega_s,\omega_p):\hat{\mathbf{E}}^{(+)}(\omega_s)\hat{\mathbf{E}}^{(-)}(\omega_p)e^{i(\omega_s-\omega_p)t-i(\mathbf{k}_s-\mathbf{k}_p)\cdot\mathbf{r}}. \tag{2.60}$$

Here, the s-component is generally referred to as the signal, the i-component as the idler and the p-component as the pump. Assuming the field at the pump-frequency ω_p is a sufficiently strong coherent state, we can make the substitution,

$$\hat{\mathbf{a}}(\omega_p) = \alpha(\mathbf{r},\omega_p-\omega_0)e^{i\theta_p[\mathbf{r},\omega_p-\omega_0]} \tag{2.61}$$

Here, $\alpha(\mathbf{r},\omega_p-\omega_0)$ is the spatial envelope of the frequency dependent coherent state amplitude, with a center frequency, ω_0, and $\theta_p(\omega_p-\omega_0)$ being the phase of the individual frequency components. Inserting this into Eq. (2.60) and taking the Fourier transform, we find the non-linear polarization at the frequency ω_i

$$\begin{aligned} \mathbf{P}^{(2)}(\omega_i) = \frac{i\epsilon_0}{2\pi}\int_{-\infty}^{\infty} d\omega_s \left(\frac{(\omega_s+\omega_i)c}{4\pi n(\omega_s+\omega_i)}\right)^{1/2}\hat{\alpha}(\omega_s+\omega_i-\omega_0)e^{i\theta_p(\omega_s+\omega_i-\omega_0)} \\ \times\chi^{(2)}(\omega_i;-\omega_s,\omega_s+\omega_i)\hat{\mathbf{E}}^{\dagger}(\omega_s)e^{-\frac{i}{c}[n(\omega_s)\omega_s\mathbf{e}_s-n(\omega_s+\omega_i)(\omega_s+\omega_i)\mathbf{e}_p]\cdot\mathbf{r}}, \end{aligned} \tag{2.62}$$

where $\mathbf{e}_{s,p}$ are unit vectors indicating the direction of propagation for the pump and signal fields. Inserting this into Eq. (2.50) along with (2.53) we find,

$$\begin{aligned}\nabla \times \nabla \times \left[\hat{\mathbf{E}}(\omega_i)e^{i\mathbf{k}_i\cdot\mathbf{r}}\right] &= \frac{\omega_i^2}{c^2}\epsilon(\omega_i)\hat{\mathbf{E}}(\omega_i)e^{i\mathbf{k}_i\cdot\mathbf{r}} \\ &+ i\frac{\omega_i^2}{c^2}\int_{-\infty}^{\infty}\left(\frac{(\omega_s+\omega_i)c}{4\pi n(\omega_s+\omega_i)}\right)^{1/2}\hat{\alpha}(\omega_s+\omega_i-\omega_0)e^{i\theta_p(\omega_s+\omega_i-\omega_0)} \\ &\times\chi^{(2)}(\omega_i;-\omega_s,\omega_s+\omega_i)\hat{\mathbf{E}}^\dagger(\omega_s)e^{-\frac{i}{c}[n(\omega_s)\omega_s\mathbf{e}_s-n(\omega_s+\omega_i)(\omega_s+\omega_i)\mathbf{e}_p]\cdot\mathbf{r}}d\omega_s\end{aligned} \tag{2.63}$$

This equation and a similar one which can be derived for $\hat{\mathbf{E}}^\dagger(\omega_s)$ can, in general, only be solved numerically, except in certain limits. One of those limits is for the plane waves, and assuming that the slowly-varying-wave approximation holds. The latter can be assumed to be true for almost any interaction involving fields at optical frequencies. Under these approximations the frequency correlations between the signal and idler fields can be shown to be roughly proportional to

$$\Psi(\omega_s,\omega_i) \quad \propto \quad \alpha(\omega_s+\omega_i-\omega_0)\mathrm{sinc}\left(\frac{\Delta kL_c}{2}\right), \tag{2.64}$$

where

$$\Delta k = n[\omega_s]\omega_s + n[\omega_i]\omega_i - n[\omega_s+\omega_i](\omega_s+\omega_i) \tag{2.65}$$

is the phase-mismatch. Eq. (2.64) we see that the frequency correlations in the downconverted are determined both by the pump field and the phase matching envelope. So in order to decorrelate the two attention must be paid to both the pump field and the phase matching conditions in the crystal. From Eqs. (2.64) and (2.65) it is seen how $\Delta k = 0$ must be fulfilled in order for the SPDC process to be efficient. In the special case $\omega_s = \omega_i$ it turns out that the solution to Eq. (2.63) in the case of a monochromatic pump field α is exactly the transformation achieved through the squeezing operator, Sec. 2.2. Thus the non-linear parametric interaction with vanishing initial signal/idler fields in the degenerate case enables the generation of a squeezed vacuum state.

Phase matching

We have seen how important it is to fulfill the condition $\Delta k = 0$ in order to have efficient parametric interaction. But due to dispersion this condition can, in general,

not be met without tricks. The most common trick utilized in parametric interaction today is that of Quasi-phase-matching (QPM). It is a technique where the condition is not really met, but by careful engineering of the dielectric media, the interacting waves are in a sense "fooled" to believe it is. In the previous derivations we have seen how it is the quantity, $\Delta kz = 0$, that is really important. If we keep the interaction lengths, z, short, the effect of this phase-mismatch can be reduced. Also, it turns out that by alternating the sign of the non-linear susceptibility $\chi^{(2)}$, it is possible to choose in which direction the energy in the interaction will flow. If this modulation is done with a periodicity Λ it will correspond to adding a term $\mathbf{K}_C = 2\pi\mathbf{k}/\Lambda$ in Eq. (2.56). For the difference frequency generation the phase-matching condition will be

$$\mathbf{k}_p - \mathbf{k}_s - \mathbf{k}_i \pm \mathbf{K}_C = \mathbf{0} \tag{2.66}$$

This is, in general, a 3D vector equation and much research has been devoted to engineering sophisticated $\mathbf{K}_C$ in order to prepare the signal/idler fields in specific frequency/spatial modes, see for instance [82, 83, 84, 85, 86, 87]. Here we are only interested in the paraxial solution to the phase-matching problem. Since the modulation period of the dielectric is constant, Eq. (2.66) can only be fulfilled for a specific set of frequencies, $\omega_p, \omega_s, \omega_i$. The particular case one is interested in is determined by the application at hand. The optimal modulation period can be found to be

$$n(\omega_s + \omega_i)\left(\frac{1}{\lambda_s} + \frac{1}{\lambda_i}\right) - \frac{n(\omega_s)}{\lambda_s} - \frac{n(\omega_i)}{\lambda_i} \pm \frac{1}{\Lambda} = 0. \tag{2.67}$$

2.4 Probing the quantum nature of light

As we saw in Sec. 2.1 the quantum state of light can attain many forms and be described by numerous representations. With this multitude of descriptions, naturally a wide array of measurement strategies are required to probe the particular property of interest in a given system. In this section we will present a brief review of the most commonly occurring detection strategies, which will also be employed in this work.

2.4.1 Intensity measurement

When dealing with light, the most used quantity is power (or intensity), i.e. the optical energy passing through a given area in a given time. This is typically measured

by collecting the energy over a known time-interval, Δt, and area A, and generating an electronic signal that is related to the optical energy. Then by inverting the relation

$$i \quad = \quad g \int_A \int_0^{\Delta t} I(t, \vec{\mathbf{r}}) dt d\vec{\mathbf{r}}, \tag{2.68}$$

it is possible to find either the power or directly the intensity distribution. This type of measurement is done using photodiodes, which generally have a very linear relation between the amount of collected light and the size of the generated electronic signal; the size of the output current. The proportionality constant g is typically stated in one of two ways; either as the responsivity, which is the the amount of current per optical power, A/W, or as a quantum efficiency, which is the probability that a given input photon is converted into an electron leaving the photodiode, η_Q. Typical photodiodes have quantum efficiencies of the order $90\% - 95\%$ in the NIR wavelengths, with demonstrations of as much as 99%. With such high quantum efficiencies the photodiodes can provide electronic signals which are highly accurate representations of the incoming optical fields.

However, this type of detectors does not allow for the detection of very weak optical fields. The electronic circuitry required for photodiodes will inevitably add noise to the detected signal. This noise will drown weak signals, thus making them undetectable. State-of-the-art photodiodes can these days be designed with noise-equivalent-powers of a few hundred femto-Watts, corresponding to a few million photons per second. In Sec. 2.1 we saw that typical quantum states only contain a few photons, meaning this type of detectors is not applicable when detecting quantum states.

In order to probe the nature of quantum states at the few photon level, we need detectors which are capable of detecting individual photons at this level. Much research is going into this type of detectors, and progress has been made towards detectors capable of detecting and distinguishing between multiple photons at the level of 4-5 photons [88, 89]. Quantum mechanically, we often describe this type of measurement by the following set of operators

$$\hat{\Pi}_n \quad = \quad |n\rangle \langle n| , \qquad \sum_{n=0} \hat{\Pi}_n \; = \; \hat{\mathbb{1}}. \tag{2.69}$$

This type of photon-number-resolving (PNR) detectors is still rare and thus expensive, and often requires sophisticated control circuitry to operate. A more developed subclass of these detectors are the avalanche photo diodes (APDs). This is a simple

form of the PNR detectors. It is capable of distinguishing between the presence of an unspecified low number of photons and no photons. It can be represented by the pair of operators,

$$\hat{\Pi}_1 \;=\; \hat{\mathbb{1}} - |0\rangle\langle 0|\,, \quad \vee \quad \hat{\Pi}_0 \;=\; |0\rangle\langle 0| \tag{2.70}$$

This type of detectors makes it possible to determine if a single photon was present or not. They do so by providing a strong electronic signal when a single photon is detected. This is achieved by applying a reverse bias voltage greater than the breakdown voltage across the diode. This means that when an electron is "kicked" loose by an impinging photon, a strong electronic signal is created, which can be picked up, amplified and shaped so it can be easily detected, thus making individual photons detectable. Typically, this can be done with reasonably high timing precision, potentially down to tens of pico-seconds. This type of detectors unfortunately often suffers from low quantum efficiency, with values normally not exceeding 60%.
In quantum mechanics the detection and characterization of fluctuations is often a priority. In Sec. 2.2 we saw how different quantum states exhibit different behavior. For instance, the coherent state, $|\alpha\rangle$, was seen to show Poissonian statistics in the number of photons. For this type of statistics the variance of the photon number scales linearly with power, $\mathrm{Var}(n) = n$. Noise with this scaling is called shot noise, and as such optical signals with this noise scaling are called shot noise or quantum noise limited. However, optical signals can show a different excess noise scaling. A typical scaling of thermal noise is $\mathrm{Var}(n) = n^2$.

2.4.2 Homodyne detection

The detectors described in the previous section can only provide information about the photon number distribution of a quantum state. This limits the knowledge we can achieve about the density matrix presented in Sec. 2.1.1 to the diagonal elements. In order to obtain the full information about the probed quantum state, we need to be able to extract information about the phase or the off-diagonal matrix elements. This information is not accessible using the intensity detectors, due to the pseudo-uncertainty relationship between photon number and phase, Sec. 2.2.2. In order to access the phase information we need some other means of detection. Here we are saved by the concept of homodyne detection. Homodyne detection has been a well-established technique in detecting weak electromagnetic fields for years. It basically entails mixing the weak fast oscillating electromagnetic field (signal) with a strong, coherent, electromagnetic field of known frequency, usually called a local

oscillator (LO). The two fields will then show a beating behavior, which depends on the characteristics of the signal and the relative frequency and phase of the two fields. In quantum optics we also have the option of employing this strong tool. Here it is called balanced homodyne detection and works by interfering the optical field to be probed with a strong coherent field as illustrated in Fig. 2.6. By this technique

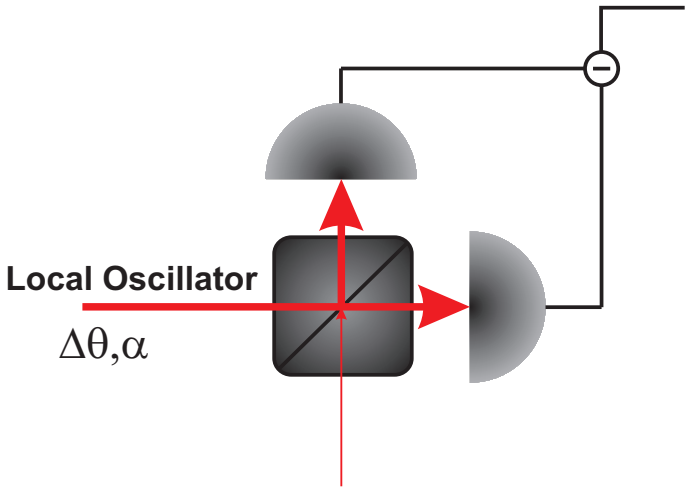

Fig. 2.6: In homodyne detection a strong local oscillator, LO, is interfered with the weak quantum state on a beam splitter. The outputs are detected by two photodiodes and the difference current will be proportional to the measured quadrature value.

we can gain access to information about the quadrature variables at an arbitrary phase, even for fields of vanishing intensity. Balanced homodyne detection is a well-established technique constantly being employed in quantum optics labs around the world, and it has been extensively covered in the literature [90]. Here, we will only briefly review the basic theory of how homodyne detection is made possible. By mixing a strong coherent signal with a weak quantum state on a beam splitter we find

$$\begin{aligned} \hat{a}_1 &= r\alpha e^{i\theta} + t\hat{a}_s \\ \hat{a}_2 &= t\alpha e^{i\theta} - r\hat{a}_s \end{aligned} \tag{2.71}$$

where r/t are the reflectance/transmittance of the mixing beam splitter which fulfills the condition $r^2 + t^2 = 1$. In Eq. (2.71) we have made the substitution $\hat{a}_{LO} \rightarrow \alpha e^{i\theta}$, since the local oscillator can be assumed to be a strong classical field. The photocurrent generated in a photodiode will be proportional to the number of photons

$$i = G\hat{n} = G\hat{a}^\dagger\hat{a}, \tag{2.72}$$

where G is some gain factor. Using this to find the difference current, we get

$$i_- \;=\; i_1 - i_2 \;=\; \alpha^2(G_1 r^2 - G_2 t^2) + \hat{n}_s(G_1 t^2 - G_2 r^2) + \alpha r t(G_1 + G_2)(\hat{a}_s^\dagger e^{i\theta} + \hat{a}_s e^{-i\theta}).$$

By requiring balancing of the classical signal, $G_1 r^2 - G_2 t^2 \;=\; 0$, and using the fact that the amplitude of the LO is much greater than the number of photons in the signal, the difference current can be expressed as

$$i_- \;=\; \sqrt{2}\alpha\sqrt{G_1 G_2}\hat{q}_\theta \tag{2.73}$$

where $\hat{q}_\theta$ is the quadrature operator for the signal at LO phase θ. We can also see why this technique is called balanced homodyne detection. The balancing is required to remove the effect of the classical amplitude and any classical noise effects on the difference current. This is not necessarily achieved by a 50/50 beam splitter, but rather by ensuring the equal distribution of LO power after the photodiodes. Finally, it is also seen that the LO amplitude must be sufficiently high, in order for the difference current to provide an accurate description of the measured quadrature. From Eq. (2.73) we can also see how the noise of the measured quadrature is amplified to a measurable level by interference with the LO

$$\mathrm{Var}(i_-) \quad = \quad 2\alpha^2 G_1 G_2 \mathrm{Var}(\hat{q}_\theta). \tag{2.74}$$

From this we have that even small fluctuations can be arbitrarily amplified and are thus measurable. By assembling a histogram of the difference currents we can also build a histogram of the measured quadrature variable. We know from Eq. (2.24) that by building a histogram we gain, at least, partial information about the wavefunction for the probed quantum state since the histogram is just an arbitrarily rescaled version of the probability density,

$$\mathrm{pr}(\hat{q}_\theta) \quad \propto \quad |\psi_\theta(ax)|^2, \tag{2.75}$$

where a is arbitrary rescaling constant found by calibrating to a known reference state. Now quantum states are fragile and will degrade through interaction with the environment. This type of degradation can be modeled by a beam splitter operation on the quadrature operator in Eq. (2.73) with vacuum on the other port

$$i_- \;=\; \sqrt{2}\alpha\sqrt{G_1 G_2}(\sqrt{\eta}\hat{q}_\theta + \sqrt{1-\eta}\hat{q}_v), \tag{2.76}$$

where η is the detection efficiency and $\hat{q}_v$ denotes the vacuum mode admixed with the signal at the beam splitter. In Eq. (2.71) we have assumed that the LO and the signal interferes perfectly at the balancing beam splitter. This is, however, not usually the case. Normally, only a certain interference contrast can be obtained between the LO and the signal. We quantify this contrast by the visibility, $0 \leq V \leq 1$. This interference contrast will enter the detection efficiency as beam splitter loss with $\eta = V^2$ [91] and for this reason much attention must be paid to this interference contrast or mode-matching.
Comparing with Eqs. (2.70) and (2.69), the homodyne detector can also be described by a set of operators

$$\hat{\Pi}_\theta = |X_\theta\rangle \langle X_\theta|, \tag{2.77}$$

which can be seen as a projection onto an infinitely squeezed state along the phase-space direction θ [30]. This measurement is highly idealized and corresponds to projection onto an infinite energy state. In practice this measurement is not possible. A more realistic description of the measurement would be

$$\hat{\Pi}_\theta = \int_{x_0-\Delta x}^{x_0+\Delta x} |X_\theta\rangle \langle X_\theta| \, dX_\theta, \tag{2.78}$$

where x_0 is the central position of the projection interval and Δx is the "uncertainty" or acceptable range around it. Both of these measurement operations rely on the projection onto Gaussian states, thus they are themselves Gaussian operations.

2.4.3 Manipulating quantum states through measurements

From [54] we have that measurements on a number of subsystems, $\mathbb{H}^{\otimes n}$, of a quantum state existing in at least $\mathbb{H}^{\otimes m}$, $n < m$, will result in an output state given by

$$\hat{\rho}_{out,n+1..m} = \frac{\mathrm{Tr}_{1..n}[\hat{\Pi}_{1..n}\hat{\rho}_{in}]}{\mathrm{Tr}[\hat{\Pi}_{1..n}\hat{\rho}_{in}]}. \tag{2.79}$$

Here, $\hat{\Pi}_{1..n}$ is a multimode POVM across the subsystems, $1..n$, and $\mathrm{Tr}_{1..n}$ is the partial trace over the same subsystems. What happens is that the $1..n$ subsystems are collapsed into some intended target states given by $\hat{\Pi}_{1..n}$ and subsequently thrown away. If $\hat{\rho}_{in}$ contains known correlations, then by appropriate choice of $\hat{\Pi}_{1..n}$, it is possible to project the output state, ρ_{out}, into a desired target state. This strategy is regularly being employed when preparing exotic quantum states.

In this work the goal is to employ a scheme where the input state, $\hat{\rho}_{in}$, is a squeezed state, which is split on beam splitter. One output port is then measured using an appropriate detection system, in our case a photon resolving system, to determine when a particular event occurred. The output should be a state, reminiscent of the coherent state superposition described in Sec. 2.2. This output is then measured using a homodyne detection scheme. Further on, the goal is to build a scheme where two CSS' are mixed on a beam splitter, and the output is projected onto a desired target using another appropriate measurement.

2.4.4 Quantum state tomography

Preparing exotic quantum states is of no use if we have no way of verifying the preparation. This is the process of quantum state tomography [90]. From Eq. (2.13) we have that the probability distribution, $f(\sigma)$, for a given measurement operator, $\hat{\Pi}(\sigma)$ is given by,

$$f_\rho(\sigma) \quad \equiv \quad \mathrm{pr}(\sigma)_{\hat{\rho}} \ \equiv \ \mathrm{Tr}[\hat{\Pi}(\sigma)\hat{\rho}] \tag{2.80}$$

Here, $\hat{\rho}$ is the density matrix of the state under investigation. The purpose of state tomography is the inversion of the expression in Eq. (2.80). This inversion is a non-trivial problem with a formal solution,

$$F(\alpha) \quad = \quad \int d\sigma K(\alpha,\sigma) f_\rho(\sigma) \tag{2.81}$$

where $K(\alpha,\varsigma)$ is an integration kernel. In the case of continuous variable optical states, the variable in question is the generalized quadrature variable, $\varsigma = q_\theta$. Now θ is a continuous variable so the measurement projectors in Eq. (2.80) will also be a continuous set of projectors. In order to invert the expression through the integral in Eq. (2.81) a probability distribution is needed for all projectors $\hat{\Pi}_\theta$ [92]. This means that we need to measure a probability distribution at every point of a continuous distribution which is obviously not possible. Even if we imagine for a second that it is possible to measure a probability distribution for all settings of θ, we will still get into trouble. These probability distributions will in any case only be approximations to the actual distribution due to the limited number of samples. If we were to acquire the true probability distribution, we would need to measure an infinite number of times at the given setting. This lack of tomographic precision (limited number of settings) and statistical precision (limited number of measurements) usually leads to unphysical solutions when attempting to evaluate the integral in Eq. (2.81) [93]. This

procedure of back-projection is, however, often used through a "low-pass filtering" of the integration kernel.
Another procedure has been presented by Hradil [93]. The procedure was made operationally available through an algorithm by Banaszek *et al.* [94] and further development has been done by Ježek *et. al.* [95] and by Lvovsky [96]. The idea is to find the probability for a given set of outcomes, $\varsigma_{1..N}$, measured on a finite set of sample states $\hat{\rho}_{1..N}$, given a known set of measurement settings, $\hat{\Pi}_\theta(\varsigma)$. This probability (likelihood functional $\mathcal{L}(\hat{\rho})$) will be given by

$$\mathcal{L}(\hat{\rho}) \quad = \quad \prod_{i=1}^{N} \mathrm{Tr}[\hat{\Pi}_i(\sigma)\hat{\rho}] \tag{2.82}$$

For computational reasons, often the logarithm of $\mathcal{L}$ is used as an estimator, but since the likelihood is a functional, the logarithm of it will also be a functional. In our case the projector used for the state tomography is the homodyne detector described in the previous section. Applying this measurement projector to our ensemble of identically prepared quantum states, $\hat{\rho}$, we will acquire a set of outcomes, the actual measured quadrature, x_i, and the corresponding phase of the LO, θ_i, $i = 1..N$. Inserting this and Eq. (2.77) into (2.82), the likelihood functional can be evaluated using Eq. (2.25) given a guess of $\hat{\rho}$. Through Eq. (2.77) and the Bernoulli coefficients the maximum likelihood method can also take into account the finite detection efficiency of the homodyne detector, η. Maximizing the likelihood functional for a finite set N of measurement outcomes x_i, given a set of homodyne detector settings θ_i, is done by solving the equation

$$\hat{R}(\hat{\rho}_0)\hat{\rho}_0\hat{R}(\hat{\rho}_0) \;=\; \hat{\rho}_0 \tag{2.83}$$

where

$$\hat{R}(\hat{\rho}_0) \;\equiv\; \frac{1}{N}\sum_i \frac{1}{\langle x_i|\,\hat{\rho}\,|x_i\rangle}\hat{\Pi}_{\theta_i} \tag{2.84}$$

From [97, 96, 98] we have that the solution to this extremal problem can be found by iteration using the operator kernel in Eq. (2.84),

$$\hat{\rho}^{n+1} \quad = \quad \hat{R}(\hat{\rho})\hat{\rho}^n\hat{R}(\hat{\rho}). \tag{2.85}$$

The convergence of Eq. (2.85) is not guaranteed [98]. But all reconstructions carried out in this work have converged. The speed of convergence is however found to

depend on initial guess and the degree to which the prepared state is populated. With increasing number of photons in the prepared state the convergence is found to slow down by as much as an order of magnitude, Ch. 5.

Summary

In this chapter we saw how the quantum mechanical harmonic oscillator can be used to describe the state of the optical field. This has the consequence that states of the QM harmonic oscillator can also be realized in the optical field. Of these states the CSS is the most intriguing. The superposition of coherent states is highly non-classical even though the coherent states themselves are semi-classical states.
We saw how non-linear interactions could be used to engineer optical fields at a wide range of frequencies. Also, the potential of SPDC to prepare states with quantum correlations was discussed. Finally, a review of the most important aspects of detection and characterization techniques of quantum optics were reviewed and discussed.

Chapter 3

Quantum state preparation

In the previous section we described how states of the optical field could roughly be grouped into two groups; the Gaussian and the non-Gaussian states. It was also described how second-order non-linearities could be used to prepare squeezed states. Just as for the states it makes sense to divide the quantum optics toolbox into two categories; The Gaussian and the non-Gaussian operations. As described in Ch. 1 Gaussian operations present us with certain limitations if we only have Gaussian states available. These limitations are linked to the fact that Gaussian operations cannot turn a Gaussian state into a non-Gaussian state [30]. Linear operations such as the displacement and second order non-linear operations, such as the squeezing operation are both examples of Gaussian operations. This type of operations has the advantage that they are deterministic and do not rely on any projective measurements.

As the name suggests, non-Gaussian operations do not have this limitation. They can turn a Gaussian state into a non-Gaussian state. However, deterministic non-Gaussian operations require access to non-linearities of at least third order. Non-linearities of third (or higher) order are weak and presently known materials all suffer from non-negligible loss [99]. For this reason deterministic preparation of non-Gaussian states is presently not a feasible strategy. An alternative is to use measurement induced non-linear operations. By projectively measuring parts of a state using some highly non-linear measurement projector it is possible to collapse a Gaussian state into a non-Gaussian state [52]. Implementing such projective measurements is however a non-trivial task, which we will devote some more attention to in the following.

3.1 Gaussian operations

Of Gaussian operations we have so far presented the displacement operator, $\hat{D}(\alpha)$ and the single-mode squeezing operator, $\hat{S}(r)$. These are examples of single-mode Gaussian operations. The Gaussian toolbox also contains some two-mode operators; the two-mode squeezing operator and the beam splitter [57]

$$\hat{S}_2(\zeta_2) \;=\; e^{\zeta_2 \hat{a}_1^\dagger \hat{a}_2^\dagger - \zeta_2^* \hat{a}_1 \hat{a}_2}, \qquad \hat{B}(T) \;=\; e^{\sqrt{T}(\hat{a}_1^\dagger \hat{a}_2 - \hat{a}_2^\dagger \hat{a}_1)}. \tag{3.1}$$

The coherent states can be shown to transform through the beam splitter as follows [57]

$$\hat{B}(T)\,|\alpha\rangle\,|\beta\rangle \;=\; \left|\sqrt{T}\alpha + \sqrt{1-T}\beta\right\rangle \left|-\sqrt{1-T}\alpha + \sqrt{T}\beta\right\rangle, \tag{3.2}$$

which cannot be transformed into any superposition of coherent states. Also the two-mode squeezing operator working on two Gaussian states will leave the Gaussianity unchanged [30]. These are the Gaussian operation and as noted they cannot turn a Gaussian state into a non-Gaussian state. We also have a Gaussian measurement strategy which is projection onto Gaussian states. This measurement strategy is realized using homodyne detection, but adding this to our toolbox will also not enable us to prepare non-Gaussian states, since this is subject to the same constraints as the other Gaussian transformations.
In a recent experiment Chrzanowski *et al.* have been able to prepare non-Gaussian statistics from Gaussian states using only Gaussian operations and heterodyne detection [100]. They were however not able to conditionally prepare any free-flying non-Gaussian states, thus limiting the applicability of the protocol.

3.2 Non-Gaussian operations

We have seen how Gaussian operations cannot alter the Gaussianity of a state. For this reason non-Gaussian states, such as the coherent state superposition are difficult to prepare in any deterministic fashion. It was shown by Yurke and Stoler that the CSS could be prepared deterministically through the third order Kerr non-linearity [76]. This scheme, however, requires Kerr non-linearities of such magnitude that it is not feasible in presently available Kerr-media. Also states of this type are highly susceptible to loss, and since absorption cannot be neglected in presently available Kerr-media, the ability to extract the CSS' before they decohere is highly limited [99].

The most feasible scheme for producing coherent state superpositions currently known was introduced by Dakna *et al.* [52]. They proposed to conditionally remove a number of photons from a squeezed vacuum state. This is practically done by splitting a squeezed vacuum state, $|\zeta\rangle$, on a beam splitter with vacuum, $|0\rangle$, on the other input port. One output port is detected using a photon number resolving (PNR) detector. The situation is sketched in Fig. 3.1. When this PNR detector

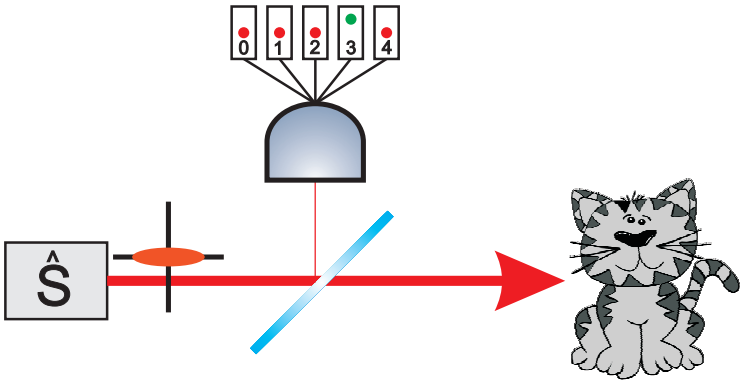

Fig. 3.1: Scheme for subtraction of m photons from a squeezed vacuum state. A squeezed state is split on a beam splitter with transmission T and when a pre-decided number of photons, in this case $m = 3$ is detected the output state is kept. Kitten clipart acquired under open license from www.clker.com

records m photons, the other output port will be prepared in a squeezed vacuum state with m photons removed. The explicit form of the output can be shown to be [52]

$$|\Psi(m)\rangle = \frac{1}{\sqrt{N(m)}} \sum_{n=0}^{\infty} c_n(m) \, |n\rangle \, , \tag{3.3}$$

where the expansion coefficients are given by

$$c_n(m) = \frac{(n+m)!(1+(-1)^{n+m})}{\Gamma[\frac{1}{2}(n+m)+1]\sqrt{n!}} \left(\frac{1}{2}T\gamma\right)^{\frac{n+m}{2}} , \tag{3.4}$$

where T is the transmission of the tap-off beam splitter and $\gamma = \tanh(r)$ is the squeezing parameter. For simplicity, the squeezing parameter is assumed to be real. Looking at $c_n(m)$ it is easily seen that if the number of detected photons m is even (odd) only the even (odd) terms persist in the output. This is easy to accept considering that the input squeezed vacuum state contains only even terms. When an even (odd) number of photons is removed there should be an even (odd) number of photons left. Looking at the photon number distribution, $|c_n(m)|^2$, as function of

the number of removed photons, it is clearly seen how the output oscillates between even and odd terms. The result is shown on the left in Fig. 3.2. From the photon

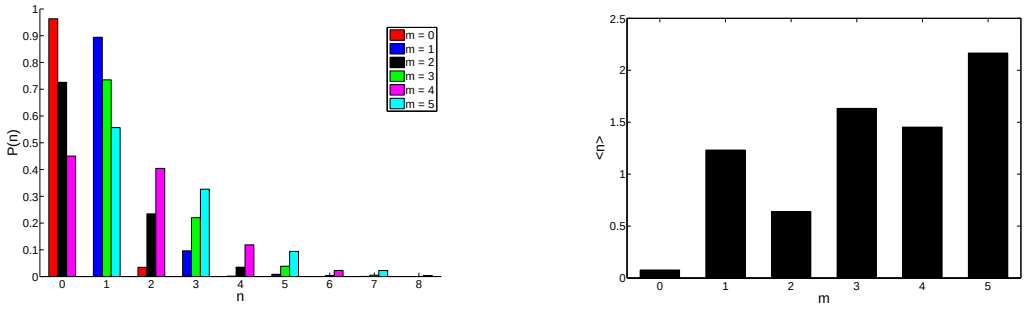

Fig. 3.2: On the left the photon number distribution for m-photon subtracted squeezed state for $r = 0.3$ and $T = 0.92$. When m is even only the even terms persist while only the odd terms persist when m is odd. Also, as the number of subtracted photons increases the higher terms increases at the expense of the lower terms. This results in an increasing mean number of photons, which is also seen on the right figure. Here, the mean number of photons of the output is shown as a function of the number of subtracted photons. Here, it is clear that the mean number of photons increases the more photons are removed from the initial squeezed vacuum state.

number distribution it is seen that as the number of removed photons increase the content of lower photon numbers $0, 1$ decreases. Also shown in Fig. 3.2 is the mean number of photons as a function of removed number of photons. Here, we see the somewhat counterintuitive behavior of increasing mean number of photons, with increasing number of removed photons. The behavior is most clearly seen when going from $m = 0$ to $m = 1$ where the mean number of photons increases by approximately 1. By removing one photon we increase the number of photons by 1. Since the squeezed vacuum state only contains the even terms, we know that once a photon is removed we will have all the odd terms left. This means that the vacuum is removed and the 1-photon Fock state becomes dominant. But since the process is probabilistic, the more photons we remove, the fewer states we have left.
Combining Eqs. (3.3) and (3.4) we see how the output can be written as the superposition of two states ignoring normalization,

$$|\Psi(m)\rangle \quad = \quad \left|\psi_m^+\right\rangle + (-1)^m \left|\psi_m^-\right\rangle, \tag{3.5}$$

where

$$\begin{aligned} \left|\psi_m^{\pm}\right\rangle &= \sum_{n=0}^{\infty} \frac{\sigma_{n,m}}{\sqrt{n!}} (\pm\gamma')^n \left|n\right\rangle, \\ \sigma_{n,m} &= \frac{(n+m)!}{\Gamma(\frac{1}{2}(n+m)+1)}, \qquad \gamma' = \sqrt{\frac{1}{2}T\gamma}. \end{aligned} \tag{3.6}$$

Comparing Eq. (3.6) with the expression for the coherent state superposition, Eq. (2.46), some similarities are apparent. The two constituting superposition states in Eq. (3.6) have a form similar to the coherent state in Eq. (2.32), suggesting that they would be two well separated states in phase space. Looking at the quadrature distributions as a function of phase space angle θ [52],

$$\begin{aligned} \mathrm{pr}(q|m)_\theta &= \frac{(T\gamma)^m}{N(m)2^m\sqrt{\pi\Delta^{m+1}}} e^{-\frac{1-T^2\gamma^2}{\Delta}q} \\ &\quad \times \left| H_m\left(\frac{\sqrt{T\gamma e^{2i\theta} - T^2\gamma^2}}{\Delta} q\right)\right|^2 \\ \Delta &= 1 + T^2\gamma - 2T\gamma\cos(2\theta), \end{aligned} \tag{3.7}$$

we can plot the probability density for $\theta = 0, \pi/2$ and clearly see the two distinct states and the interference between them. These marginals are shown in Fig. 3.3. From the marginal distributions it is clearly seen how the subtraction of m photons

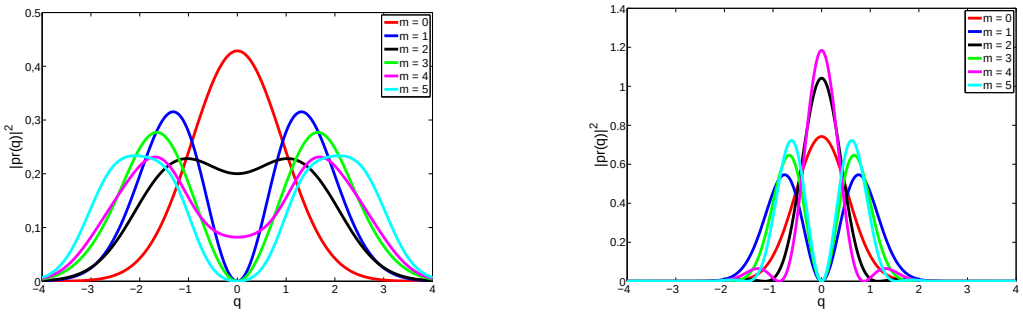

Fig. 3.3: Marginal distributions $\mathrm{pr}(q_{\theta,m})$ for $\theta = 0, \pi/2$ for the state in Eq. (3.3). On the left, $\theta = 0$, the two distinct states of Eq. (3.6) are visible and can be seen to become increasingly separated as m increases. For the conjugate quadrature, $\theta = \pi/2$, clear oscillations are visible. It can be seen how these oscillations alternate between a peak and a dip at the central point as m is even and odd, respectively.

from the squeezed state prepares a state which consists of two distinct states in phase space. The two distinct states are seen as the almost Gaussian shaped "lumps" in the marginal for $\theta = 0$ shown on the left. It is also seen how the lumps move further

apart as m increases. Remembering the comparison of Eq. (3.6) with Eqs. (2.44) and (2.32) this resembles an increase in the amplitude of the individual coherent states in the coherent state superposition. In the marginals for $\theta = \pi/2$ clear oscillations are visible. These oscillations either have one strong central peak when m is even or two equal side-peaks when m is odd.
Looking at the fidelity between the states in Eqs. (3.3) and (2.44), we can get an idea of how well these photon subtracted squeezed states resemble the ideal coherent state superpositions. The fidelity as a function of γ and α is shown for $m = 1, 3, 5$ in Fig. 3.4, [44, 101, 102]. From this it is seen that the state prepared by photon subtraction

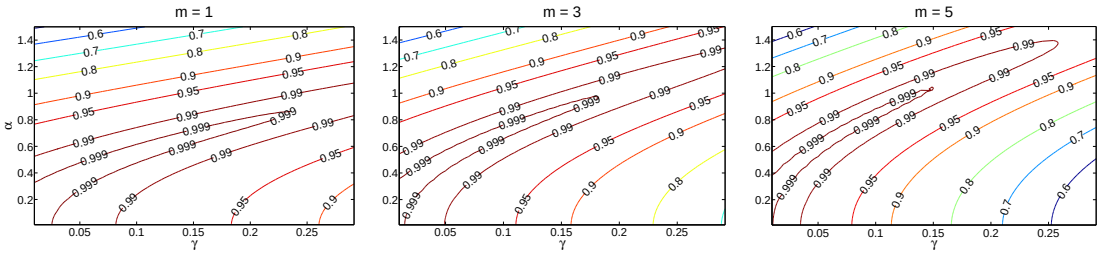

Fig. 3.4: Fidelity between the ideal CSS and the photon subtracted squeezed state for $m = 1, 3, 5$. The fidelity is above 0.99 for optimal settings of squeezing γ and α. Also the ridge of highest fidelity, $F > 0.99$, is seen to move towards higher amplitude for the CSS, while the required squeezing, γ decreases.

from squeezed vacuum can resemble the ideal CSS with fidelities arbitrary close to unity. It is also seen how the potential amplitude of the corresponding CSS increases as m increases, reaching fidelities of more than $F > 0.99$ for $\alpha \approx 1.2$. This photon number resolved subtraction from squeezed vacuum has been demonstrated for pulsed systems [88, 89], with reasonably good results. These results clearly show an increase in the amplitude of the CSS with subtraction of multiple photons.
If we restrict ourselves to the case of only subtracting a single photon, $m = 1$, we can transform the annihilation operator using the squeezing operator and derive an alternative way to prepare the single-photon subtracted squeezed state [102].

$$\begin{aligned} \hat{S}^\dagger(r)\hat{a}\hat{S}(r) &= \hat{a}\cosh(r) - \hat{a}^\dagger \sinh(s) \Rightarrow \\ \hat{a}\hat{S}(r)\left|0\right\rangle &= (\cosh(r)\hat{S}\hat{a} - \sinh(r)\hat{S}(r)\hat{a}^\dagger)\left|0\right\rangle \\ &= -\sinh(r)\hat{S}(r)\left|1\right\rangle \end{aligned} \tag{3.8}$$

Thus, if one photon is subtracted, it is, apart from normalization, equivalent to squeezing a single photon. So, squeezing the single photon is also a viable way to prepare coherent state superpositions with small amplitude.

3.2.1 Realistic conditions

In order to perform the photon number resolved subtraction of photons from the squeezed vacuum a detector capable of distinguishing between m and $m+1$ photons is required, but such a detector is not easy to realize. The Transition Edge Detector (TES) used by Gerrits *et al.* [88] required cryogenic cooling and was only reliable for photon numbers up to $m = 3$. Also, the probability of successful events decreases the more photons we aim to subtract, resulting in highly increasing measurement times. In Eq. (3.8) it is suggested to squeeze the single photon instead of removing one photon from squeezed vacuum. This is a deterministic process and as such more interesting. However, this just shifts the problem as single photons can currently only be prepared probabilistically [49, 72, 103], albeit with fairly high quality.

Imperfect detection

A simpler solution is to use a detector which is only approximately photon number resolving. As described in Sec. 2.4, an avalanche photodiode (APD) is capable of providing almost photon number resolved detection if the mean number of photons is much less than 1. By tuning the squeezing strength, γ, and the transmission, T, of the tap-off beam splitter in Eq. (3.3), one can arrange the conditions such that, once a photon is detected in the APD, with very high certainty only a single photon was present. This limitation is enforced from the fact that, as the photon number increases the APD will start to erase information about how many photons were subtracted. From Eq. (2.70) we have the projection operator for the APD $\hat{\Pi}_{on} = \mathbb{1} - |0\rangle\langle 0|$. This projector can be extended to include the finite detection efficiency η,

$$\hat{\Pi}_{on} = \mathbb{1} - \sum_{m=0} (1-\eta)^m |m\rangle\langle m| \tag{3.9}$$

So far we have assumed that when the heralding detector detects a photon it originated from the squeezed state. As discussed in Sec. 2.4, an APD can also have "false clicks" or dark counts which will be uncorrelated with any optical signal. Such a count will not herald the subtraction of a photon so the output will just be the squeezed state after a loss given by the tap-off beam splitter. In fact any heralding detection by the APD, which is not correlated with the signal state will have the same result. As such, the definition of dark counts can be extended to include more than just the electronic dark counts. Following [104, **?**, 105] it can be interpreted as the total of all counts not correlated with the signal state, and is often referred

to as the "modal purity". Possible sources of such "dark counts" can be stray photons from the surroundings, and, more severely, photons originating from different contaminating squeezed modes, which could also be populated during the squeezing process. The resulting state will be given by Eq. (2.11),

$$\begin{aligned} \rho_{on,s} &= \frac{\mathrm{Tr}_r[\hat{\Pi}_{on,r}\hat{\rho}_{BS}]}{\mathrm{Tr}[\hat{\Pi}_{on,s}\hat{\rho}_{BS}]}, \qquad \hat{\rho}_{dark,s} = \mathrm{Tr}_r[\hat{\rho}_{BS}], \\ \hat{\rho}_{out,s} &= \Theta\hat{\rho}_{on,s} + (1-\Theta)\hat{\rho}_{dark,s}, \end{aligned} \tag{3.10}$$

where Tr_r denotes partial trace over the reflected mode of the state after the beam splitter $\hat{\rho}_{BS}$ and θ is the ration between real and false counts. From this it can be seen that the decrease of the modal purity mixes in a different state than what is intended. This state is the original squeezed state, which has only suffered a loss of $1-T$. In the low reflecting limit $T \approx 1$, the heralded state $\hat{\rho}_{on,s}$ and the "false click" state $\hat{\rho}_{dark,s}$ are almost orthogonal. As shown in the previous section, the heralded state has a large degree of overlap with a small amplitude odd coherent state superposition, while the contaminating state has a large overlap with the orthogonal state, the even coherent state superposition. From this it is obvious that a too low modal purity Θ (or a too high ratio of dark counts) will severely limit the quality of the prepared states. This reduction of quality will be visible in both the fidelity, F, and in the value of the Wigner distribution at the origin, $W(0,0)$. To get an idea of the impact of the combined effect of these imperfections we can investigate the fidelity F and the $W(0,0)$ for various values. From Figs. 3.5 and 3.6 it is seen that the largest

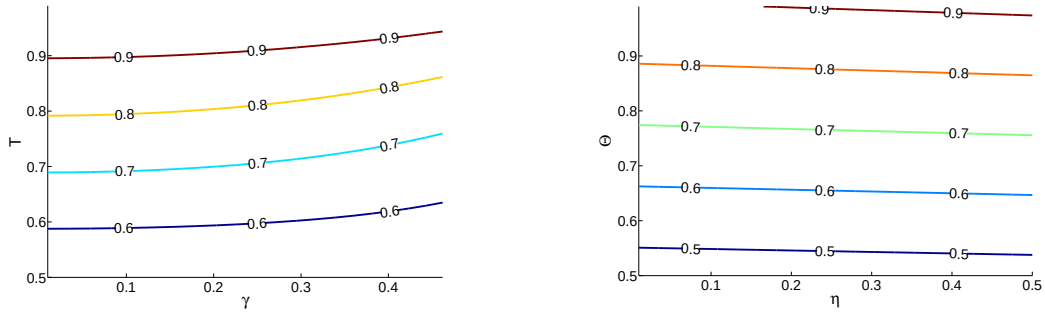

Fig. 3.5: Fidelity, F, as a function of T, γ or Θ, η for the realistic photons subtracted squeezed state. From this it is clearly seen that the largest impact on the quality is coming from T and Θ. Failure to optimize these parameters can have a significant impact on the quality of the states.

impact on the quality of the prepared photon subtracted states is coming from the transmission of the tap-off beam splitter T and the modal purity Θ. Both of these parameters have to be well above 0.5 in order for the prepared states to be of high

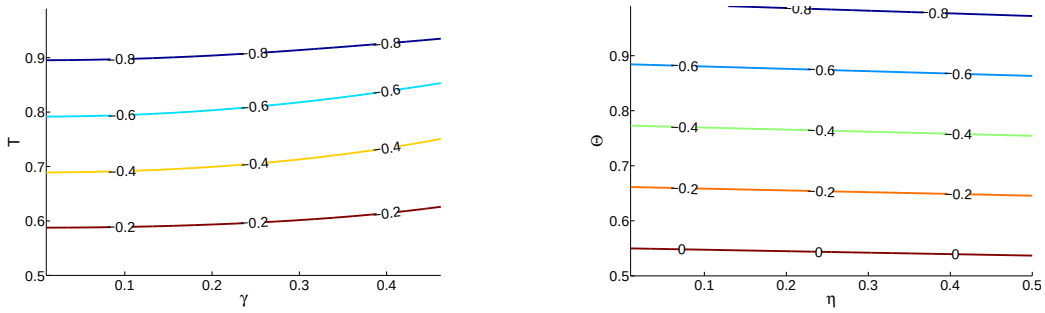

Fig. 3.6: The value at the origin of the Wigner distribution $\pi W(0,0)$ as a function of T, γ or Θ, η for the realistic photons subtracted squeezed state. As for the fidelity it is clearly seen that the largest impact on the quality is coming from T and Θ, which is hardly surprising. Increasing fidelity should lead to larger negativity around the origin since this is a feature of the intended target.

quality.

Imperfect resources

So far the assumption has been that the squeezed state used as starting point is a minimum uncertainty state. Preparing such squeezed states is not easy, and has so far only been done for low degrees of squeezing in CW experiments [66]. In pulsed experiments the minimum uncertainty condition is rarely fulfilled. The result is that the variances are no longer given as in Sec. 2.2.1 and that $\mathrm{Tr}[\hat{\rho}^2] < 1$. According to [71, 64], as the purity of the non-Gaussian state decreases, the possibility to observe negativities in the Wigner distribution decreases with it, however, a general condition on the purity has not yet been derived [106, 107]. Now, since the heralding detector, Eq. (3.9), in itself decreases the purity, it seems reasonable that the input squeezed state must have a certain purity, if we are to have any hopes of preparing states with negativities in the Wigner distribution. What effectively happens is, that the high gain of the SPDC process in pulsed experiments will result in the population of multiple modes around the desired mode. These modes will leak into the right mode and add thermal noise to it [108]. From [109, 50, 110, 111, 112, 105, 63] we have that such a squeezer can be approximated by the real single mode squeezer, the Degenerate Optical Parametric Amplifier (DOPA) followed by a Non-degenerate Parametric Amplifier (NDOPA), which entangles the squeezed mode with an auxiliary vacuum. Finally the auxiliary mode is lost to the environment. The situation is graphically illustrated in Fig. 3.7. This system can be simulated using the density matrix formalism used so far by the 2-mode squeezing operator, Eq. (3.1), working on the squeezed state, $|\zeta\rangle$, and auxiliary vacuum state and then

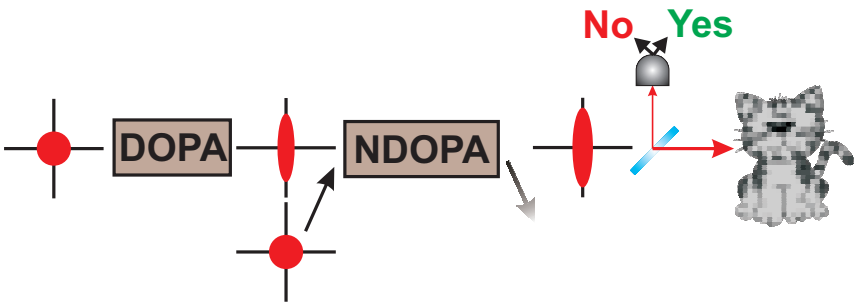

Fig. 3.7: Schematic overview of the system for subtracting photons from a squeezed vacuum state. Squeezed vacuum is generated in a DOPA and excess noise is added by mixing with vacuum in a NDOPA. Then a small fraction of the state is tapped of using an asymmetric beam splitter (ABS). The tapped of mode is then measured using an APD and the output is kept only upon successful heralding. The output state will not be perfect but only resemble the expected CSS. Kitten clipart acquired under open license from www.clker.com.

tracing out the auxiliary mode

$$\hat{\rho} \;=\; \mathrm{Tr}_2[\hat{S}_2(\zeta_2)\,|\zeta_1\rangle\,\langle\zeta_1|\otimes|0\rangle\,\langle 0|\,\hat{S}_2^\dagger(\zeta_2)] \tag{3.11}$$

By adding such a "device" between the squeezer and the beam splitter we can investigate how the purity of the squeezed state influences the benchmarks, F and $W(0,0)$. The results are shown in Fig. 3.8. From these results it is seen that the reduction of the purity of the squeezed state resource has a tremendous impact on the quality of the output photon subtracted states. If the purity drops below 0.9 it is almost impossible to achieve fidelities of more than 0.5 and negativities at the origin of the Wigner distribution. The results also suggest that it is better to have some degree of squeezing with lower purity (Bottom right corner of the 4 graphs). In these regions the effects of a small decrease in purity is not as violent as it appears to be for small degrees of squeezing. From the results derived so far we see that the two most important parameters in a photon subtraction experiment are the model purity, Θ, and the squeezing purity. Systems which to a good approximation can be simulated using this approach have been demonstrated a number of times in recent years [104, 50, 51, 113, 112, 65].

3.3 Gaussian operations on non-Gaussian states

In the previous section it was seen how an approximation to a coherent state superposition could be prepared by subtracting photons from a squeezed vacuum. In Fig. 3.4 it was seen how the amplitude of the CSS could be increased by subtract-

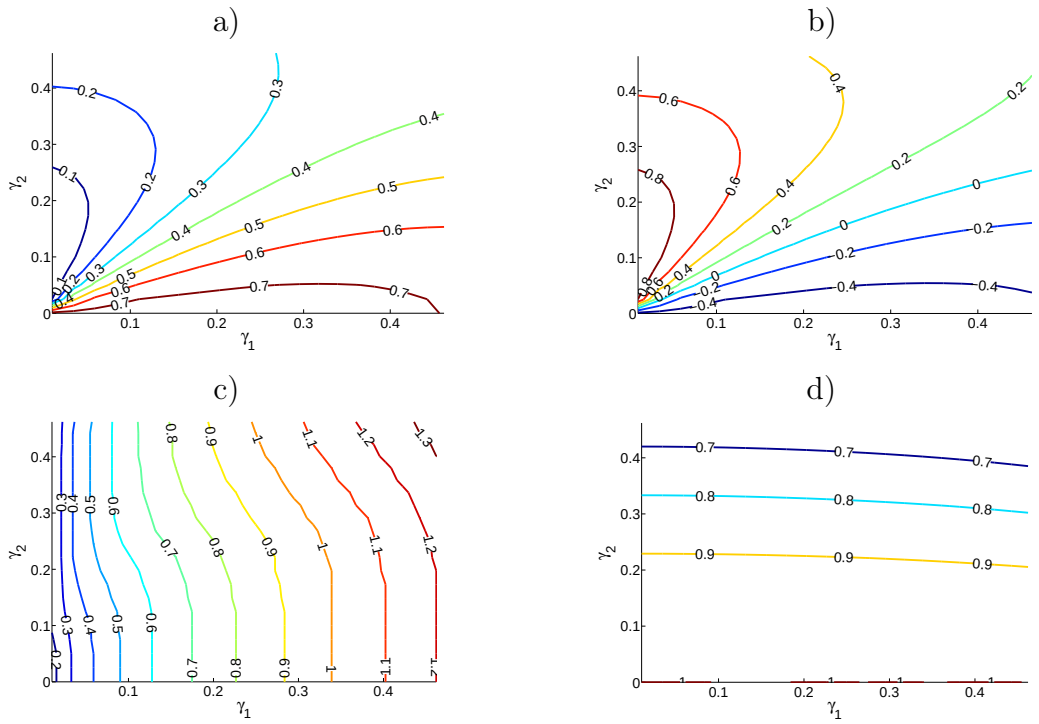

Fig. 3.8: a) Fidelity, b) $\pi W(0,0)$, c) amplitude of CSS and d) purity of input squeezed state as a function of $\gamma_1 = \tanh(r)$ and $\gamma_2 = \tanh(|\zeta_2|)$ for $T = 0.92$, $\Theta = 0.8$ and $\eta = 0.1$. These results indicate that the purity of the squeezed state resource must be above 0.9 if we are to have any hope of being successful in observing negativities at the origin of the Wigner function.

ing multiple photons. This approach can be further optimized using displacements [114]. This approach is, however, difficult [88, 89] so other paths have been pursued, including single photon subtraction assisted by auxiliary fields [115]. These schemes are, however, all somewhat experimentally challenging, so most experimental efforts have been devoted to the subtraction of only a single photon. As was also shown in the previous section, this limits the attainable amplitude of the prepared CSS. From Fig. 3.8 we have that the CSS amplitude cannot be expected to be much larger than $\alpha \approx 1.0$, and this even with somewhat poor quality, $F < 0.7$. So what can be done in order to increase the amplitude of the coherent state superpositions?
From [44] we have that, by mixing two small amplitude CSS' on a balanced beam splitter and performing optimal displaced photon counting on one output, a larger CSS can be prepared. The situation is sketched in Fig. 3.9. Omitting normalization we find from mixing two CSS'

$$|\Psi\rangle_{in} = \left(|\alpha\rangle + e^{i\varphi_1}|-\alpha\rangle\right)\left(|\alpha\rangle + e^{i\varphi_2}|-\alpha\rangle\right) \tag{3.12}$$

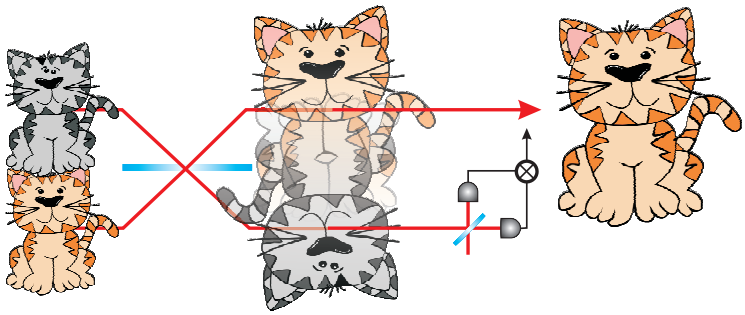

Fig. 3.9: Scheme for increasing the amplitude of a coherent state superposition. If two smaller CSS' are mixed on a balanced beam splitter the output will be an entangled state with content of two larger CSS'. After conditional detection in one mode the second mode will be projected onto the remaining large CSS'. Kitten clipart acquired under open license from www.clker.com

on a 50:50 beam splitter, Eq. (3.2),

$$\begin{aligned} \hat{BS}_1\left(\frac{1}{2}\right)|\Psi\rangle_{in} &= \left(\left|\sqrt{2}\alpha\right\rangle_1 + e^{i(\varphi_1+\varphi_2)}\left|-\sqrt{2}\alpha\right\rangle_1\right)|0\rangle_2 \\ &\quad + e^{i\varphi_2}|0\rangle_1\left(\left|\sqrt{2}\alpha\right\rangle_2 + e^{i(\varphi_1-\varphi_2)}\left|-\sqrt{2}\alpha\right\rangle_2\right) \qquad (3.13) \\ &= \left|\textcircled{S}(\sqrt{2}\alpha,\varphi_1+\varphi_2)\right\rangle_1|0\rangle_2 + |0\rangle_1\left|\textcircled{S}(\sqrt{2}\alpha,\varphi_1-\varphi_2)\right\rangle_2 \qquad (3.14) \end{aligned}$$

Now if it is possible to conditionally detect the $|0\rangle$-state in the second mode, the first mode will be projected into the CSS with a larger amplitude, $\beta = \sqrt{2}\alpha$. For the particular case of $\varphi_1 - \varphi_2 = \pi$, corresponding to opposite parities of the two input states, this can be done without any problems. In this case the CSS in the second mode will be of odd parity and thus contain no $|0\rangle$ contribution. The output state would in this case reduce to

$$|\Psi\rangle_{out} = \left|\sqrt{2}\alpha\right\rangle + e^{i(2\varphi_1-\pi)}\left|-\sqrt{2}\alpha\right\rangle. \qquad (3.15)$$

If the condition $\varphi_1 - \varphi_2 = \pi$ is not met, it is not directly possible to discriminate perfectly in the conditioning mode unless $\alpha \to \infty$. What can be done instead is to interfere the conditioning mode with an auxiliary coherent state with appropriate amplitude, $|\gamma\rangle$,

$$\begin{aligned} \mathbb{1}\otimes\hat{BS}_2|\Psi\rangle_{out}|\gamma\rangle_3 &= \mathbb{1}\otimes\hat{BS}_2\left(\left|\textcircled{S}(\sqrt{2}\alpha,\varphi_1+\varphi_2)\right\rangle_1|0\rangle_2|\gamma\rangle_3\right. \\ &\quad \left. + |0\rangle_1\left|\textcircled{S}(\sqrt{2}\alpha,\varphi_1-\varphi_2)\right\rangle_2|\gamma\rangle_3\right) \\ &= \left|\textcircled{S}(\sqrt{2}\alpha,\varphi_1+\varphi_2)\right\rangle_1\left|\frac{\gamma}{\sqrt{2}}\right\rangle_2\left|-\frac{\gamma}{\sqrt{2}}\right\rangle_3 \end{aligned}$$

(3.16)

If we set $\gamma = \sqrt{2}\alpha$ this state reduces to

$$\begin{aligned} |\Psi\rangle &= \left|\text{S}(\sqrt{2}\alpha, \varphi_1 + \varphi_2)\right\rangle_1 |\alpha\rangle_2 |-\alpha\rangle_3 \\ &\quad + |0\rangle_1 \left(|2\alpha\rangle_2 |0\rangle_3 + e^{i(\varphi_1-\varphi_2)} |0\rangle_2 |-2\alpha\rangle\right). \end{aligned} \tag{3.17}$$

Now, by detecting both mode 2 and 3 using photodetectors and conditioning on detection of photons in both modes, it is possible to perfectly discriminate between the two cases. If photons are detected in both modes, the resulting state at the output will be

$$|\Psi\rangle_{out} = \left|\sqrt{2}\alpha\right\rangle + e^{i(\varphi_1+\varphi_2)} \left|-\sqrt{2}\alpha\right\rangle, \tag{3.18}$$

regardless of φ_1 and φ_2. Thus, we have conditionally prepared a larger CSS, using Gaussian operations and photon detection. This process can work for arbitrarily small input CSS'. Photodetection suffers from not being the most efficient form of optical detection as discussed in Sec. 2.4. This often makes it unpractical in realistic experiments. Homodyne detection can reach efficiencies far exceeding those of typical photodetectors, so we investigated the feasibility of using a homodyne detector instead. In the proposal by Lund *et al.* one output is mixed with a coherent state and detected by two photodetectors. This is reminiscent of homodyne detection, thus suggesting our approach would be justified. Taking our starting point in the two-mode state in Eq. (3.13) and performing homodyne detection, Eq. (2.77), on mode 2 we find

$$\begin{aligned} |\Psi\rangle_{out} &= \left|\text{S}(\sqrt{2}\alpha, \varphi_1 + \varphi_2)\right\rangle \langle X_\theta|\, 0\rangle \\ &\quad + |0\rangle \left(\langle X_\theta|\, \sqrt{2}\alpha\right\rangle + e^{i(\varphi_1-\varphi_2)} \langle X_\theta|\, -\sqrt{2}\alpha\right\rangle). \end{aligned} \tag{3.19}$$

By using

$$\langle X_\theta|\, \beta\rangle = e^{-\frac{1}{2}x^2 - \sqrt{2}e^{-i\theta}x\beta - \frac{1}{2}e^{-2i\theta}\beta^2 - \frac{1}{2}|\beta|^2}, \tag{3.20}$$

we find

$$\begin{aligned} |\Psi\rangle_{out} &= \left|\text{S}(\sqrt{2}\alpha, \varphi_1 + \varphi_2)\right\rangle \\ &\quad + |0\rangle\, e^{-e^{-2i\theta}\alpha^2 - 2e^{-i\theta}x\alpha - |\alpha|^2} \left(1 + e^{i(\varphi_1-\varphi_2)} e^{4e^{-i\theta}x\alpha}\right), \end{aligned} \tag{3.21}$$

where normalization and common factors have been omitted. The task now is to eliminate the second term which is done by choosing x so the parenthesis vanishes. This happens when

$$x = i\frac{\varphi_2 - \varphi_1 \pm \pi}{4\alpha}e^{i\theta} \tag{3.22}$$

Now, it must be a requirement that the "heralding" quadrature eigenvalue x is real. In general we treat α as real number, but for now, without any complications, we can make the substitution, $\alpha = |\alpha|e^{i\varphi_\alpha}$, where $|\alpha|$ is the CSS amplitude and φ_α gives the direction of displacement for the coherent state "lumps". This phase is not to be confused with the φ which gives the parity of the CSS. Making this substitution we find the following constraint on θ

$$\theta = \pm\frac{\pi}{2} - \varphi_\alpha. \tag{3.23}$$

In order for the protocol to be effective, we must always measure the quadrature, which is conjugate to the displacement direction of the coherent states. In order to quantify how this approach matches up to the one presented by Lund *et al.* [44], we would have to compare quality and probability of success. Ideally, both systems should be able to operate with 100% fidelity, assuming perfect detectors. One of our motivations for introducing the homodyne detector into this system is its higher quantum efficiency, and the fact that it is a well established technique when working with this type of states. However, by considering the structure of the states in Eqs. (3.19) and (3.17) it would appear that finite detection efficiency will have less impact on the quality in the protocol based on photodection as opposed to the one based on homodyne detection. If we consider Eq. (3.17) there is only one possibility to detect photons in both mode 2 and 3 and a finite detection efficiency will not change this. Opposite of this is Eq. (3.19) where a finite detection efficiency will cause the two heralding possibilities to decohere into a state where they cannot be distinguished. To investigate this we check the fidelity and probability of success for the two schemes. The results are shown in Fig. 3.10. From these results it can be seen that the fidelity of the homodyne protocol suffers from imperfect detection. The degradation gets worse the lower the detection efficiency. For the case of $\varphi_1 = \pi$, $\varphi_2 = 0$ the effect is present for all values of α. However, when $\varphi_1 = \varphi_2$ it seems that for small $\alpha_{in} \lesssim 0.6$, the scheme works perfectly. This is caused by the fact that in this region, the intended output state is an even CSS with amplitude $\alpha_{out} \approx 1$. This state has a rather large content of vacuum, $|0\rangle$, which is also the

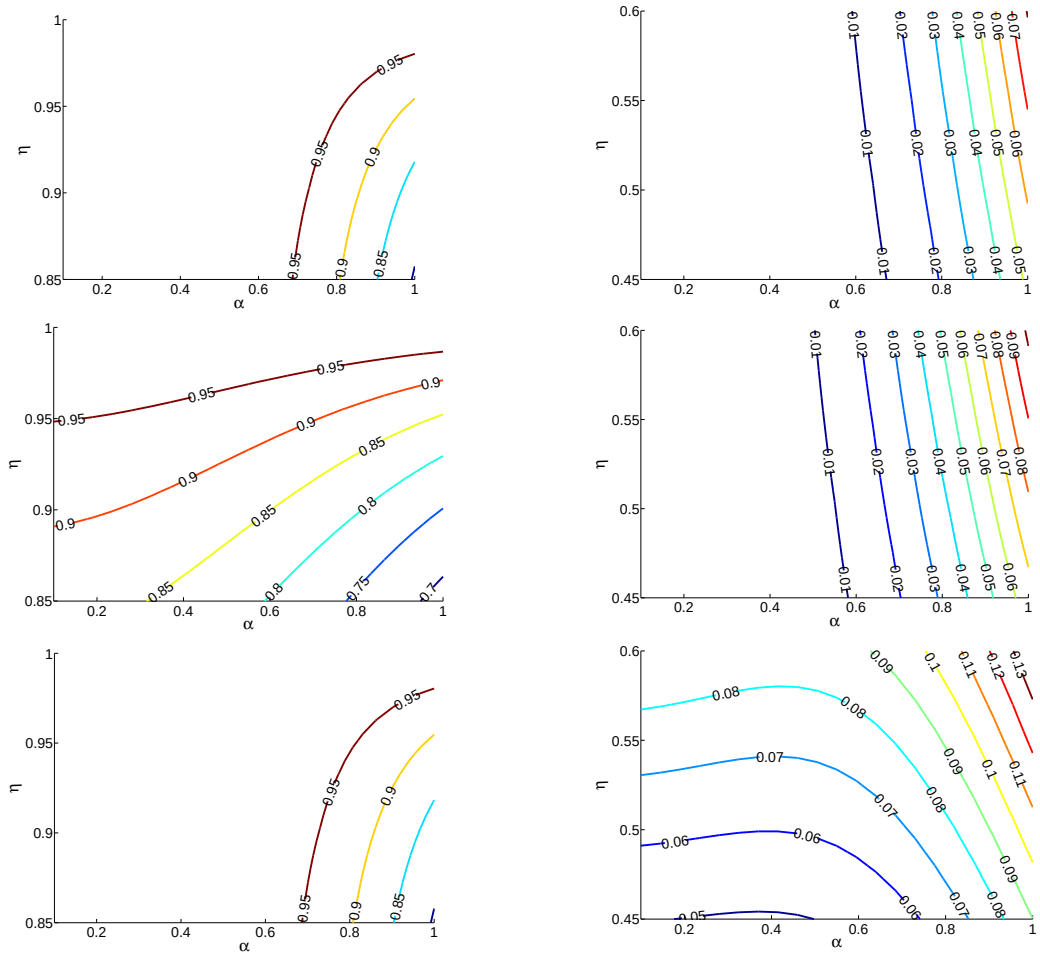

Fig. 3.10: Fidelities (on the left) and success probabilities (on the right) for the protocols for increasing the CSS amplitude. Both a calculated as a function of detection efficiency and amplitude of the CSS. The fidelity is only evaluated for the protocol based on homodyne detection, while the success probability is only calculated for the displaced photodetection. On the top results for the case of $\varphi_1 = \varphi_2 = 0$, in the middle $\varphi_1 = \pi$, $\varphi_2 = 0$ and the bottom $\varphi_1 = \varphi_2 = \pi$. Everything for physically reasonable values of $\eta_{HD} \in [0.85 : 0.1]$, $\eta_D \in [0.45 : 0.6]$ and $\alpha_{in} \in [0 : 1]$.

main content on the output in the lossy scheme. For the photo detection scheme the success probability is seen to be virtually independent on the detection efficiency for the range of α considered here, except for the case $\varphi_1 = \varphi_2 = \pi$. For small $\alpha < 0.5$ the success probability is seen to depend most strongly on the detection efficiency. In this range of input CSS amplitudes the number of photons is almost constant, $\langle n \rangle \approx 2 + 2\alpha^2$, and the detection efficiency around $\eta = 0.5$ plays a role. The fidelity for the photodetector scheme is not shown, but was found to be $F \approx 1$ regardless of detection efficiency. Regarding the success probability this was found to

be virtually constant for the homodyne scheme, for the individual cases, but differs tremendously from case to case. In an experimental setting, the case $\varphi_1 = \varphi_2 = \pi$ is most interesting to us, since the input states $|\alpha\rangle - |-\alpha\rangle$ can be prepared using single-photon subtraction from squeezed vacuum.
This scheme is similar to the protocol proposed by Brask *et al.* to distribute entanglement over large distances [116]. Instead of using CSS' as the input they propose to use single photons. The output of the protocol will in this case take the form

$$|\Psi\rangle_{out} = \langle X_\theta|\, 0\rangle\, |2\rangle + \langle X_\theta|\, 2\rangle\, |0\rangle\,, \tag{3.24}$$

where by tuning X_θ this superposition can be made close to a CSS. By continuous applications of this protocol a large CSS can be "grown" from just single-photon resources.

3.3.1 Realistic conditions

From the results derived previously we see that the homodyne detector is capable of substituting the double photon detection suggested by Lund *et al.* with good results. These results, however, assume perfect input states. This limits the effect of the imperfect detection schemes as shown in Fig. 3.10. In order to see if the scheme is feasible, given physically realistic input states, we simulated it using the resulting states in Sec. 3.2. In the feasibility studies, we assumed the input states to be two identical copies of the states prepared by realistic photon subtraction. Thus we ideally implement the transformation where two $|\alpha\rangle - |-\alpha\rangle$ states are mixed and used to prepare a $\left|\sqrt{2}\alpha\right\rangle + \left|-\sqrt{2}\alpha\right\rangle$ state. This state in itself contains a finite amount of vacuum.
Now, if we have vacuum in the input states we will also have vacuum in the output states, since the protocol cannot remove this vacuum contribution. But when vacuum reduces the quality of the input states it will not necessarily reduce the quality of the output state. For this reason fidelity is not an ideal measure. And since vacuum contamination will most likely always occur in systems such as these, fidelity will always be bounded from below by the vacuum contribution. If we anyway look at the fidelity between the prepared output and the ideal scenario we find the fidelities shown in Fig. 3.11. These fidelities would seem to suggest that the protocol can be expected to produce fairly good results. The fidelities are well above 50% for a large parameter space. However, if the results in Fig. 3.8 and 3.11 are compared we see that, if γ_1 is small compared to γ_2, the input states (upper left corners in Fig. 3.8) will have low fidelity with the ideal state, $F \approx 0.2$, while the output of the

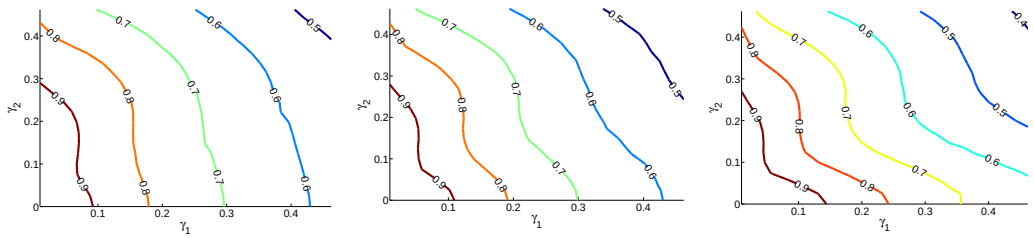

Fig. 3.11: Fidelity between output state prepared by the Lund-protocol using homodyne detectors and ideally expected amplitude increased CSS. Simulated as a function of γ_1 and γ_2 for the squeezing of the original resource state in Fig. 3.8 with $\Theta = 0.5,\ 0.75,\ 1.0$ (from left to right).

"breeding" protocol has a fidelity of $F \gtrsim 0.95$ with the expected state. This is caused by the vacuum contamination. In the input states in Fig. 3.8 this contamination reduces fidelity, while for the output states, this "contamination" basically bounds the fidelity above 90%. An alternative "solution" to quantifying the quality, could be to decompose the prepared state into its eigenstates, thus finding the mixture given in (2.12) and compare the most dominant eigenstate with the ideally expected state. This result is shown in Fig. 3.12. These results give a slightly more detailed picture

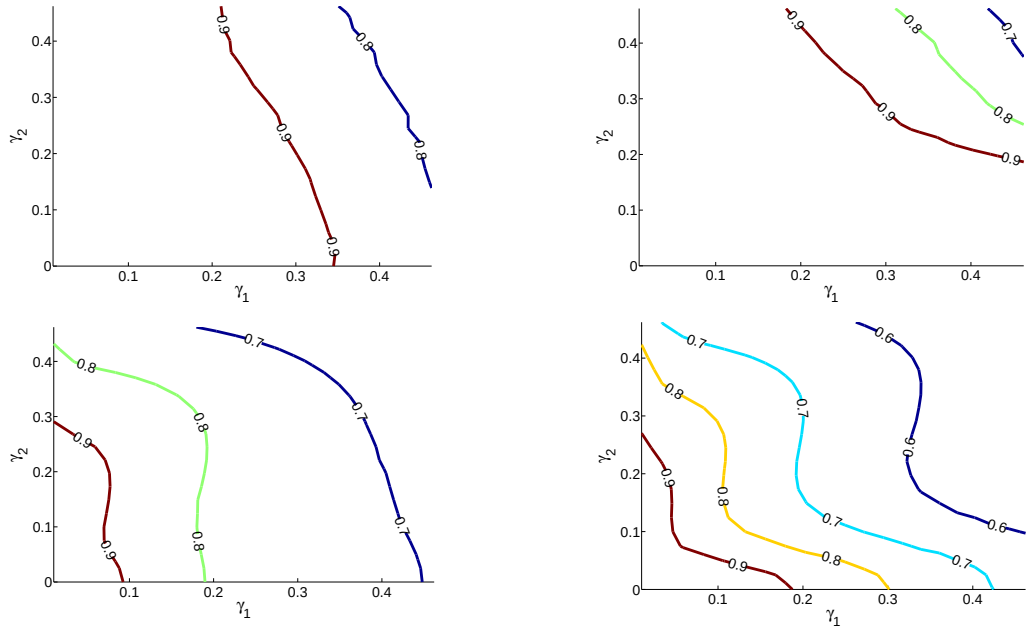

Fig. 3.12: Fidelity of dominant eigenstate and ideally expected CSS, $|\sqrt{2}\alpha\rangle + |-\sqrt{2}\alpha\rangle$ (top) and weight of the eigenstate (bottom). Calculated for $\Theta = 0.5$ (left) and 1.0 (right).

of what is really going on. For the small CSS input states the vacuum contamination is still dominant and can be found inside the eigenstates. Further out in parameter

space the dominant eigenstate start to deviate from the ideal scenario, and the weight of it drops of somewhat fast, meaning the total state is swiftly becoming a mixture. The reason we do not consider the Wigner distribution value at the origin in this case is that it should be positive, even for the ideal scenario, so it can not tell us anything about the non-classicality of the state.

Summary

In this chapter we presented and discussed the protocol for preparing small amplitude coherent state superpositions. The initial ideal protocol presented by Dakna *et al.* [52] was used as the starting point. Then the experimentally more realizable protocol using non-number-resolving APD's as conditioning detectors was presented and analyzed in details. This is the protocol we have implemented experimentally. We attempted to build a model capable of taking into account the potential experimental imperfections we can encounter in this protocol.
Then a protocol for probabilistically increasing the amplitude of the CSS's was presented and discussed. The protocol is an alternative to the protocol presented by Lund [44], where we would attempt to use a homodyne detector instead of the intensity detectors. The quality of the protocol was, however, found to be highly dependent on the quality of the input states. In fact, the requirements on state and detector quality are such that implementation of this protocol could prove a challenge.

Chapter 4

Experimental techniques

In this work much work has been devoted to developing the experimental techniques needed to successfully subtract photons from squeezed vacuum. In this experiment the aim was to combine different optical detection strategies in order to prepare and characterize small amplitude coherent states. We relied on a discrete variable type measurement, the APD, to conditionally prepare the states and a continuous variable type, the homodyne detector, to characterize the states. The complete setup for preparing the initial small amplitude coherent state superpositions, through photon subtraction from squeezed vacuum states is depicted in Fig. 4.1. It is a perfectly

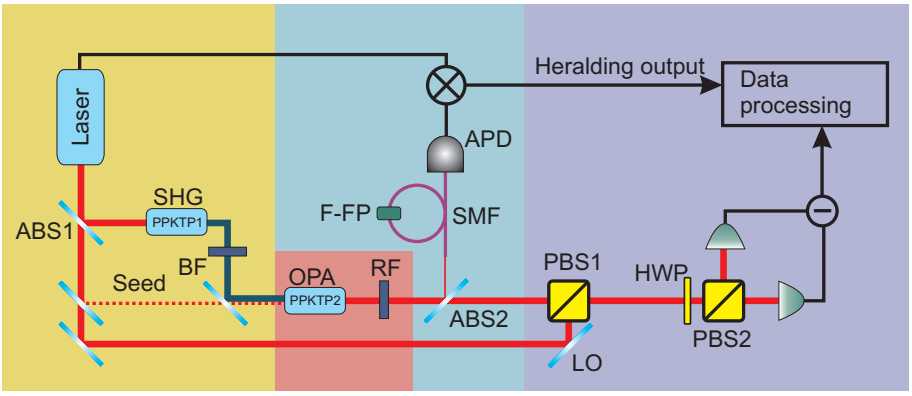

Fig. 4.1: Experimental setup for preparation of photon subtracted squeezed states. All the way to the left the laser and second-harmonic generation (SHG) crystal (PPKTP1). Also the tap-off for a weak seed beam for alignment and calibration. The SPDC crystal (PPKTP2) for preparing squeezed states can be seen at them bottom. In the middle we find the system for tapping off (ABS1), filtering (SMF+F-FP) and detecting photons (APD) and correlating with the laser pulse cycle. Finally on the right the system for characterizing the resulting output is found.

linear setup, which can roughly be divided into four main components: The laser including the second-harmonic generation (yellow), the single-pass Optical Parametric Amplifier (OPA) (red), the tap-off with filtering and APD detection including

electronics to derive the trigger-signal (blue), and finally the homodyne detection system and data acquisition (purple).

4.1 The laser

The laser used to drive the entire setup was a commercial Ti:Sapphire laser purchased from Time-Bandwidth products (TB-P), Switzerland[1]. It was designed for mode-locked operation with pulse durations of a few pico-seconds, with typical values of about 4.6 pico seconds (stated in the test report). The typical wavelength of the laser is 829.7 nm (both specified and measured), but could be tuned in steps of roughly ≈ 2.3 nm in the range from 820-840 nm using a birefringent filter plate. During these tuning steps the pulse length would increase slightly from the 4.6 ps at 829.7 nm to a maximum of 5.1 ps at 822.7 nm. The pulse energy could be as high as 83 nJ, corresponding to a peak power of at least 15 kW. The bandwidth of the laser was specified to be 0.2 nm, corresponding to 87 GHz. However, during the course of this project it has been measured a couple of times with results varying from 70 GHz to 46 GHz. This could be indicative of two things. Either the pulses are closer to being Fourier limited ($f \approx 16$ GHz), or the calibration of the Ångstrom High-Finesse LSA spectrometer[2] was imperfect. An autocorrelator has been purchased to check the temporal profiles of the pulses, but it has not yet been implemented in the laboratory.

As a mode-locked laser, it had an intrinsic repetition rate given by the cavity round-trip time. This repetition rate was 82 MHz, corresponding to a cavity-length of 1.83 m in the standing-wave configuration. When performing quantum information experiments with pulsed laser systems, it is essential that the bandwidths of the detection electronics is larger than the repetition rate, in order to achieve sufficient temporal de-correlation between sequential pulses. In the case of a repetition rate of 82 MHz, this would put tremendous requirements on the electronics, especially the homodyne detectors, see Sec. 4.5. Although experiments have achieved good results under these conditions [72, 117], it was generally much easier to work with repetition rates in the lower MHz or even the kHz range. In order to achieve this, one could employ an external pulse-picker which rejects most pulses, and in this way reduces the repetition rate. This way of reducing the repetition rate is not very energy efficient. Another option was to install an internal cavity dumper. Instead of using light leaked through an output-coupler in the laser, an AOM was installed

[1] See http://www.time-bandwidth.com/ for more information

[2] www.highfinesse.com

inside the cavity. By synchronizing the signal going to the AOM with the internal cavity pulse cycle, the AOM could be made to only deflect light during a fraction of the pulses. This way all light leaving the laser cavity was still utilized, while the remaining light was still trapped inside the cavity for the next pulse. This cavity dumping technique enabled us to downscale the laser repetition rate by factors of 20, 50, 100, 200, 500 and 1000. Typically, we downscaled it by a factor of 100, resulting in a repetition rate of 815 kHz. With this repetition rate, the electronic bandwidths could be as low as a few MHz, which is much more feasible [118, 119]. Typically, the performance of the laser was also found to be best when it was operated at 815 kHz. The pulse-energy should be the highest and the pulses shortest, thus optimizing the peak power.

The laser has, however, presented some problems during the experiments. As the laser is an open system, dust and other dirt had no problems getting into the laser-casing and attaching itself to the optics in the cavity. This would occasionally cause the laser to drop almost 100% in power. This problem was eventually solved by installing a clean-air circulator above the laser. After this was installed, there has only been one significant occurrence of detrimental dust finding its way onto some of the cavity optics. The laser was, however, also somewhat temperature-sensitive. Some of the cavity optics had to be slightly re-optimized during day-to-day operations due to slightly changing conditions. Usually, the problems could be corrected by careful adjustment of the pump beam for the Ti:Sapphire crystal. Another option for optimizing the power was to slightly change the alignment of the mirror focusing the beam onto the SESAM. The optomechanics used in the laser were not generally of poor qualilty, but this re-optimization was nevertheless regularly needed.

The largest problem presented by the laser has, however, turned out to be the cavity dumper. This way of electronically controlling the repetition rate of the laser resulted in noise from the cavity dumper leaking into the laser itself. Although this noise was of relatively low frequency, $\approx$ 70 kHz, the frequency was still comparable to the repetition rate, meaning it proved difficult to remove this noise in the homodyne detectors. Also, at some point the laser power had dropped almost 50%, while the noise had increased to a level, where it was impossible to remove it in the balanced homodyne detectors. After a consultation by the TB-P technician, it was concluded that the cavity-dumper was faulty due to prolonged overheating, resulting from a failed cooling-fan. This resulted in an almost 9-months repair cycle, where the cavity-dumper was serviced twice by the manufacturer. The faulty laser was diagnosed in January 2011 and was not fully operational until the middle of September. By the end of this work, the cavity dumper is back and operational, and the laser is working

close to specifications given during the installation. Only a slight increase in noise originating from the cavity dumper is still present, but at a level where it can be removed by careful balancing, see Sec. 4.5.

4.2 Second harmonic generation

Most quantum optics experiments rely on downconversion to prepare the basic non-classical state, the squeezed state, for use in experiments. Usually, we want the squeezed state to have an optical wavelength in the Near Infra-Red (NIR) since that is where we have the most effective and well-developed detectors available. In order to be able to reach these wavelength ranges, the pump needed for the downconversion must have wavelengths in the green to near-UV wavelength range. Although semi-conductor laser-technology in this wavelength range has matured significantly in recent years, the beam quality and the general laser characteristics do not yet enable usage in quantum optics experiments. We still look to the higher quality solid-state lasers, which are still only available at NIR wavelengths, such as Ti:Sapphire in our case. In order to reach wavelengths in the green to near-UV range we resort to second-harmonic generation. As described in Sec. 2.3 this is the process where a strong coherent field at a low frequency interacts with itself through a non-linear medium to generate a coherent field at the doubled frequency. In many quantum optics experiments, this process is implemented separately from the laser, and as such is not part of the laser. This was also the case in our system. However, from an experimental point of view, it can still be treated as a part of the laser, since it is a strictly classical process used only to prepare a classical pump wave for the quantum experiments.

4.2.1 The basics of second-harmonic generation

The process of second-harmonic generation (SHG) has been extensively treated both in theory and experiments, and is today a commonly occurring experimental technique. Not only in quantum optics laboratories, but in many laser applications in general. As described in Sec. 2.3, one of the primary issues to handle in SHG is that of phase-matching. Phase-matching is the issue of ensuring that the fundamental beam at the NIR wavelength and the SHG beam move with the same phase-velocity inside the crystal. If they do, the SHG light from point A inside the crystal will add up coherently with the SHG light from point B. In this case energy will constantly flow from the fundamental beam to the SHG beam. Since the SHG beam has half

the wavelength of the fundamental beam, the beams are strictly speaking not in phase, but the desired situation is where there are exactly two wavelengths of the SHG within one wavelength of the fundamental. As described in Sec. 2.3 this is generally not the case due to dispersion. The refractive index is a function of the frequency, $n(\omega)$, resulting in a changing relative phase during propagation inside the non-linear crystal.

As described in Sec. 2.3 several techniques exist to eliminate the difference in phase velocities. Often non-linear crystals are birefringent besides being dispersive. Since the refractive index also depends on polarization, it is possible to achieve a situation where the fundamental beam with one polarization has the same phase-velocity as the SHG beam with a different polarization. For the process of SHG from $\lambda = 830$ to $\lambda = 415$ nm, this condition can be fulfilled in the crystal Barium-Borate (BBO), which was used in the first generation of our SHG system. However, BBO suffers from another problem, associated with this type of phase-matching technique. Due to the birefringent nature, the **k**-vector and the Poynting vector **S** do not generally point in the same direction. This results in so-called walk-off, which will elongate the beamprofile along one plane. This can result in highly elliptical beams, which is not desirable when doing quantum optics experiments. For this reason the BBO-crystal setup was quickly abandoned and never studied in detail.

Due to these issues with the BBO crystal, we quickly switched to using a Periodically Poled Potassium Titanyl Phosphate (PPKTP) crystal. In this type of crystal a different type of phase-matching is employed. As described in Sec. 2.3, it is possible to periodically modulate the non-linear crystal in such a way that it induces a "fake" crystal momentum vector, which will fulfill Eq. (2.66). The modulation is done in the sign of the non-linear coefficient, so the relation between the domains is $\chi^{(2)}_{n+1} = -\chi^{(2)}_n$. By doing this, the SHG field generated in domain $n+1$ will have the opposite phase of the field generated in domain n. By modulating with a period Λ, corresponding to the distance in which the field from domain n and the field from domain $n+1$ ends up being 2π out of phase the SHG field will continuously add up coherently. Effectively, this modulation enables a $2\pi/\Lambda$ momentum to be "stored" in the crystal in domain n, and when this wave moves with the optical fields it will be drawn from the crystal in domain $n+1$. Naturally this modulation comes with a cost. The cost is an effective reduction of the nonlinear coefficient with a factor $\chi^{(2)}_{eff} = 2\chi^{(2)}/\pi \approx 0.637\chi^{(2)}$. This corresponds to the first Fourier coefficient of the Fourier expansion of the non-linear coefficient. But the non-linear coefficient also depends on the propagation direction and polarization inside the crystal. When using PP-crystals, typically the orientation is chosen in such a way that the exploited

non-linear coefficient is the highest possible. In KTP, this has a typical value of 33 pm/V, which after reduction becomes $\approx$ 22 pm/V. Comparing with the value that is typically achievable with birefringent phase-matching in KTP crystals, $\approx$ 9.5 pm/V, it is still almost twice as high. And since the conversion efficiency to a good approximation depends on the square of the effective non-linear coefficient, the effect can be as high as a factor of 4. Now, in order to find the modulation period needed to phase-match our desired interaction, $\lambda = 830$ nm $\rightarrow \lambda = 415$ nm, it is just a matter of inserting into Eq. (2.67)

$$\Lambda = \frac{\lambda_{2\omega}}{n(2\omega) - n(\omega)} = 3.82\mu m. \tag{4.1}$$

Strictly speaking, this will only phase-match the plane-wave interaction, since Eq. (2.67) only holds in this case. In typical quantum optics experiments one usually works with beams with Gaussian spatial profiles. In this case this modulation would still be the most optimal [81]. As shown in Sec. 2.3 this modulation period is the same needed for both SHG and DFG. The crystals used in these experiments were all purchased from Raicol Crystals Ltd.

When building an SHG setup, the typical objective is to achieve a high conversion efficiency, η. In pulsed experiments this is typically done in single-pass configuration

$$P_{out,2\omega} = \eta P_{in,\omega}. \tag{4.2}$$

Boyd and Kleinman [81] found the geometry that in principle would optimize the conversion efficiency. However, their solution does not generally take into account the possibility of depletion of the fundamental field. Since the conversion efficiency depends on the input intensity $\eta(I_{in,\omega})$, the behavior when increasing the power or the strength of the focusing is not easily predicted. In pulsed experiments the non-linear gain or conversion efficiency can be of such magnitude that the assumptions of [81] are no longer valid.

For pulsed experiments the effect of Group-Velocity-Mismatch (GVM) also has to be taken into account. Not only do the fundamental and SHG fields have different phase-velocities, which can be compensated by periodic poling, they also generally have different group-velocities, v_g and thus in pulses at two different frequencies will have temporal walk-off. The effect of this is that SHG light being generated in the end of the non-linear crystal will not be temporally overlapped with the light generated in the beginning of the crystal. The longer the crystal, the greater the effect of this temporal walk-off. If one defines a characteristic length, $\tau = t_p/D$,

where t_p is the pulse length of the fundamental field and $D = 1/v_{g,\omega} - 1/v_{g,2\omega}$ is the GVM between the fundamental and SHG fields, then τ is the length required for the temporal walk-off to accumulate to one pulse length. If $L_c \ll \tau$ where L_c is the crystal length, we have from [120, 121] that the conversion efficiency can be expressed as

$$\eta = \gamma U_{in} \frac{L^2}{2z_R}, \quad \gamma = \frac{4\omega^2 d_{\text{eff}}^2}{n(\omega)^2 c^3 \epsilon \lambda_\omega}. \tag{4.3}$$

Here, $z_R = \pi w^2 n/\lambda$ is the Rayleigh range of the fundamental beam and U_{in} is now the pulse energy. Eq. (4.3) is only valid in the limit of weak focusing and assuming no pump-depletion. For longer crystals $\tau < L_c$ the crystal can approximately be divided into slabs of τ thickness and the conversion efficiency can be found by summing across each slab,

$$\eta = \frac{\gamma U_{in}}{2Dz_R} L. \tag{4.4}$$

If we include pump depletion and assume short crystals, with moderate focusing, the conversion efficiency will approximately be proportional to [121, 122],

$$\eta \propto \tanh^2\left(\sqrt{\frac{\gamma}{2Dz_R} U_{in}} L_c\right). \tag{4.5}$$

4.2.2 Implementation

In Eq. (4.5) it was found that, in order to have a large conversion efficiency, the nonlinear crystal has to be long compared with the depth of focus while maintaining that $\tau \lesssim L_c$. In order to find the crystal length that would satisfy this condition, we had to evaluate the GVM for KTP crystals. Given a propagation direction along x with field polarizations along z inside the crystal we found the GVM [123],

$$D_\omega = 1.464 \frac{\text{ps}}{\text{mm}}, \tag{4.6}$$

corresponding to a relative delay of 1.464 ps for every millimeter of crystal. This means that the characteristic crystal length is $\tau \approx 3$ mm. If our crystal length does not greatly exceed this, the conversion efficiency should be well approximated by Eq. (4.5). For this reason, we determined that using 3.0 mm crystals would be, if not an optimal, then at least a acceptable choice. According to Boyd and Kleinman the optimal focusing would yield a depth-of-focus $2z_R = 1.06$ mm corresponding

to a beam waist of $w_0 = 8.7$ µm. We tried various configurations of the focusing into the SHG crystal. With tighter focusing closer to the Boyd-Kleinman optimum we were able to reach conversion efficiencies of more than 50 %. However, this value tended to decrease rapidly over time, and would typically reach 25 % or less after 24h of continued exposure. Also, at the same time the spatial profile of the SHG beam would become distorted and ugly. This degradation was highly irreversible and could only be corrected by moving the crystal, so the beam would trace a new path through it. After the degradation a drop in the NIR transmission of the crystal could also be recorded, which led us to the conclusion that the tight focusing in combination with the high peak-powers damaged the crystal. For a particular case of tight focusing $L_c/2z_R = 0.65$ we measured the conversion efficiency after a 24 h settling time. The result is shown in Fig. 4.2.
Empirical studies [121, 124, 125] have found that the quality in terms of conversion efficiency would be improved for weak focusing of the fundamental field. We found a similar dependence in our system. The final design ended up being with a beamwaist of roughly $w_0 = 90$ µm, corresponding to a depth of focus of roughly 60 mm or 20 times the crystal length. The resulting conversion efficiency is also shown in Fig. 4.2. Both measurements have been fitted to the relation in Eq. (4.5) and can be

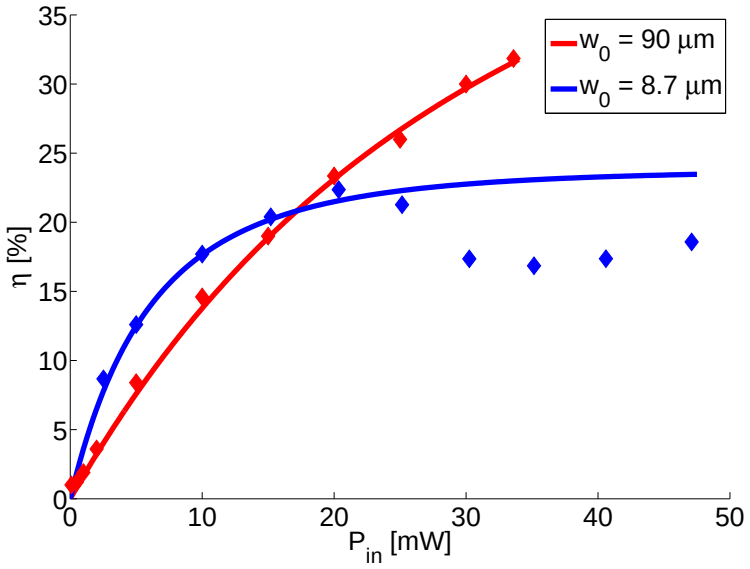

Fig. 4.2: SHG efficiency as a function of input power P_{in}. For the strong focusing the gain is higher for smaller pump powers, but saturation sets in quickly and the gain even drops for higher input powers, $\eta = 23.8\% \tanh^2(0.42\sqrt{P_{in}})$. For the weak focusing it is not even possible to reach the saturation point. The reason why the weak focusing has not been tested for equally high input powers is due to laser problems at the time. For the weak focusing $\eta = 52\% \tanh^2(0.18\sqrt{P_{in}})$.

seen to follow it quite nicely. For the weaker focusing the measured values are seen to follow the prediction all the way through the available powers. For the tighter focusing the model can only match the results until a certain power level. When the input power became too high the conversion efficiency actually started to drop. This was in alignment with previous experiments involving SHG using short pulses [121, 125]. The reason for this drop in conversion efficiency could be caused some gain-induced distortion or diffraction effects. For the tighter focusing the intensity is up to 100 times higher resulting in a dramatic increase in the gain. This increase in gain could cause distortion of the wave-fronts or increased diffraction of the involved fields, causing the phase-matching to be unfulfilled.
Another important aspect of SHG is to maintain a reasonable spectral distribution. For narrow bandwidth systems, such as CW lasers, the SHG bandwidth is comparable to the fundamental bandwidth. For pulsed systems it depends on the spectral form of the non-linear coefficient and the dispersion characteristics. This makes a prediction difficult. Fortunately, we had the option of simply measuring the spectrum using our spectrometer. We found a spectral width of $\Delta\omega_{SHG} = 174$ GHz in early measurements, when the spectral width of the laser was 70 GHz, while the SHG spectral width was found to be 57 GHz for the 46 GHz laser bandwidth. It makes sense that the bandwidth of the SHG field decreases when the bandwidth fundamental field decreases. Given the bandwidth of the SHG and the crystal parameters it is possible to calculate the spectral distribution of the downconverted fields using the theory in Sec. 2.3, see Secs. **??** and 4.4.

4.3 Parametric interaction

The primary workhorse in most quantum optics experiments is the single mode squeezer. A squeezed state is among the simplest non-classical state. It is a Gaussian state and can thus be prepared using only Gaussian operations, and as such it is relatively easy to prepare [5, 30]. Squeezed states have been demonstrated in both CW regimes [17] and for pulsed systems [126, 127]. Today squeezing values exceeding 7dB are regularly being demonstrated in quantum optics labs [19, 18, 20].
When preparing squeezing in CW systems, optical parametric oscillators (OPO's) are typically used. The OPO naturally defines the mode, which is optimally squeezed. In pulsed systems cavities can be utilized, but the implementation is very challenging. For this reason squeezing is usually prepared in single-pass configurations in optical parametric amplifiers (OPA's). In such a system the natural mode selection is done only by the phase-matching of the non-linear crystal and by the pump-

envelope. In this case the number of available spatio-temporal modes significantly increases [128, 129, 130]. Which mode to be considered as the squeezed is determined by the measurement device, which in the present is case the local oscillator (LO) of the homodyne detector. The aim is therefore to match the LO with the desired squeezed mode. This is generally done by injecting a weak coherent seed into the non-linear crystal along with the pump beam. The non-linear interaction between the seed and the pump, facilitated by the non-linear crystal, will cause amplification or de-amplification of the weak seed. From [131] we know that such a system is a phase-sensitive amplifier. Depending on the phase between the weak seed and the strong pump, the weak seed will either be de-amplified or amplified. By continuously scanning the relative phase difference, it is possible to estimate the degree of squeezing being produced in the spatio-temporal mode defined by the seed. The squeezing can be approximated by the de-amplification, while the anti-squeezing can be approximated by the amplification.

We chose to work with PPKTP crystals for the OPA as well. This was motivated by the same considerations as for the SHG system. The high damage threshold and the high non-linear gain makes it an ideal candidate for OPA systems based on pump beams in the visible spectral range. The crystal used in the OPA was a twin to the one used for SHG, meaning a 3 mm crystal with poling period for the $415 \leftrightarrow 830$ interaction. In Sec. 4.4 a deeper discussion on the crystal length will be given.

Extensive theoretical [108, 132, 133] and experimental [134, 135, 125, 136] studies have shown that the amount and quality of the squeezing in pulsed experiments is highly dependent on the focusing of the interacting beams inside the non-linear crystal. These results suggest that better squeezing can be obtained by weakening the focusing of the pump. The reason for this is speculated to be the very high gain available in pulsed experiments. Just as for the SHG system this high gain can cause distortion of the wave-fronts resulting in excess noise in the squeezed state. Also, results seem to suggest that a good choice of ratio between seed and pump focusing would be such that $w_{0,P} = \sqrt{2}w_{0,s}$ [125, 112]. From [108] we have that if $L_c/2z_R \approx 100$, corresponding to $w_{0,P} = 150$ μm and $w_{0,s} = 105$ μm, the optimally highest achievable degree of squeezing should be of the order of 10 dB. By lowering the pump power in this configuration it should be possible to obtain up to 3 dB of squeezing with a purity which is sufficiently high to achieve negativities in the Wigner distribution after subtraction, see Ch. 3. In this configuration we measured both the amplification and de-amplification of a weak seed beam. The result of this measurement is shown in Fig. 4.3.

From [132, 133] we have that the single-pass gain of an OPA for long pulses in the

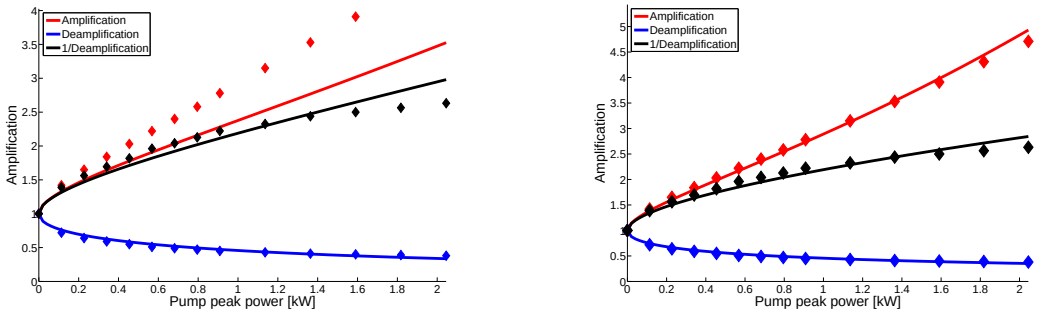

Fig. 4.3: Experimental and theoretical amplifications (red), de-amplifications (blue) and 1/de-amplification (black) for the optical parametric amplifier. Diamonds are measured values and curves are predictions from Eq. (4.7). On the left the theoretical predictions are made using the experimental parameters for the beamwaists. On the right the pump beam waist has been changed in order to fit the theory with the experiment.

weak focusing limit can be approximated by

$$G_{avg,\pm} \approx \frac{1}{t_p w_s^2} \int_0^\infty \int_{-T/2}^{T/2} e^{-(r/w_s)^2} f_s(t/t_p) e^{\pm\Gamma\sqrt{P_0} e^{-(r/w_p)^2} f_p(t/t_p)} r dt dr. \quad (4.7)$$

Here $t_{s,p}$ is the pulse length of the seed/pump respectively, $f_{s,p}(t/t_{s,p})$ the pulse shapes, $w_{s,p}$ the beam waists, P_0 is the pump pulse peak power, T is the pulse separation and r is the radial spatial variable. In this system long pulses mean pulses with a temporal walk-off distance, τ, which is comparable to the crystal length L_c, see p. 59. Γ is the gain constant and can be approximated by

$$\Gamma \approx \frac{4\sqrt{2\pi}(\mu_0)^{3/4}(\epsilon_0)^{1/4} c d_{\text{eff}} L_c}{\lambda_s n_s \sqrt{n_p} w_p}. \quad (4.8)$$

Calculating the amplification and de-amplification for our configuration will result in the curves shown in Fig. 4.3. From these curves it is seen that the model in Eq. (4.7) does not fit well with the measured values. However, if the focusing is changed so the pump beam has a narrower beam waist, $w_{0,P} = 100$ μm, the theory can be made to fit much better with the results. The reason for this discrepancy could be that the pump waist is somewhat difficult to determine precisely. The beam waists for both the seed and the pump were measured using a Thorlabs beamprofiler. However, for the blue pump beam the power had to be decreased in order to avoid overexposure of the sensor. At the time, the only way to decrease the power of the blue beam, was to reduce the amount of NIR light entering into the SHG crystal. This will most likely affect the waist of the SHG field leaving the SHG crystal. By increasing the NIR light entering the SHG crystal a continuous change of the pump

beamwaist inside the OPA crystal could be induced. It is seen that for lower pump powers the theoretical predictions for larger beam waists can also fit the experiment with good agreement. Given the new beam waist of the pump beam, the highest achievable degree of squeezing reduces to about -9 dB according to [108]. From the results it is seen that we reach a de-amplification of roughly 0.4 for a pump peak power of 2 kW, with an amplification of 4.5. The quality of this configuration is not particularly good. But for lower pump powers up to about 1 kW peak power, the difference between the amplification and the inverse of the de-amplification is not too big. This corresponds to almost noise-free amplification/de-amplification. This should indicate that the quality of the squeezing we can prepare in this configuration should be so high that we can expect to see negativities in the Wigner distribution after subtraction.

4.4 Photon subtraction

After the SPDC crystal a collimating lens was used to collect the downconverted light. After this lens a series of filters was used to efficiently remove the pump field. The tap-off was done by a simple uncoated glass-plate, which was anti-reflection coated on the backside thus we simply exploited the Fresnel reflection [137]. This gives a tap-off fraction of roughly 8% with our settings for polarization and AOI. Also a dispersive prism was used to remove any remaining light at or around the pump frequency.

Having prepared a photon subtracted squeezed state we need to characterize it using homodyne detection. In order for this to be efficient the state must be able to interfere effectively with the LO of the homodyne detector. From [**?**] we have that the ability of a prepared state to interfere with a classical field as the LO, will be limited by the spectral and spatial purity of the prepared signal state

$$M^2 \quad \leq \quad P_s, \tag{4.9}$$

where M is the interference visibility and P_s is the purity of the spectral and spatial frequency distribution of the heralded signal state, $\Phi_s(\omega_s, \mathbf{k}_s)$,

$$P_s \quad = \quad \mathrm{Tr}[\Phi_s^2(\omega_s, \mathbf{k}_s)] \tag{4.10}$$

Thus, in order for our prepared state to interfere effectively with our LO, we need it to have a pure spectral and spatial distribution. The distribution $\Phi_s(\omega_s, \mathbf{k}_s)$ is the

reduced part of the Joint-correlation-function

$$\Phi_s(\omega_s, \mathbf{k}_s) \quad = \quad \mathrm{Tr}_i[\Phi(\omega_s, \mathbf{k}_s, \omega_i, \mathbf{k}_i)], \tag{4.11}$$

where it is obvious that if correlations are present, the resulting distribution will have a reduced purity. Thus, in order to have efficient homodyne detection of a photon subtracted state we must optimize the purity of the reduced frequency distribution. This is supposed to be done by filtering, both in the spatial and spectral degrees of freedom.
In order to find the Joint-correlation-function one must in general solve Eq. (2.63). As noted earlier this is highly non-trivial task except in certain regimes. One of these regimes is where dispersion is limited and the pump beam is not focused to strongly, in which case divergence can be ignored. In this case the problem can be solved and the spatial and spectral part of the correlation function will approximately decouple

$$\Phi_s(\omega_s, \mathbf{k}_s) \quad \approx \quad \sigma(\omega_s, \omega_i)\psi(\mathbf{k}_s, \mathbf{k}_i), \tag{4.12}$$

In our system the conditions for this decoupling is to a good approximation fulfilled, so we can treat the spatial and spectral filtering independently, which will be done in the following sections.

4.4.1 Spatial filtering

The spatial filtering of the **k**-vectors is done through a single-mode fiber. In the literature different results for the optimal choice of spatial filtering can be found. Tualle-Brouri *et al.* find that the optimal spatial filtering is where the optical mode coupled to the fibre is much narrower than the pump field, $w_f \ll w_p$ [105], while Aichele *et al.* find the opposite result [138]. However, the system treated by Tualle-Brouri is closer to our system, so for this reason we chose to optimally couple the mode given by the narrow seed beam to the fibre.
This configuration meant that the mode coupled to the fiber was not a plane wave. But the mode used to align interference at the homodyne detector. As such it should define the spatial mode of the prepared photon-subtracted state, which is then interfering with the LO. The seed was coupled with approximately 75% efficiency to the single mode fiber by careful mode-matching with long-focal length lenses in front of the fiber coupler.

4.4.2 Frequency filtering

For the spectral filtering we restrict ourselves to the co-linear, polarization degenerate case. To get an idea of the extent of spectral correlations we will have to consider the spectral dependence of the phase matching function. The phase matching is given by, Sec. 2.3,

$$\Delta k(\omega) \quad = \quad k_p(\omega) - 2k_0(\omega) + K_c, \tag{4.13}$$

where we have explicitly included the dependence of the momentum vector on the frequency, ω. If we restrict ourselves to a limited region in frequency space around the central frequency, $\omega_0 = \omega_p/2$, we can make a Taylor expansion of the momentum vectors

$$\begin{aligned} \Delta k(\omega) \quad &\approx \quad k_p(2\omega_0) - 2k_0(\omega_0) + \left.\frac{dk_p}{d\omega}\right|_{\omega_p} (\omega - \omega_p) - 2\left.\frac{dk_s}{d\omega}\right|_{\omega_0} (\omega - \omega_0) + K_c \\ &= \quad \Delta k^{(0)} + 2\left(\left.\frac{dk_p}{d\omega}\right|_{\omega_p} - \left.\frac{dk_0}{d\omega}\right|_{\omega_0}\right)(\omega - \omega_0), \end{aligned} \tag{4.14}$$

where we have restricted ourselves to the first two terms in the Taylor expansion [139]. Here $\Delta k^{(0)} = k_p(2\omega_0) - 2k_0(\omega_0) + K_c$ is the zeroth order phase matching, which is fulfilled through the periodic poling of the crystal. Using [123] we can find the dispersion characteristics of KTP crystals and evaluate the frequency dependent phase-matching, Eq. (4.14). Inserting this into Eq.(**??**) we can evaluate the frequency correlations on the prepared SPDC state. Following [139] the two-mode SPDC state will look like

$$\begin{aligned} |\Psi(\omega_s, \omega_i)\rangle \quad &= \quad \int\int \sqrt{JSD(\omega_s, \omega_i)}\, |\omega_s\rangle_s\, |\omega_i\rangle_i\, d\omega_s d\omega_i \\ \hat{\rho}(\omega_s, \omega_i) \quad &= \quad \iiiint \sqrt{JSD(\omega_s, \omega_i)}\sqrt{JSD(\omega'_s, \omega'_i)}\, |\omega_s\rangle_s\, |\omega_i\rangle_i\, \langle\omega'_i|_i\, \langle\omega'_s|_s\, d\omega_s d\omega_i d\omega'_s d\omega'_i \end{aligned} \tag{4.15}$$

where $JSD(\omega_s, \omega_i)$ is the joint-spectral-distribution (JSD). For the co-linear SPDC state it can be approximated by

$$JSD(\omega_s, \omega_i) \quad \approx \quad |\alpha(\omega_p - \omega_s - \omega_i)|^2 |\varphi(\Delta k(\omega))|^2, \tag{4.16}$$

where $\alpha(\omega_p - \omega_s - \omega_i)$ is the field pump-envelope and $\varphi(\Delta k(\omega))$ is the phase matching function. Assuming a Gaussian spectrum of the pump field with a power bandwidth given by the measurements in Sec. 4.2 we can evaluate the JSD for the

SPDC spectrum. It is shown in Fig. 4.4, for both 174 GHz and 57 GHz. Looking

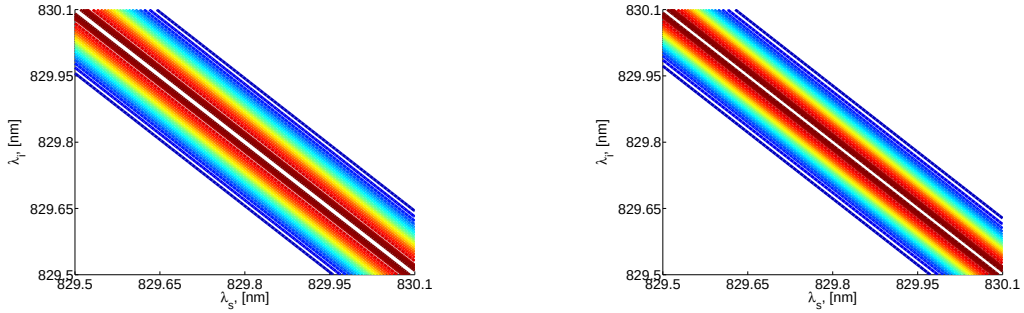

Fig. 4.4: Joint spectral distribution of the SPDC field for KTP crystal with $\omega_p = 415$ nm and $\omega_0 = 830$ nm. On the left the JSD for a pump bandwidth of $\Delta\omega_p = 174$ GHz, which was the "old" measurement and on the right for the "new" measurement of $\Delta\omega_p = 57$ GHz.

at the JSD for the SPDC spectrum, they are clearly highly correlated. Without filtering in front of the APD, any state prepared by triggering on the idler photon will result in a highly mixed spectrum of the heralded state, resulting in an inability to interfere it effectively with the local oscillator of the homodyne detector as stated in Eq. (4.9).

We decided on a commercially available fiber-coupled Fabry-Perot filter, FFP-TF-0830-022G1400, from Micron Optics Inc.[3] intended for use at a central wavelength of 830 nm. The bandwidth of the filter is specified to 22 GHz with a finesse of 1400, resulting in a free spectral range (FSR) of more than 60 nm. This FSR should be sufficient to exceed the bandwidth of the downconversion, eliminating the need for further filtering. This filter type was chosen for its combined effect of narrow bandwidth, large FSR and the fact that it is directly coupled through single-mode fiber pigtails. This should in principle mean that no further filtering is needed. During experiments the filter transmission bandwidth was measured to be somewhere between 22 and 18 GHz, with 18 GHz being the most recent value.

When the APD detects a filtered photon the two-mode SPDC frequency state, $\hat{\rho}(\omega_s, \omega_i)$, reduces through the transformation [138]

$$\hat{\rho}_{h,s}(\omega_s) \quad = \quad \mathrm{Tr}_i[\hat{\Pi}_{APD,F}(\omega_f)\hat{\rho}(\omega_s, \omega_i)], \tag{4.17}$$

where $\hat{\Pi}_{APD,F}(\omega_f)$ is the filtered APD detection operator

$$\hat{\Pi}_{APD,F}(\omega_f) \; = \; \int F_i(\omega_f) \, |\omega_f\rangle \, \langle\omega_f|_i \, d\omega_f. \tag{4.18}$$

[3]See www.micronoptics.com for more info.

Combining these results we arrive at the spectral distribution of the resulting signal state

$$\begin{aligned}\hat{\rho}_{h,s}(\omega_s,\omega_s') &= \iiint \sqrt{JSD(\omega_s,\omega_i)JSD(\omega_s',\omega_i)}F(\omega_i)d\omega_i\,|\omega_s\rangle\langle\omega_s'|\,d\omega_s d\omega_s' \\ &= \iint JSD_F(\omega_s,\omega_s')\,|\omega_s\rangle\langle\omega_s'|\,d\omega_s d\omega_s' \end{aligned} \tag{4.19}$$

where we have used $\langle\omega_f|\,\omega_i\rangle = \delta(\omega_f-\omega_i)$. From this we can calculate a new set of joint-spectral-distributions also taking into account the effect of the filter. If we assume a Gaussian filter function, the result is shown in Fig. 4.5. Looking at

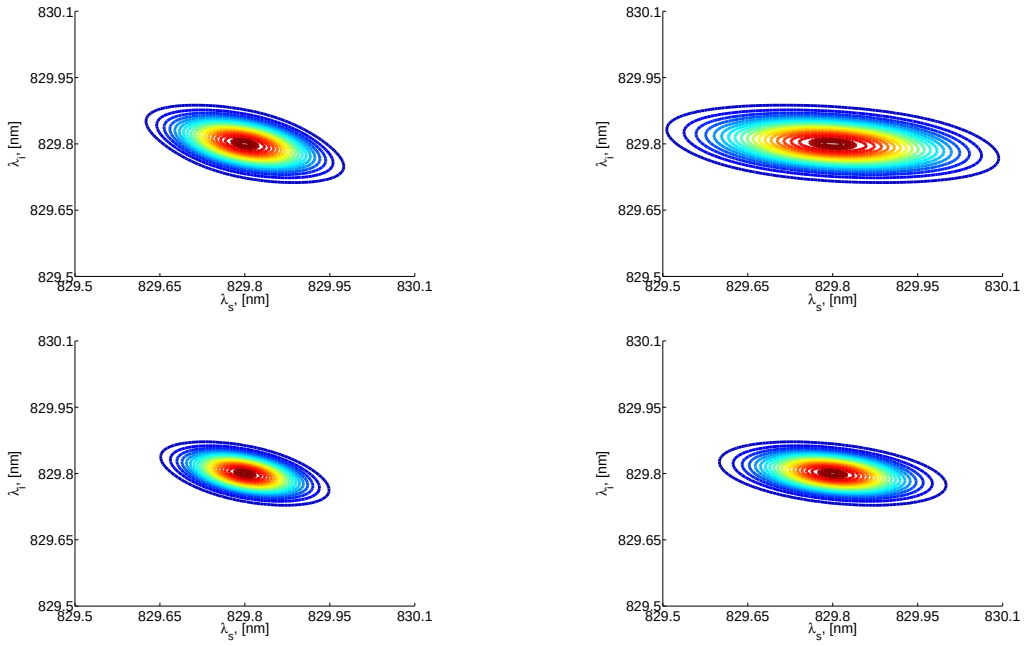

Fig. 4.5: Filtered joint-spectral-distributions for various configurations of experimental parameters. On the left for a crystal length of 3 mm and on the right for a crystal length of 1.5 mm. The upper JSD's are for the older measurements of spectral widths, $\sigma_p = 174$ GHz and $\sigma_f = 22$ GHz, while the lower are for the newer measurements $\sigma_p = 57$ GHz and $\sigma_f = 18$ GHz.

the filtered JSD's it is seen that the JSD depends both on pump/filter bandwidths and the crystal length. Looking at these JSD's it would seem that a shorter crystal should give less correlations between ω_s and ω_i. The ellipse in the JSD tends to be aligned with the major axis along ω_i. A way to quantify the correlations in the JSD is through a Schmidt decomposition [140], which is particularly useful in this situation.

$$|\Psi_F(\omega_s,\omega_i)\rangle = \int \tilde{\xi}(\tilde{\omega}_j)\,|\tilde{\omega}_j\rangle_s\,|\tilde{\omega}_j\rangle_i\,d\tilde{\omega}_j, \tag{4.20}$$

where the Schmidt coefficients $\tilde{\xi}(\tilde{\omega}_j)$ are found as the square-roots of the eigenvalues of the reduced density matrix, which can be found using the partial trace. It then follows that the purity is

$$P_{h,s} \quad = \quad \mathrm{Tr}[\hat{\rho}_{h,s}^2] \quad = \quad \int \tilde{\xi}^4(\tilde{\omega}_j) d\tilde{\omega}_j, \tag{4.21}$$

We numerically investigated the purity of the reduced state as a function of crystal length for the parameters used in Fig. 4.5. Looking at the result in Fig. 4.6 it is seen

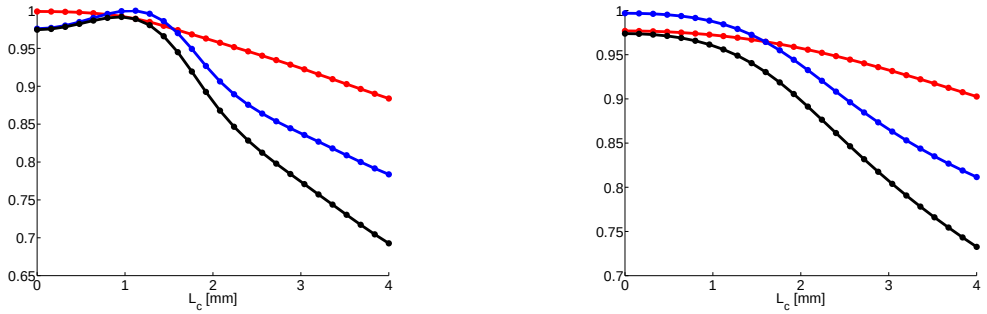

Fig. 4.6: Square-root of spectral purity of reduced state (red), spectral overlap with local oscillator (blue) and product of these (black). On the left (right) the result for the "old" ("new") case. For the old (new) case an LO bandwidth of 70 (46) GHz is assumed. The integration is done numerically over the window used in Fig. 4.5 with a discretization of 100×100.

that the spectral purity drops as the crystal becomes longer. Now, a high purity is desired, but this will be of no use if it is not spectrally matched to the LO. For this reason it seems justified to also consider include spectral overlap with the $LO(\omega_s)$

$$m \quad = \quad \frac{(\int \sqrt{\varphi(\omega_s) LO(\omega_s)} d\omega_s)^2}{\int \varphi(\omega_s) d\omega_s \int LO(\omega_s) d\omega_s}$$

where

$$\varphi(\omega_s) \quad = \quad \langle \omega_s | \, \hat{\rho}_{h,s}(\omega_s', \omega_s'') \, | \omega_s \rangle \, .$$

Thus the limit on the homodyne detection efficiency will be

$$M^2 \quad \leq \quad P_{h,s} \times m$$

as a benchmark function. Using this we see that our choice of using a 3mm long crystal is far from optimal. According to Fig. 4.6 the homodyne detection efficiency can not exceed about 75% for a crystal of 3mm. Unfortunately, this was the only

crystal length available at the time. Now new SPDC crystal, with a length of 1.5mm, has been installed and is being tested in the experiment.

4.4.3 Electronics

The APD used for the experiment was the Perkin-Elmer SPCM-AQR-16-FC avalanche photo diode[4]. This model had an intrinsic dark-count rate of < 25 s^{-1} and a detection efficiency of about 60% at our operational wavelength. The dark count rate was verified through a measurement and was found to be 20 ± 4 s^{-1}. The detector was fiber-coupled, meaning the fiber pigtail of the Fabry-Perot could be coupled directly to the APD. This APD will give a 35 ns TTL pulse upon a detection of a photon. In order to optimize the data-acquisition and to reduce the effect of spurious detections by the APD a system of electronics was utilized. The overall target was to ensure that once a photon was detected by the APD it could with very high probability be attributed to subtraction from the squeezed vacuum. This was done by only allowing counts to be registred when the laser cavity dumper was active. This was done by correlating the APD and the cavity dumper signals through a coincidence circuit. But before this, both signals were shaped and stretched using a discriminator. The signals after the discriminator were both NIM pulses of roughly 75 ns length, which was also chosen as the coincidence window of the logical circuit. This would mean that APD detection events would only be accepted within about 1/15'th of the time. This should give a 15 times decrease in the intrinsic dark counts. The corrected dark count rate was found to be about 1.5 ± 0.5 s^{-1}, thus not entirely 15 times lower, but still a significant decrease.

4.5 Time-domain balanced homodyne detection

In Sec. 2.4.2 the apparent simple nature of homodyne detection was described. However, the real story is far from being that simple. As with any other aspect of quantum optics, there are many effects that need to be taken into account when doing actual experiments.

4.5.1 The detector

The detector used in these experiments is based on the design by Hansen *et al.* [118] and was modified by Dr. In the continuous wave regime the electronic signal from

[4]See www.perkinelmer.com for more information

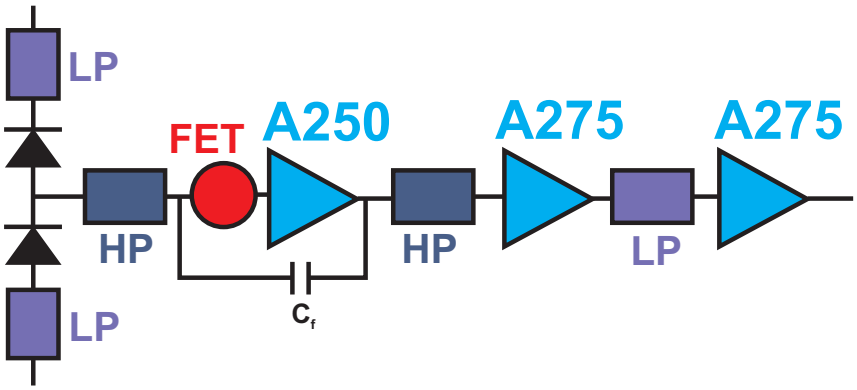

Fig. 4.7: Schematic overview of the detector layout for the homodyne detector. The photocurrents from the photodiodes are subtracted right away and sent through a high-pass filter (HP). Then it is amplified through a charge-sensitive preamplifier (A250) with a FET, where the gain is determined by a feedback capacitor, C_f. The output voltage is then filtered (HP+LP) and amplified (A275) before the output is derived.

the individual photodiodes remains fairly low, meaning it can often be amplified without saturation effects if high-quality amplifiers are used. We work with pulsed lasers, however, and as such are faced with some challenges if we were to do this. While the average electronic signal from the photodiodes is usually substantially lower than what can be seen in the CW case, within a short time window the signal will be much larger. This large signal is much more difficult to amplify without saturation effects, meaning we would like to remove the classical amplitude before any amplification. This is done by detecting the two outputs from the balanced beam splitter by photodiodes placed closely together and immediately afterwards taking the difference current. A bias is applied to the two photodiodes to increase the quantum efficiency and the temporal response. The bias is low-pass filtered to prevent high-frequency components from leaking into the amplifying stage. Right after the photodiodes we already have the difference current, which we saw in Eq. (2.73) is directly proportional to the quadrature we want to measure. Now all we have to do is to amplify this remaining difference current. This is done by a design employing the AMPTEK A250/A275 amplifiers, with appropriate filters in between[5]. The first filter of the amplifier is a high-pass filter for the charge accumulated at the subtraction point. The filter has a cut-on frequency of roughly,

$$f_c = \frac{1}{2\pi RC} \approx 35\text{Hz}. \tag{4.22}$$

[5]See www.amptek.com for more information

The output of this charge high-pass filter is directly fed to a Field Effect Transistor (FET). The FET feeds the charge to the A250, charge-sensitive pre-amplifier. This amplifier converts a small charge change at the input to a big voltage change at the output. The bandwidth of this amplifier is specified to be roughly 300MHz, with a gain determined by a feedback capacitor C_f. This gain scales with the feedback capacitor like

$$G_{\mathrm{A250}} \quad \propto \quad \frac{1}{C_f}. \tag{4.23}$$

After the A250 amplifier a voltage high-pass filter is used. The pass-function for this filter is displayed on the left in Fig 4.8 for various component configurations. The

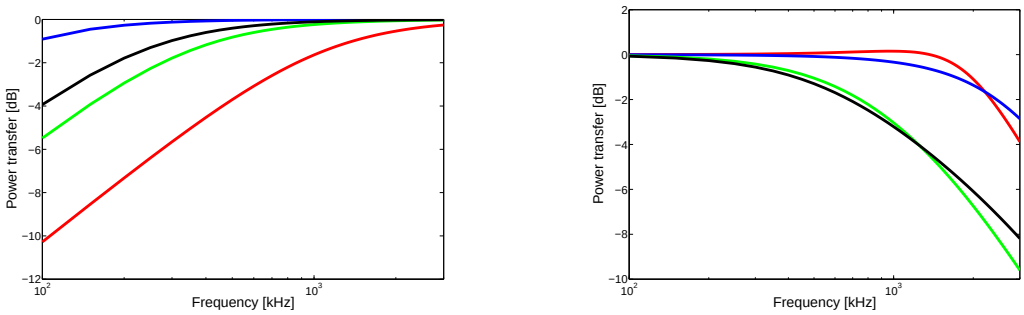

Fig. 4.8: Filter functions for high- and low-pass filters of the homodyne detector. On the left the filter function for the high-pass filter and on the right for the low-pass function for various configurations. For more details on the filter functions and component configurations see Appendix A.1.

configuration used in this particular case has a cut-on frequency of roughly

$$f_c \quad \approx \quad 600\mathrm{kHz}. \tag{4.24}$$

After this high-pass filter another amplifier is inserted. It is a AMPTEK A275 pulse amplifier. It has a gain-bandwidth of up to 200MHz, with the gain remaining higher than 40dB up to 1MHz. After this second amplifier a low-pass filter is inserted. This low-pass filter is made up of an L-R-C circuit. The pass-function for this filter is plotted on the right in Fig. 4.8 for various configurations. The configuration we ended up using had a cut-off frequency of

$$f_c \quad \approx \quad 2.5\mathrm{MHz}. \tag{4.25}$$

We know our optical system has a repetition rate of 815 kHz so we want our detector to be able to see this frequency and an area around it. The chosen filter configu-

rations were made at a time when our understanding of the inner workings of this detector was limited. And as such they were based on the configuration used at MPI Erlangen, from where we borrowed the layout. This means that they are most likely not optimal, but as we will see in Sec. 4.5.5 the final layout does work in a satisfactory manner. The final detector was assembled on a small printed board and inserted in a closed aluminum box, only with holes to the photodiodes. This was done to limit noise from electronic pick-up from the environment. The final physical detector is shown in Fig. 4.9. We tested the gain of the detector configuration for

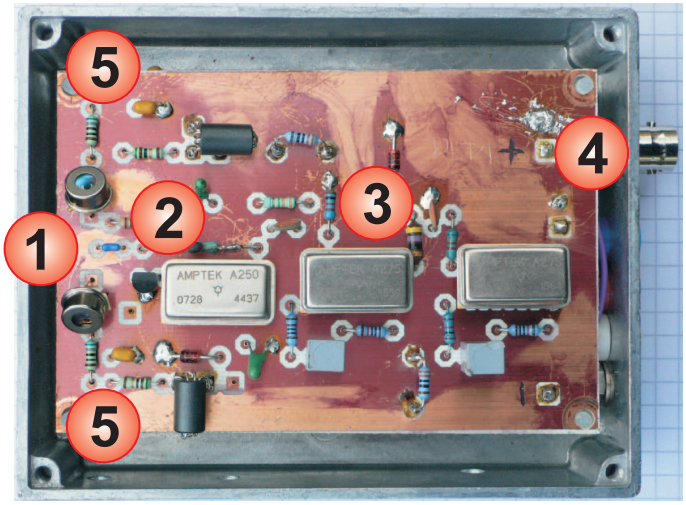

Fig. 4.9: The physical board layout of the resulting detector. On the left the bias arms (5) and the photodiodes with the subtraction point (1) are shown. The signal path can be followed through the FET and the charge-sensitive preamplifier (2) and the highpass- and lowpass-filters with the pulse amplifiers (3) to the output (4).

various choices of feedback capacitor for the pre-amplifier, C_f, basically putting Eq. (4.23) to the test. We measured the gain by passing a fast-oscillating charge through the first low-pass filter, by applying an AC signal of 815kHz across it. By varying the voltage step we could vary how much charge was sent through the filter to the FET. By recording the peak-voltage of the output, it is possible to define a gain in terms of pulse height versus input charge. We measured for a range of feedback capacitors ranging from 0F to 4.7pF. The output peak voltage as function of input charge is shown in Fig. 4.10 On the left it is seen that the output peak voltage depends virtually linearly on the input charge until saturation sets in. The saturation sets in around 6V, which is the maximum output voltage the A275 amplifiers are capable to provide. It can also be seen that the gain is increasing when the feedback capacitance is made smaller. However, we also see that the gain does not "blow up" when the capacitance vanishes, suggesting that a resistor placed in parallel with the

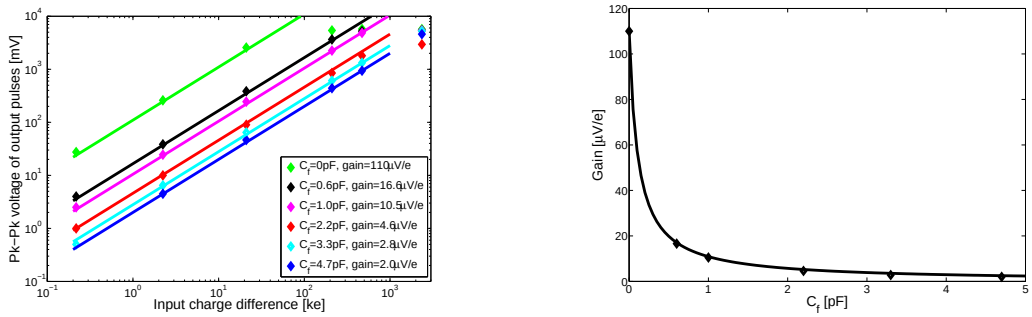

Fig. 4.10: On the left the output peak voltages (in mV) of the output pulses is shown as a function of the input charge (in ke). It was measured for feedback capacitances of $C_f = 0$ pF with gain of $G = 110\mu$V/e (green), $C_f = 0.6$ pF with gain of 16.6μV/e (black), $C_f = 1.0$ pF with gain of 10.5μV/e (pink), $C_f = 2.2$ pF with gain of 4.6μV/e (red), $C_f = 3.3$ pF with gain of 2.8μV/e (cyan) and $C_f = 4.7$ pF with gain of 2.0μV/e (blue). The output increases linearly in input charge up to about 6V, where saturation effects set in. On the right the gains are shown as a function of feedback capacitance. The curve is a fit based on Eq. (4.26) with $A = 110\mu$V$\cdot$ pF/e and $C_\epsilon = 0.11$ pF, which is seen to follow the gains extremely well, thus confirming the dependence in Eq. (4.23).

feedback capacitor acts as a small parasitic capacitance on its own. By fitting the gain to the form

$$G = \frac{A}{C_f + C_\epsilon} \tag{4.26}$$

we can find the extra capacitance, C_ϵ, of the resistor. This is done on the right in Fig. 4.10, and can be seen to follow the gains with good accuracy for values of $C_\epsilon = 0.11$ pF and $A = 110\mu$V$\cdot$ pF/e. The final choice of feedback capacitor ended up being $C_f = 1.0$ pF.

4.5.2 Balancing the detector

From Eq. (2.73) we have the importance of balancing the homodyne detector in order to remove any classical signal from our measurements. In the case of CW optical systems, this is essentially done by fulfilling the requirements given in Sec. 2.4.2. However, in the pulsed case, we also have to take into account the temporal response of the photodiodes as well. Even though two photodiodes are specified to be identical, small differences might be present in the response to fast optical signals. Small, nonlinear effects in the quantum efficiency or other temporal distortion effects can result in significantly different responses to otherwise identical optical pulses. On the left in Fig. 4.11 a typical part of a pulse train is shown. The pulse amplitude is

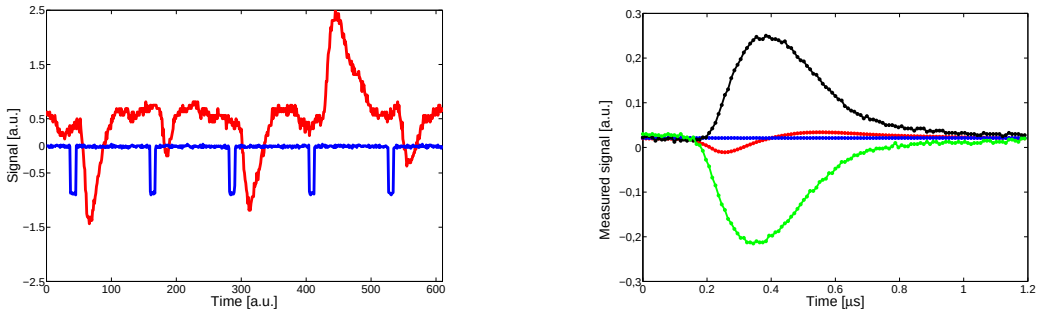

Fig. 4.11: On the left a typical pulse train is displayed (red). It can be seen that the pulse amplitude is fluctuating around some mean value, which ideally should be zero. However, it can be seen that a small offset is present. Shown is also the trigger signal which is derived from the cavity dumper for the laser. It marks the beginning of a pulse window and can thus be used to extract the length of the pulse window, $T \approx 1.2\mu$s. On the right about 65000 pulses have been measured and averaged pointwise (red). The result is shown together with the corresponding electronic noise (blue) and the pulses with highest (black) and lowest (green) amplitudes.

seen to fluctuate around some mean value. Ideally, this mean value should be 0, but, due to a small offset in the detector, it is slightly different. On the right in Fig. 4.11 65000 pulses have been averaged pointwise. The result is the red curve. Comparing this curve with the electronic noise, it is seen that a small ripple is present. This ripple is caused by a slight, uncompensated imbalance in the temporal response of the two photodiodes. Comparing the ripple with the maximum/minimum pulses, it is, however, seen that it is not so significant. Experience showed us that the size and shape of this ripple was very much dependent on the bias voltage applied to the photodiodes as well as how the light was focused onto the photodiodes. This was to be expected due to the extreme circumstances in which we use the photodiodes with short optical pulses.

4.5.3 Noise characteristics

One of the primary characteristics of any detection circuit is the noise characteristics. This is also the case in any HD circuit. In a homodyne detector there are two main different types of noise. As with any other electronic system, a HD circuit will have electronic noise. This is the intrinsic noise that we measure from the detector when it is completely isolated from any optical signals. Electronic noise typically has a significant bandwidth, which can often be much greater than the actual bandwidth of the detector. In the case of our detector the signal is drawn directly from the output of the last amplifier. Although the A275 has excellent noise characteristics, this will inevitably add some high-frequency electronic noise to the output.

The second main type of noise is from the quantum fluctuations of the measured light, $\mathrm{Var}(i_-)$, as given in Eq. (2.74). This type of noise is what we are really interested in measuring and is mostly referred to as the signal- or shotnoise. We know from Sec. 2.4.2 that shotnoise is what is measured by a balanced homodyne detector when there is no signal being mixed with the LO. It is important to know the relation between the spectra of electronic noise and shotnoise for a given homodyne detector. The spectral distribution of both the electronic noise and the shotnoise can formally be found by the Wiener-Khintchine theorem,

$$S_e(\nu) = \int_{-\infty}^{\infty} \langle i_e(t) i_e(t+\tau) \rangle e^{2\pi i \nu \tau} d\tau, \tag{4.27}$$

$$S(\nu) = \int_{-\infty}^{\infty} \langle i_-(t) i_-(t+\tau) \rangle e^{2\pi i \nu \tau} d\tau, \tag{4.28}$$

where ν is the frequency. We have from [141] that the ratio between the variance originating from electronic noise, $\mathrm{Var}(\hat{q}_e)$, and the variance of a measured vacuum state, $\mathrm{Var}(\hat{q}_0)$, can be translated into an reduction in quantum efficiency of the homodyne detector,

$$\eta_e = 1 - \frac{\mathrm{Var}(\hat{q}_e)}{\mathrm{Var}(\hat{q}_0)}. \tag{4.29}$$

If the detector bandwidth is sufficiently high compared to the bandwidth of the signal, this ratio can be approximated by the clearance of the detector [142]

$$\eta_e \approx 1 - \frac{S_e(\nu)}{S(\nu)}. \tag{4.30}$$

However, for pulsed systems the story is a bit more complicated. In this case the individual LO pulses have a temporal shape which is in no way resolvable by the electronics. The only things we can hope to resolve are the individual pulses, in order to avoid cross-talk. For this we need a bandwidth which is greater than the repetition rate of the LO. For the case where the bandwidth is sufficiently high compared to the repetition rate, Eq. (4.30) can be reformulated approximately like

$$\eta_e \approx 1 - \frac{\Delta T}{T} \frac{S_e(0)}{S(0)}, \tag{4.31}$$

where ΔT is essentially the length of the electronic pulse resulting from an optical pulse and T is the time between individual pulses. Looking at Fig. 4.11 we can get an idea of how to find these two timescales. The time between pulses, T, can be

extracted using some reference signal, either from the laser or directly measured in the setup by an extra photodiode. The integration window, ΔT, is some part of the pulse shown in Fig. 4.11.
Looking at the spectrum of a balanced detector we can get an idea of the impact of the ripple. The spectrum is measured with an LO power of 10μW, corresponding

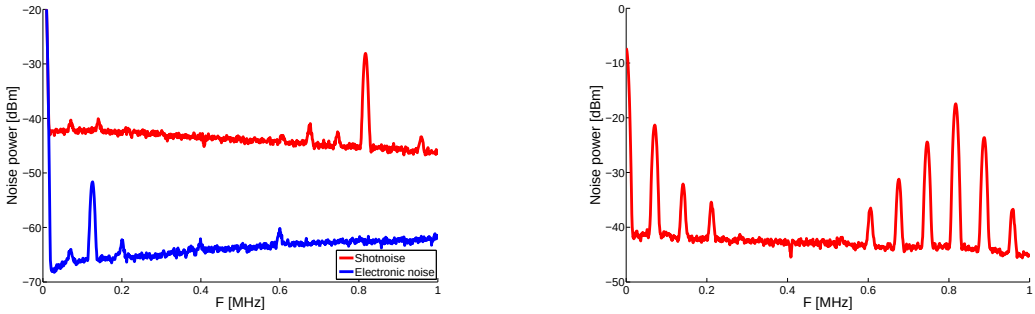

Fig. 4.12: On the left a spectrum from a properly balanced homodyne detector (red) as well as the detectors electronic noise spectrum (blue) shown up to 1MHz. The shotnoise spectrum was measured with an LO power of 10μW corresponding to 50 million photons per pulse. The peak in the shotnoise spectrum is located at 815kHz, which is the laser repetition rate, and is this caused by a slight imbalance in the subtracted pulsesignal, as seen in Fig. 4.11. On the right a spectrum of an improperly balanced homodyne detector. The extra peaks are located with spacing of about 70khz around the 815kHz repetition rate. All spectra were measured with a resolution bandwidth of 9kHz.

to 50 million photons per pulse, with a resolution of 9kHz and averaged over 100 traces. In the spectrum on the left we see a clear peak at 815 kHz which is exactly the repetition rate. This is caused by the slight imbalance also presented by the ripple in Fig. 4.11. The rest of the spectrum is typical for shotnoise though, being virtually flat over the entire frequency range. The electronic noise spectrum is seen to contain slightly more power at the frequencies around 1MHz than for lower frequencies. Comparing the shotnoise spectrum with the electronic noise spectrum, we can see that the clearance is at least 15dB for the entire frequency range here. On the right of Fig. 4.12 a spectrum of an improperly balanced detector is shown. The peak at 815kHz is about 10dB larger than for the properly balanced detector, and around this peak a range of extra peaks has appeared. They are spaced of about 70kHz and are a clear indication that the detector is no longer shotnoise limited. This is excess noise originating in the laser, and has not been properly balanced out in the detector. The majority of this excess noise spectrum was traced back to the cavity dumper.

4.5.4 Measuring a quadrature

In Sec. 2.4.2 it was derived how the difference current in a homodyne detector is directly proportional to the measured quadrature-value of the probed quantum state. In reality the picture is slightly more complicated than that. First of all the difference current has to be a function of time in order for us to describe the pulsed nature of the optical signal [142]

$$i_{-}(t) \quad \propto \quad \alpha(t)\hat{q}_{\theta}(t), \qquad \hat{q}_{\theta}(t) \;=\; \hat{a}(t)e^{i\theta} + \hat{a}^{\dagger}(t)e^{-i\theta}, \tag{4.32}$$

where the explicit time-dependence is not included in the annihilation operator $\hat{a}(t)$. As described in Sec. 4.5.3 any detector will have a finite bandwidth, which in time-domain can be described a response function, $r(t)$. In Sec. 4.5.3 we saw that a signal is present even in the absence of any optical signal. This electronic noise will also contribute to the difference current, thus a more realistic description of the situation is given by

$$i(t) \quad = \quad i_e(t) + A\int_{-\infty}^{\infty} \alpha(t')\hat{q}(t')r(t-t')dt', \tag{4.33}$$

where the $-$ has been omitted from the difference currents for simplicity, $i_e(t)$ is the electronic noise difference and A is a proportionality constant encompassing the gain of the detector. If the detector had infinite bandwidth, the response function would be a delta function, $r(t) \;=\; \delta(t)$, and Eq. (4.33) would simplify to Eq. (4.32) apart from the electronic noise. Now, considering our case where the LO, $\alpha(t)$, is short pulses, which cannot be resolved by the electronics, we can treat the LO as a δ-function, $\alpha(t) \;=\; \alpha_p\delta(t)$, rearranging Eq. (4.33) to

$$i(t) \quad = \quad A\alpha_p\hat{q}r(t) + i_e(t). \tag{4.34}$$

Apart from the electronic noise the detector response to a short pulse will be given fully by the detector response function. This is also well known from standard differential theory on impulse response [143]. The response function is defined as the system solution found when the initial condition is a δ-function. In our system the response function is basically the pulse-shape shown in Fig. 4.11. Now in order to find the measured quadrature value, various solutions can be employed. The typical solution is integration of the difference current over some interval with some weight

function $\psi(t)$,

$$\hat{Q}_{\text{meas}} = \int_{t_0}^{t_0+\Delta T} i(t)\psi(t)dt = A\alpha_p\hat{q}\int_{t_0}^{t_0+\Delta T}\psi(t)r(t) + \hat{Q}_e, \quad (4.35)$$

where the integration window starting point, t_0, and length, ΔT, are determined by an optimization procedure. Now, as we saw in Sec. 4.5.1, the bandwidth of the detector could be expected to be at least 2MHz. This means that we can expect cross-talk between pulses to be negligible when operating with a repetition rate of 815kHz. This is also confirmed by the right figure in Fig. 4.11. Here, it is seen that the signal from one pulse can be expected to return to zero before the next pulse arrives. In order to find the optimal integration limits and weighting function in Eq. (4.35), we measured a batch of 65000 LO pulses with only vacuum as the signal being probed. Then, while varying the integration starting point and integration window, we extracted the quadratures from the measurement using Eq. (4.35). During this process we chose to use the simple weight function treating each point equally, $\psi(t) = 1$. For each setting we evaluated the variances in order to find the settings that would optimize Eq. (4.29). The findings are plotted in Fig. 4.13 From these

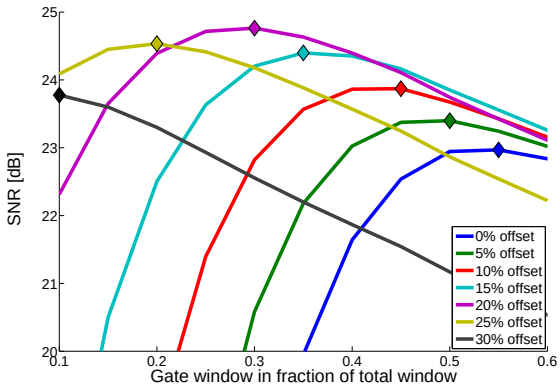

Fig. 4.13: Signal-to-noise ratio, $\langle\hat{q}_0^2\rangle/\langle\hat{q}_e^2\rangle$ as a function of size of integration window, $\Delta T/T$, for various settings of the integration starting point, t_0/T where T is the pulse separation.

results we found that the SNR could be optimized to a value of almost 25 dB by choosing the integration window according to $\Delta T/T = 0.3$ and $t_0/T = 0.2$. According to Eq. (4.29) this corresponds to a detection efficiency of more than $\eta_e > 99.5\%$. We can also see from Fig. 4.13 that the SNR is reasonably flat around the optimal setting of the integration, never dropping below 23 dB. No investigation was done into how an alternate weight function could improve the SNR even further. Looking strictly at the SNR and correspondingly the electronic detection efficiency,

this choice is justified. The room for improvement is so small that other sources of imperfections will vastly drown any improvement achieved by this. Now, having deduced how to extract the information about the measured quadrature, we can start measuring quadrature distributions for various quantum states. We start by measuring the distributions of the cases also used in the spectra in Fig. 4.12. Both spectra were measured for a vacuum state input in the signal, so we expect to see a Gaussian distribution of the quadratures, Eq. (2.25). However, in one of the cases the detector was not properly balanced, which can potentially influence the result. The

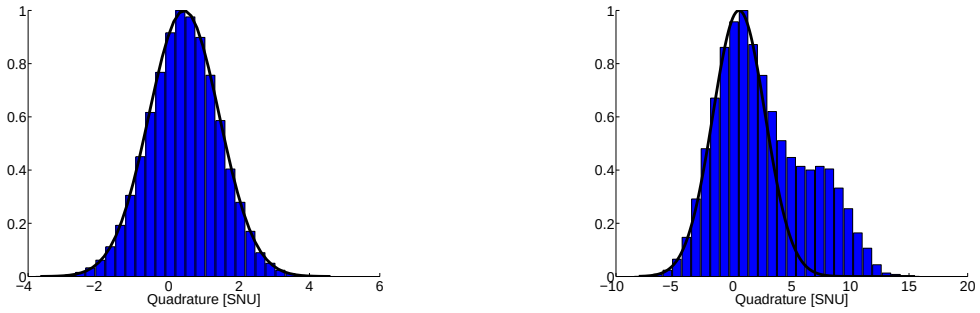

Fig. 4.14: Histograms for a measured vacuum state on a properly balanced (left) and an unbalanced (right) detector. The black curve is the Gaussian distribution with variance found from a properly balanced detector.

resulting histograms are seen in Fig. 4.14. On the left a nice Gaussian bell-shaped histogram is shown, as expected from a vacuum state. On the right, however, we can see the effect of the excess noise also found in the spectrum in Fig. 4.12. The outcome is a displacement of the Gaussian distribution and the emergence of a second, smaller lump. This distribution is clearly not Gaussian and as such completely useless, and much effort has been put into removing these effects. The Gaussian distribution on the left is not a confirmation that the detector works as expected. In order to test this, we must check the linearity of the vacuum noise with LO power, Sec. 4.5.5.

4.5.5 Shotnoise linearity

The final test to check if the detector configuration is working properly is to confirm that the detector is operating in accordance with Eq. (2.74). That is, does the measured variance of a vacuum state increase linearly with LO power, $|\alpha|^2$? In order to test this, we measured the vacuum variance and the SNR for the detector as a function of LO power. The result is shown in Fig. 4.15. On the left in Fig. 4.15 it is clearly seen that the variance increases linearly with LO power, for LO powers up to more than 100 million photons per pulse, corresponding to more than

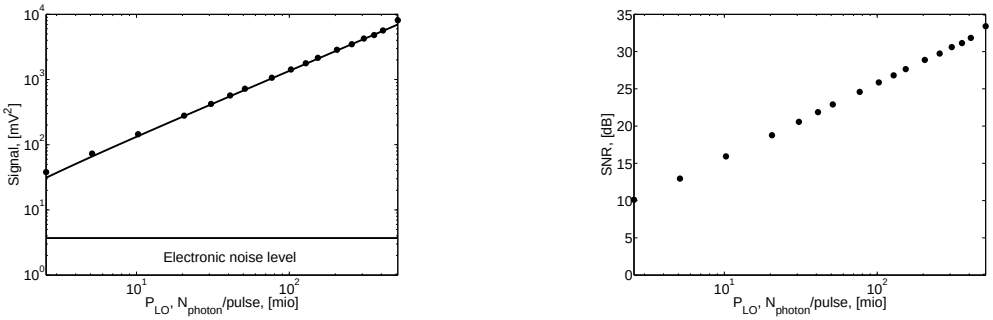

Fig. 4.15: Vacuum noise linearity (left) and SNR (right) of the homodyne detector configuration as function of LO power. The LO power is measured in photons per pulse, with 10 million photons per pulse corresponding roughly to 2μW.

20μW LO power. The SNR can reach almost 30dB within the same range of LO powers, and reaching 25dB well within the range where the detector is linear. From this we concluded, that the developed detector could be used in our experimental preparation of coherent state superpositions.

4.5.6 Implementing a homodyne detector using polarization

The way to implement a homodyne detection scheme is typically as depicted in Fig. 2.6, where the quantum state and the strong LO interfere at a 50/50 beam splitter and the two outputs are detected using photodiodes. However, an alternative which is sometimes used, is to implement it using the polarization degree of freedom. This is similar to a Stokes measurement. We chose to implement our homodyne detection schemes using this system. In such a system the quantum state and the LO are first spatially overlapped on a polarizing beam splitter (PBS). The situation is illustrated in Fig. 4.1 at PBS1/PBS2. The quantum state with vertical polarization enters through one port, while the LO with horizontal polarization enters through the second port. When leaving the PBS, the two will be overlapped, but in different polarizations, meaning they cannot interfere. By rotating the polarization by 45° using a half-wave plate the two fields can be made to interfere on a PBS oriented to split into horizontal and vertical polarizations.

4.6 Data acquisition

The process of measuring a quadrature was described in Sec. 4.5. The amplified difference current would be sampled with a sampling rate of 100 MS/s. The time-

trace would then be transfered to a computer, where an integration over individual pulses was carried out to extract the quadrature. This procedure was the same, regardless of the quantum state to be measured. We mainly measured two quantum states in the system. We measured a squeezed vacuum state and a photon subtracted squeezed state. There were only small differences in the way data was acquired in the two cases, but we will discuss it briefly here.

4.6.1 The squeezed state

Since squeezing is a deterministic process there is no need for heralding or post-selection when measuring it. Thus, when squeezing is being prepared, we can measure all pulses and keep all measurements. This was practically done by measuring continuously with a sampling rate of 100MS/s until the oscilloscope memory was filled up. When measuring squeezing, we needed two signals; the homodyne difference current and the cavity dumper signal for processing. When measuring two signals in continuous mode, the oscilloscope was capable of acquiring 8 MS on both signals before readout was needed. This would result in a measurement time of 80 ms. This corresponds to measuring approximately 65.500 squeezed pulses. Now, we did not implement any phase locking or active stabilization, so instead we decided to continuously scan the LO phase during such a measurement. The scan speed was set in such a way that during the 80ms we would scan approximately 2π, in order to calibrate according to a fitting function after the measurement.

4.6.2 Photon subtracted squeezed state

The detection rate of the APD during experiments could be varied between $\approx$ 250 s^{-1} for a pump power of 0.5 mW and could reach as much as 4500 s^{-1} for a pump power of 8.0 mW. This corresponds to probabilities ranging from $3 \cdot 10^{-4}$ to 0.006. Measuring the quadratures of the photon subtracted states could be done in two ways;

1) One could choose to measure squeezing as described previously and add the detection of a third signal from the APD. Then, during the data processing, the quadrature measured in correlation with an APD click is kept for further investigation. Looking at the statistics, we found, however, that this procedure was not efficient. Given the subtraction probabilities, the total number of detection events during a squeezing measurement would be of the order of 20 to

350. In order to acquire enough measurements to have reliable statistics, the number of measurement runs would be unproportionally high.

2) The alternative we decided on was to use a segmented measurement setting. By using the previously described electronics, we correlated the APD signal with the cavity dumper. By only sampling the homodyne difference current when an APD click was correlated with the cavity dumper, all the unsuccessful detection events could be rejected. By doing this, a set of 4000 quadratures could be acquired roughly in the same time it would take to acquire 1-2 full squeezing measurements. Here, the 4000 quadratures is the maximum number of segments the oscilloscope was capable to store before readout. In total this procedure enabled a speedup of a factor of 7 to 100.

4.7 Testing the system for squeezing

We tested the system for squeezing before venturing into any photon subtraction experiments. We measured the squeezing for a series of pump powers ranging from 0.5 mW to 8 mW, corresponding to peak powers of about 0.2 kW to 1.4 kW. The result is shown in Fig. 4.16. The same measurement is shown both on the left, in the

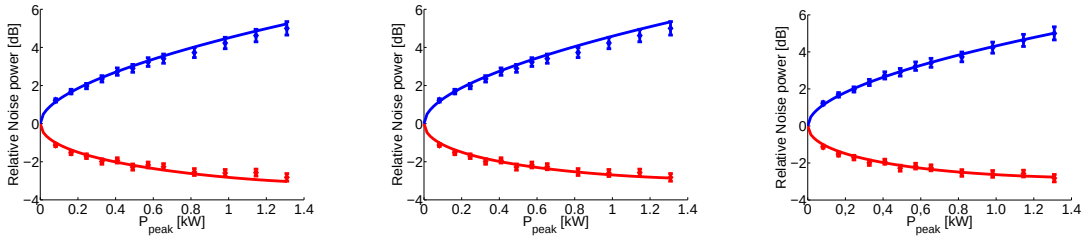

Fig. 4.16: Measured squeezing for a series of pump powers ranging from 0.2 kW to 1.4 kW peak power. The same measurement is shown both on the left, in the middle, and on the right. The three graphs are for three different schemes of fitting model. On the left, pure squeezing is assumed and the detection efficiency is the fitting parameter, in the middle the detection efficiency is fixed at $\eta = 0.77 \times 0.92 = 0.71$ and the purity is the fitting parameter, and on the right the detection efficiency is fixed at $\eta = 0.92$ and the purity is the fitting parameter. See text for further details.

middle and on the right. On the left the measured squeezing is fitted to a model, where pure squeezing is assumed and the detection efficiency is used to fit the model to the data. In the middle the detection efficiency is fixed at the experimentally calibrated value of $0.77 \times 0.92 = 0.71$. Here, the extra 0.92 factor arises from the fact that the 0.77 are measured without taking into account the tap-off mirror. The fitting is then done by assuming impure squeezing. On the right, perfect detection

is assumed, $\eta = 0.92$, and purity is again used as the fitting parameter. The fitting parameters for the three models are

$$\begin{aligned} 1) \quad & r_1 = 0.27\sqrt{P_p}, \quad r_2 = 0 \quad \eta = 0.65, \\ 2) \quad & r_1 = 0.25\sqrt{P_p}, \quad r_2 = 0.17\sqrt{P_p} \quad \eta = 0.71, \\ 3) \quad & r_1 = 0.19\sqrt{P_p}, \quad r_2 = 0.23\sqrt{P_p} \quad \eta = 0.92, \end{aligned}$$

where P_p is the average power. From this we can see that our detection efficiency for our squeezed state is at least 65% corresponding to a predicted detection efficieny of our photon subtracted states of 71%. Given that we pump our down conversion crystal with a plane wave pump, it is reasonable to expect the generated squeezing to be of reasonably high purity. And with a measured and inferred detection efficiency of 71% for the squeezed state the actual setting in the experiment is most likely somewhere between 1) and 2).

4.7.1 Predictions for photon subtraction

Based on the fitting curves for the squeezing and the model derived in Ch. 3.2, we can make some simple predictions on the performance of a photon subtraction experiment. These predictions can be considered as a most optimistic case for the photon subtraction. The predictions as a function of input squeezing and modal purity are shown in Fig. 4.17. From these results we can see the parameter space where we can expect to see positive results in terms of the fidelity and the negativity at the origin, given the performance of our squeezer and homodyne detectors. We can see that the potential for observing the non-classical behaviour greatly increases when going from low detection efficiency with pure squeezing to impure squeezing with high detection efficiency. Thus a low detection efficiency has a much larger impact on the results than a slight decrease in the quality of the squeezing. From these results we can also see that the modal purity must not fall below 0.8 if we are to be able to observe fidelities above 0.5 and negativities in the Wigner distribution.

Summary

In this chapter we presented the experimental techniques developed during the course of this project. The pulsed laser was discussed, including the problems it posed to the experimental work. Together with the laser the implementation of the SHG system was presented and investigated.

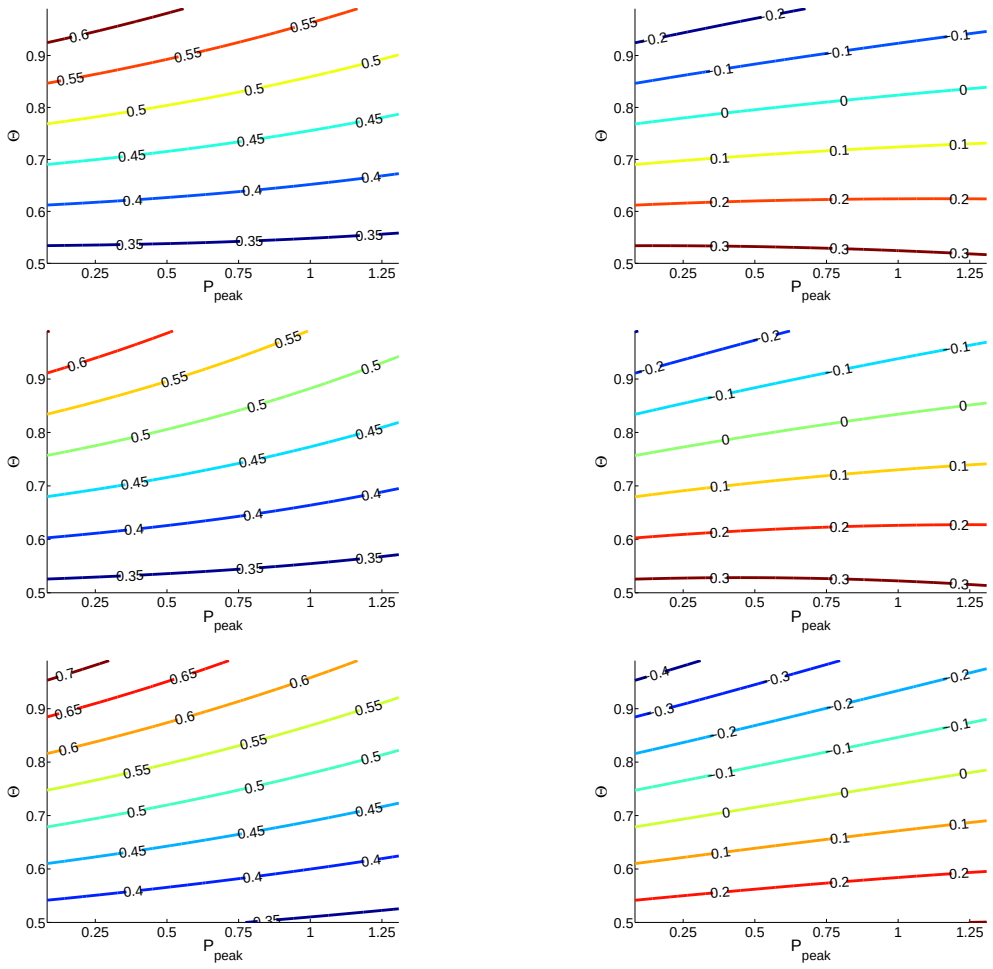

Fig. 4.17: Upper results are for the pure squeezing with $\eta = 0.65/0.92 = 0.71$, the middle results for impure squeezing with $\eta = 0.71/0.92 = 0.77$ and the lower results for impure squeezing with $\eta = 1.00$. On the left, fidelities with the most optimal CSS and on the right predictions for $\pi W(0,0)$.

After this, the tools for the actual state preparation were presented. First, the SPDC system was presented and investigated. The amplification/de-amplification was investigated and compared to theoretical predictions. Here, some discrepancies were discovered. The model did not fit to with experimentally obtained values using the measured values for the measured input parameters. The difference could, however, be eliminated by assuming tighter focusing of the pump. Also, the system for subtraction of photons was presented. Here, the frequency filter and our consideration regarding the spectral purity were discussed. The conclusion was that under certain circumstances, good spectral quality can be obtained.
Finally, the system for characterizing the prepared quantum states was presented.

The developed detector for time-domain balanced homodyne detection was investigated in detail. The detector itself as well as the post processing of the homodyne signal were tested and good linearity and signal-to-noise ratio were achieved. Finally the system was tested by measuring a squeezed state. From this squeezed state, predictions were made using the model from Ch. 3.

Chapter 5

Photon subtracted squeezed states

Having built and investigated the different parts of the setup needed for subtracting photons from squeezed vacuum we carried out a series photon subtractions for different pump powers for the squeezed state. We took a measurement series for the pump powers 1, 2, 4, 6 and 8 mW's. In the following we will present these results and discuss the quality of the reconstructed states. We will start with a discussion of how to infer information about the phase from the time-traces. Then we will present the reconstructed states. Finally we will present an optimized way of inferring the phase motivated by the somewhat non-elliptical states resulting from the initial phase inference.

5.1 Setting the phase

In order to carry out any reconstructions we need to specify a phase for the different measurement projectors, Eq. (2.80). The phase in question is the relative phase between the prepared quantum state and the local oscillator. This phase could be set in a number of different ways. We could have tried to lock all phases in the experimental setup and always measured at a specific chosen local oscillator phase. Another option is to carry out a calibrated scan of the phase during a measurement. A third solution is to try and infer it from the measured quadratures by applying some assumption on the prepared state.
As we did not employ any means of locking the phase or perform a calibrated scan, we had to try and infer it from the measured quadratures. With good justification we can assume that the rotational noise dependence of our states follow the relation

$$\mathrm{Var}(\theta) \quad = \quad \mathrm{Var}_{max}\cos^2\theta + \mathrm{Var}_{min}\sin^2\theta$$

$$= \frac{\mathrm{Var}_{max} - \mathrm{Var}_{min}}{2} \cos 2\theta + \frac{\mathrm{Var}_{max} + \mathrm{Var}_{min}}{2}. \quad (5.1)$$

This phase dependence of the noise is the same as one would find for a squeezed state. Since the starting point for our subtraction protocol is the squeezed state and the subtraction is completely phase insensitive, it would seem justified to assume that the phase dependence of the noise in our prepared states is the same as for squeezing. Now, the relation in Eq. (5.1) depends on the variances of the measured quadratures, so we need to define variances for our quadrature data. In order to do this we need to somehow bin our data. Looking at the time traces in Fig. 5.1 we can see how the phase is roughly scanned by 2π during the course of a single trace. By

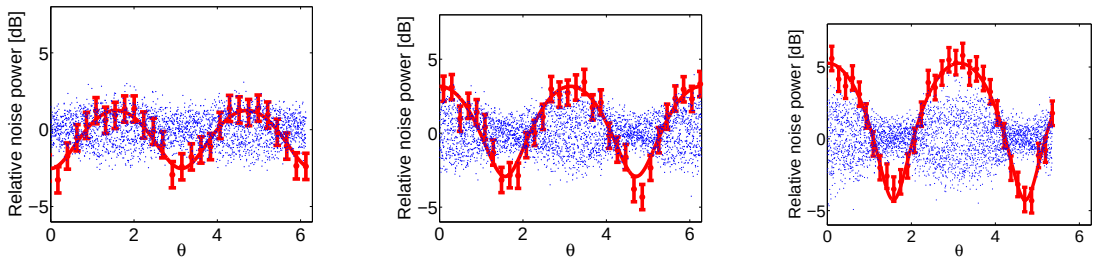

Fig. 5.1: Time traces with bin-variance and fitted phase dependence. On the left a trace for a pump power of 1 mW, in the middle for 4 mW and on the right for 8 mW. Each trace consist of 4000 quadratures.

binning the data in bins of 100 quadratures we can fit the phase to the dependence in Eq. (5.1). The choice of bin-size, will inevitably influence the amplitude of the phase fitting, but will have less influence on the argument, θ. The fitting is done by assuming that the phase space angle depends on the quadrature/bin number, k, according to, $\theta(k) = \omega_2 k^2 + \omega_1 k + \varphi$. It turned out that the second order term was not needed to obtain nice fits, so the fits shown in Fig. 5.1 are all done without this term.

5.2 Reconstruction

After fitting the variance to the dependence in Eq. (5.1) we reconstructed the prepared states for the different pump powers. The convergence of the maximum likelihood algorithm, Sec. 2.4, was also investigated. We monitored the convergence by taking the absolute change between the current reconstructed state and the previous

$$\sum_{n,m} \left| \left|\hat{\rho}^{(i)}\right| - \left|\hat{\rho}^{(i-1)}\right| \right|. \quad (5.2)$$

The convergence as a function of iteration number can be seen in Fig. 5.2 From these

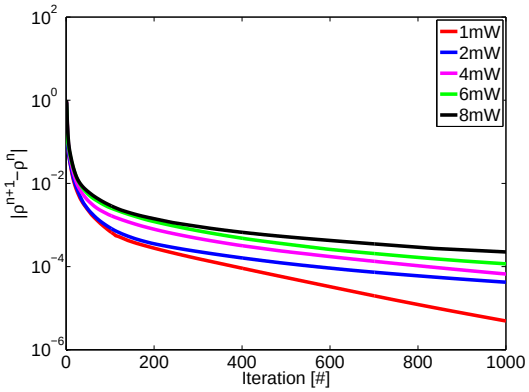

Fig. 5.2: Convergence given by Eq. (5.2).

results we see that, as the pump power increases and the states should become more populated, the convergence of the MaxLik algorithm becomes slower. The starting point for all reconstructions was the completely mixed state

$$\hat{\rho}^{(0)} = \sum_{n=0}^{N_{max}} \frac{1}{N_{max}+1} |n\rangle \langle n| . \tag{5.3}$$

We did the measurement for 1, 2, 4, 6 and 8 mW pump powers. The results will be discussed in further details in the following sections. All reconstructions were done with a Hilbert space dimension of $N_{max} = 13$. Also correction for a finite detection efficiency of 0.77 ± 0.02 was included. This value includes propagation efficiency, 0.93 ± 0.01, interference with the LO 0.95 ± 0.01 and efficiency of the photodiodes 0.93 ± 0.01.

5.2.1 1 mW

For the pump power of 1 mW the Wigner distribution for the reconstructed state is shown in Fig. 5.3. The reconstruction is based on a set of 52.000 successful subtraction events distributed across 13 traces of 4000 quadratures. Initially the phase was fitted within each trace using the previously described method. After this, all traces were concatenated and one reconstruction was carried out using the full data-set. The resulting state is shown in Fig. 5.3. From the result we see that the squeezed state has clearly been de-Gaussified. A clear dip is visible around the origin of the Wigner distribution, however, this dip unfortunately do not go deep enough to attain negative values. The value is found to be 0.031 ± 0.009. By decomposing the

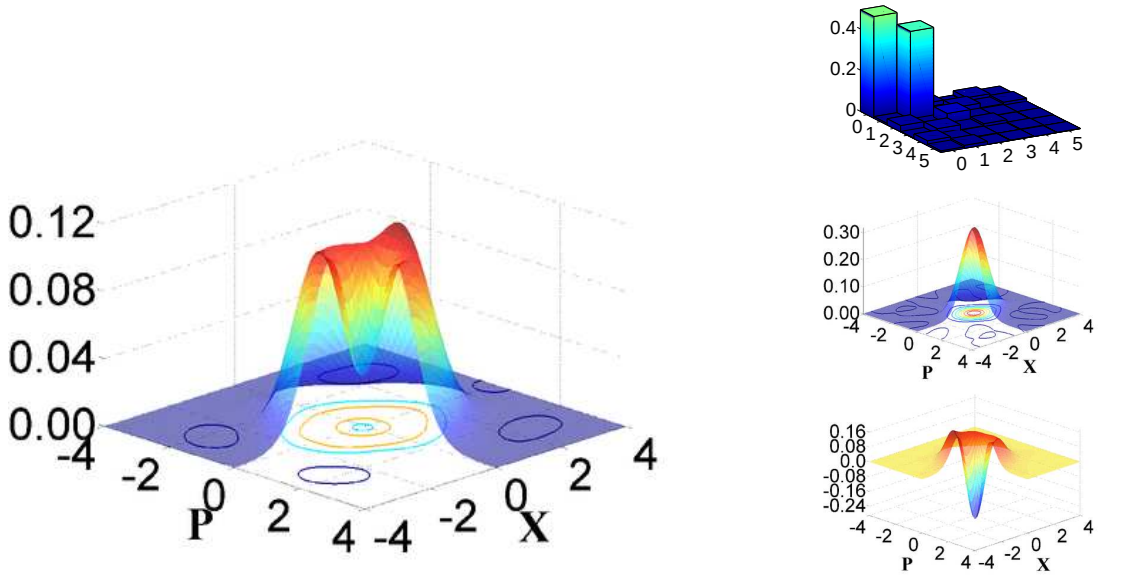

Fig. 5.3: Wigner distribution for the reconstructed state for 1 mW pump power (left). On the right the density matrix up to $n = 5$ and the two most dominant eigenstates.

state into its eigenstates we can get an idea of what states make up the result. The Wigner distributions for the two most dominant eigenstates are also shown in Fig. 5.3. The most dominant, $\rho_0 = 0.497$, looks almost like a vacuum state, and indeed the fidelity between this state and vacuum is above 95%. The second eigenstate with $\rho_0 = 0.437$ looks like a single photon with a small degree of squeezing. And the fidelity between this state and the single photon was also found to be more than 90%. These two eigenstates comprise more than 90% of the state. The rest is contamination from mainly a small fraction of something resembling a two-photon state.

5.2.2 2 mW

For the pump power of 2 mW the Wigner distribution for the reconstructed state is shown in Fig. 5.4. The reconstruction is based on a set of 76.000 successful subtraction events. Again the phase is initially fitted on each trace of 4000 quadratures individually before all traces are concatenated. Looking at these results the outcome does not seem to improve compared to the case of 1mW pump power. The dip around the origin is still present, but is now only dropping to a value of 0.038 ± 0.009. The two dominant eigenstates are similar to the ones for 1 mW pump power with only slightly shifted weights, $\rho_0 = 0.473$ and $\rho_1 = 0.407$. They are both lower than

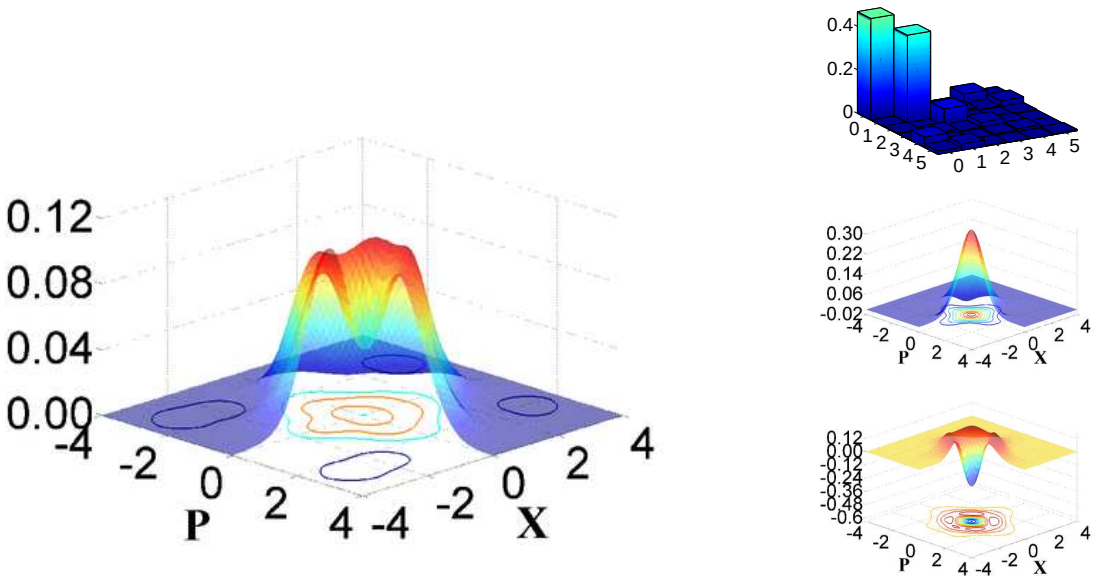

Fig. 5.4: Wigner distribution for the reconstructed state for 2 mW pump power (left). On the right the density matrix up to $n = 5$ and the two most dominant eigenstates.

before, thus a higher amount of two-photon contribution is present in the state.

5.2.3 4 mW

For the pump power of 4 mW the Wigner distribution for the reconstructed state is shown in Fig. 5.5. The reconstruction is based on a set of 36.000 successful subtraction events. The phase fitting and reconstruction is done in the same manner as for 1 mW and 2 mW pump powers. Here the result is improving compared to the previous cases. The dip has now fallen to 0.010 ± 0.010. This is very close to the definite non-classical boundary. Also looking at the Wigner distribution we see something resembling two lumps. These lumps could resemble those appearing in the states in Eq. (3.6). In this experimental state we, however, do not have a superposition of these two states. Instead we have something which would be more of a mixture of the two. This could also seem to confirmed by the eigenstates, which are now a lump at either $-x_0$ or x_0. These two eigenstates have practically equal weight, $\rho_{\pm} \approx 0.39$ and are found to be closely resembling the states $|0\rangle \pm |1\rangle$, which is also comparable to the result in Eq. (3.6).

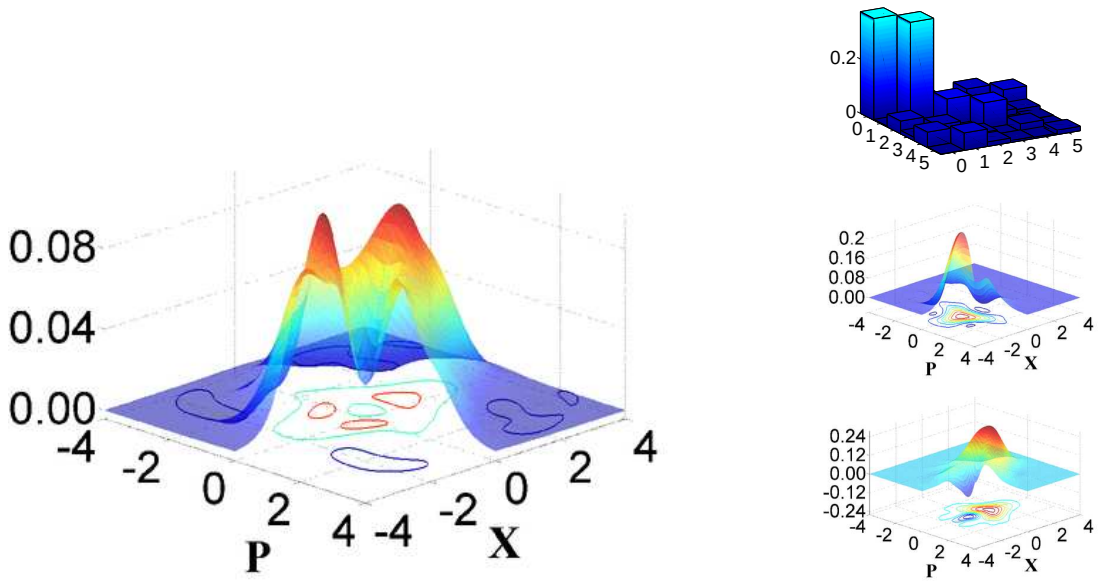

Fig. 5.5: Wigner distribution for the reconstructed state for 4 mW pump power (left). On the right the density matrix up to $n = 5$ and the two most dominant eigenstates.

5.2.4 6 mW

For the pump power of 6 mW the Wigner distribution for the reconstructed state is shown in Fig. 5.6. The reconstruction is based on a set of 64.000 successful subtraction events and the phase is again inferred according to Eq. (5.1). Here we see further improvement of the state quality. The value at the origin has dropped further to $W(0,0) = -0.010 \pm 0.010$. This value is indicative of the clear non-classical nature of the prepared state. Also looking at the Wigner distribution, it does not present the expected elliptical shape. This suggest that the phase fitting algorithm is not perfect. This also shows up in the eigenstates which look somewhat special. The most dominant one has some resemblance to vacuum, although with some slightly weird structure. The other eigenstate is more reminiscent of a squeezed single-photon, with only small ripples.

5.2.5 8 mW

For the pump power of 8 mW the Wigner distribution for the reconstructed state is shown in Fig. 5.7. The reconstruction is based on a set of 80.000 successful subtraction events again using Eq. (5.1). Now the dip at the origin is clearly below the classical boundary, $W(0,0) = -0.03 \pm 0.01$. The reconstructed state is however still looking somewhat odd. Instead of a nice ellipse, it has a series of peaks. The

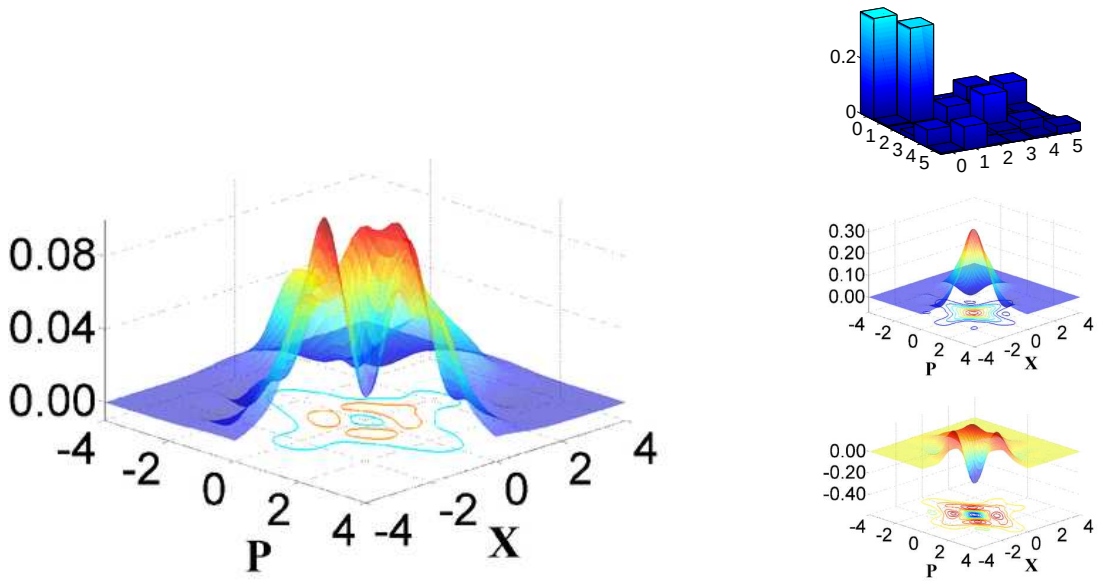

Fig. 5.6: Wigner distribution for the reconstructed state for 6 mW pump power (left). On the right the density matrix up to $n = 5$ and the two most dominant eigenstates.

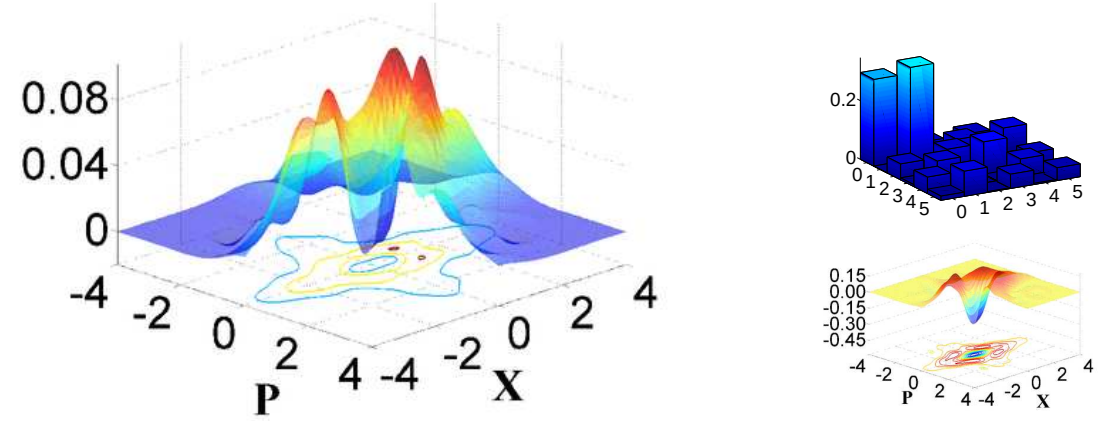

Fig. 5.7: Wigner distribution for the reconstructed state for 8 mW pump power (left). On the right the density matrix up to $n = 5$ and the most dominant eigenstate.

dominant eigenstate for this reconstruction is also shown in Fig. 5.7. In this case it is highly dominant compared to the other contributions, $\rho^{(1)} \approx 0.45$. All other contributions are below 0.35. The eigenstate looks like a clearly squeezed single-photon. Also looking at the density matrix we see that the most dominant contribution is the single photon component.

5.3 Optimizing the phase fitting

Observing the phase space behaviour of the reconstructed states for the 6 and 8 mW pump powers, Figs. 5.6 and 5.7, we could see that the states did not show the expected elliptical shape of a photon subtracted squeezed state. From the time-traces in Fig. 5.1 we could see that some of the variance bins were lying somewhat away from the fitting curve which was a recurring thing in many of the time-traces. An effect that seemed be more pronounced for the higher pump powers and also seemed to be correlated with the non-elliptical shapes of the Wigner distributions. In order to see if we could get more elliptical states in phase space we allowed for some optimization. We allowed the phase of individual bins to be altered slightly within a small interval around the fitted phase in attempt to reconstruct more elliptical states. The size of this interval, $\delta\varphi$, was chosen to be much smaller than the phase-scan distance in the bin, $\Delta\varphi$. This optimization was applied to the reconstructions for 6 and 8 mW, since it would appear that the prepared states at these pump powers were of the best quality.

5.3.1 6mW

We applied this optimization procedure to the state prepared for the 6 mW case. The resulting Wigner distribution, density matrix and most dominant eigenstate is

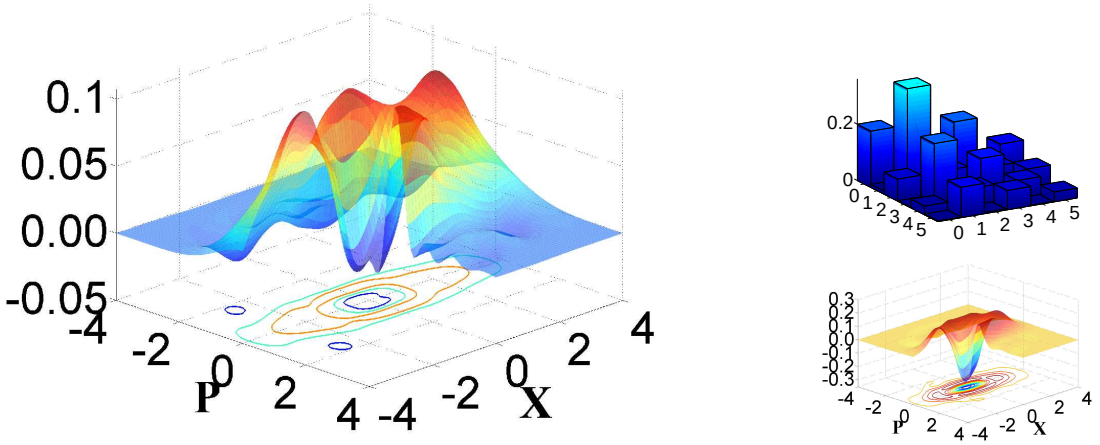

Fig. 5.8: Wigner distribution for the reconstructed state for 6 mW pump power with optimized phase fitting (left). On the right the density matrix up to $n = 5$ and the most dominant eigenstate.

shown in Fig. 5.8. From the Wigner distribution it is seen that the state is now much more elliptical in phase space. It would, however, also appear that the quality of the

state has improved. The value of the Wigner distribution at the origin can now be found to be $W(0,0) = -0.02 \pm 0.01$, again after loss-correction. Finding the fidelity with the most optimal coherent state superposition we find $F = 0.56 \pm 0.02$ for a CSS amplitude of $\alpha = 1.30$. Considering the most dominant eigenstate, we can see it is now the squeezed single photon. And it is found to have a weight of more than 50%.

5.3.2 8mW

Finally we applied this optimization procedure to the state prepared for the 8 mW case. The resulting Wigner distribution, density matrix and most dominant eigen-

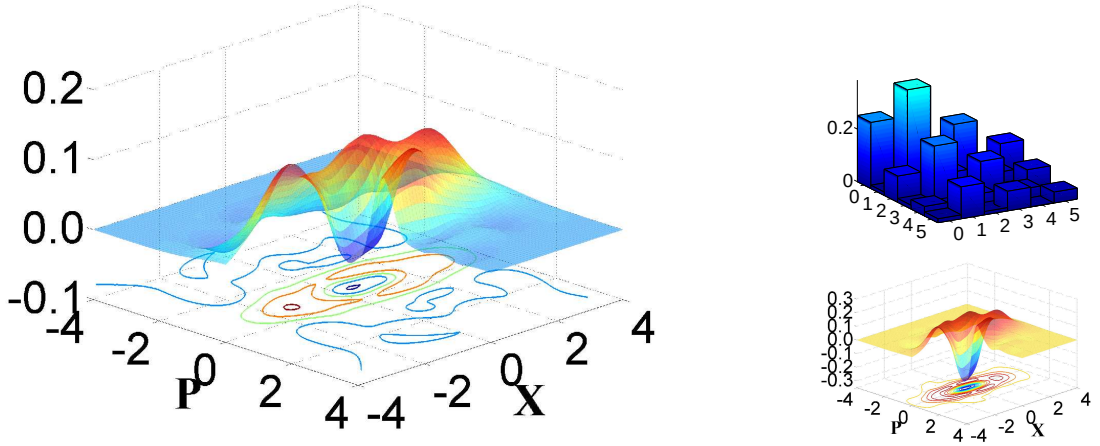

Fig. 5.9: Wigner distribution for the reconstructed state for 8 mW pump power with optimized phase fitting (left). On the right the density matrix up to $n = 5$ and the most dominant eigenstate.

state is shown in Fig. 5.9. This Wigner distribution is also seen to become more elliptical in phase space. And again it would also appear that the quality of the state is improving. The value of the Wigner distribution at the origin can for this state be found to be $W(0,0) = -0.05 \pm 0.01$ after loss-correction. Finding the fidelity with the most optimal coherent state superposition we find $F = 0.57 \pm 0.02$ for a CSS amplitude of $\alpha = 1.36$. Also for this case the most dominant eigenstate is the squeezed single photon, with a weight of more than 50%.

5.4 A comment on error estimation

Estimating the uncertainty of a reconstructed state can be difficult and is an area of much research [144]. The different parameters can often be difficult to estimate

with any reasonable accuracy. This lack of accuracy will result in uncertainties in the reconstructed states. But due to the limited capability to accurately determining parameters such as detection efficiency, predicting the precise influence on the prepared states can be difficult. However, one source of errors which can be readily investigated, is the uncertainty resulting from limited sampling statistics. This can be done by randomly generating data and reconstructing a number of sample states. The random data is generated from the marginal distribution of the state reconstructed from the experimental data using quantum Monte Carlo simulation. From this artificial data a new state can then be reconstructed. By doing this a number of times and doing statistics on the reconstructed states, an estimate of the uncertainty originating from limiting sampling statistics can be obtained.
In order to ensure that the statistical significance in the maximum likelihood algorithm is correctly estimated the amount of random data must be equivalent to the amount of measured data. Also the random data should be prepared and treated in the same way as the measured data. Thus, the data should be generated at the phase space angles found from the phase fitting, and at each phase a set of data equivalent to the measured should be prepared. We implemented such a Monte Carlo simulation and generated 100 random states, and the errors given previously is based on the standard-deviation found from these 100 states.

Summary

In this chapter we verified that the experimental setup prepared in Ch. 4 could be used to prepare and characterize non-Gaussian states by photon subtraction from squeezed vacuum. We saw how the state quality improved as the pump power and thus the squeezing strength was increased. This is in contrast to the predictions made both in Ch. 3 and Ch. 4. From the results in Figs. 3.5, 3.6, 3.8 and 4.17 we expected the quality to be best for lower pump powers. The reason for this behavior is not yet fully understood.
We also saw how the results for both 6 and 8 mW suggest that a more robust way of fitting the phase can be found. Looking at the Wigner distributions we saw clear indications that the phase was not fitted perfectly. Spurred by these results we were motivated to develop a more robust procedure to infer the phase.
Such procedure was found and applied to the measurements for 6 and 8 mW pump powers and a clear improvement in the ellipiticity of the state was found. This improvement also gave some improvement in the general quality of the state. This optimized phase fitting procedure will be applied in the Hadamard gate experiment,

Ch. 6.

Chapter 6

Hadamard gate for coherent state superpositions

The increased interest in coherent state superpositions over the last decade has partly been spurred by the advent of a universal set of quantum gates deviced for this type of states [43, 45, 102, 145]. These proposals all fall into the category of measurement-based linear optical quantum processors [146]. In this category the most famous ones are the cluster state quantum processor [147, 148], and the linear quantum computer approach known as the KLM-scheme [149]. In the former, universal operation is achieved through a series of measurements on a large prepared entangled cluster state. Using this technique, several quantum operations have been demonstrated in recent years [150, 151, 29]. The KLM-scheme is based on single-photon resources which interfere in a linear optical network and are subsequently measured to enforce the desired operation. Using this approach, the C-NOT gate has been demonstrated [13].

The proposal by Ralph *et al.* [43] is a beautiful solution to the challenge of devising a set of gates for obtaining universal operation. The proposed gates are based on linear operations such as beam splitters and displacements combined with projective measurements which can be realized using photon-number resolving detectors. The coherent state superpositions are prepared off-line and are available as resource states. The gates work by displacing the states out of the computational basis by a small amount, $\alpha \rightarrow \alpha + i\theta$ where $\alpha \gg \theta$, and then projecting back onto the computational basis. The gates can be made near-deterministic, if instead of making the full transformation in one step, it is broken down into a finite number of steps, $N \gg 1$, and carrying out the operation N times. Another option is to implement the gates using teleportation, in which case the gates can be made deterministic.

However, this scheme suffers from strong requirements on the experimental parame-

ters. It relies on projective measurements which are difficult to implement in practice and the demands on the resource states are strong. For this reason experimental investigations into these schemes are not readily realistic. An alternative solution has been put forward by Marek and Fiurášek, which should be realisable using current technology [152]. The proposal is based on the same idea of displacing the states out of the computational basis and projecting back into the basis. The difference is mainly in the type of projective measurements needed for the realization of the gate operation. Here the projective measurements can be realized using photon subtraction and homodyne detection. Thus making the physical realization of these gates feasible with current technology. The simpler realization comes, however, with a cost. These gates can only be realized in a probabilistic fashion as opposed to the proposal by Ralph *et al.*.
We did an experimental implementation of the Hadamard gate proposed by Marek and Fiurášek. The results in this chapter have been presented at CLEO©Europe 2011 and published in Physical Review A, Rapid Communications [153].

6.1 The Hadamard transform

The Hadamard transform is the linear transformation that takes a set of basis states and transforms them into the rotated basis,

$$\hat{\mathcal{H}}(x\left|0\right\rangle + y\left|1\right\rangle) \quad = \quad x\frac{\left|1\right\rangle + \left|0\right\rangle}{\sqrt{2}} + y\frac{\left|1\right\rangle - \left|0\right\rangle}{\sqrt{2}}. \tag{6.1}$$

Using this, it is easily verified that, besides linearity, the Hadamard transform satisfies the relation

$$\hat{\mathcal{H}}\hat{\mathcal{H}} \;=\; \mathbb{1}. \tag{6.2}$$

The simplest example of a Hadamard transform for optical systems is a half-wave plate operating in the polarization basis. In this basis the information can be encoded like $\left|0\right\rangle, \left|1\right\rangle \;=\; \left|H\right\rangle, \left|V\right\rangle$. If the wave-plate is rotated by 22.5°, we have the transformation

$$\hat{\mathcal{H}}(x\left|H\right\rangle + y\left|V\right\rangle) \quad = \quad x\frac{\left|H\right\rangle + \left|V\right\rangle}{\sqrt{2}} + y\frac{\left|H\right\rangle - \left|V\right\rangle}{\sqrt{2}}. \tag{6.3}$$

From Eqs. (6.1) and (6.3) we can see that the Hadamard transform is well defined if it operates on an orthonormal binary basis, $\{\left|0\right\rangle, \left|1\right\rangle\}$. In that case the linearity and

the condition in Eq. (6.2) are well defined. However, this is not the case if the basis is no longer orthonormal. This is exactly the case for the coherent state superpositions. In this case the encoding basis, $|\pm\alpha\rangle$, is no longer orthonormal, thus the relation

$$\hat{\mathcal{H}}(x\,|\alpha\rangle + y\,|-\alpha\rangle) \quad = \quad x(|\alpha\rangle + |-\alpha\rangle) + y(|\alpha\rangle - |-\alpha\rangle) \tag{6.4}$$

without normalization is no longer well-defined. In this case we can choose any arbitrary normalization since $(\langle\alpha|+\langle-\alpha|)(|\alpha\rangle-|-\alpha\rangle) = 0$. However, two normalizations would appear to be more clever than others:
Normalization 1:

$$\hat{\mathcal{H}}(\cos(\theta)\,|\alpha\rangle + e^{i\varphi}\sin(\theta)\,|-\alpha\rangle) \quad = \quad \frac{\cos(\theta)(|\alpha\rangle + |-\alpha\rangle) + e^{i\varphi}\sin(\theta)(|\alpha\rangle - |-\alpha\rangle)}{\sqrt{2(1+\cos(2\theta)e^{-2\alpha^2})}}. \tag{6.5}$$

Normalization 2:

$$\hat{\mathcal{H}}(\cos(\theta)\,|\alpha\rangle + e^{i\varphi}\sin(\theta)\,|-\alpha\rangle) \quad = \quad \cos(\theta)\frac{|\alpha\rangle + |-\alpha\rangle}{\sqrt{N_+}} + e^{i\varphi}\sin(\theta)\frac{|\alpha\rangle - |-\alpha\rangle}{\sqrt{N_-}}. \tag{6.6}$$

Here the first choice of normalization satisfies Eq. (6.2) while the second satisfies linearity. These two normalizations are not identical and the average fidelity can be shown to go to $F = 0.5$ for $\alpha \to 0$ and to $F = 1$ for $\alpha \to \infty$. For $\alpha \gtrsim 1$ the average fidelity is, however, already exceeding $F > 0.99$, so the difference is quickly becoming negligible.

6.2 Practical implementation

In the proposal by Marek and Fiurášek [152] the gate operation is achieved through linear operations on the input, and a set of projective measurements on the input and a resource state. The realization requires two projective measurements, one of the discrete variable type, i.e. a photon subtraction, and one of the continuous variable type, i.e. a homodyne measurement. A schematic overview of the gate is shown in Fig. 6.1. The gate is successfully implemented by a displacement of the input state, $u\,|\alpha\rangle + v\,|-\alpha\rangle$, by α followed by a joint but biased subtraction, $r\hat{a}_1 + t\hat{a}_2$, of a photon from the input and the resource. Finally, the resource is projectively measured using a homodyne detector $\langle x|$. Assuming the resource is an even coherent

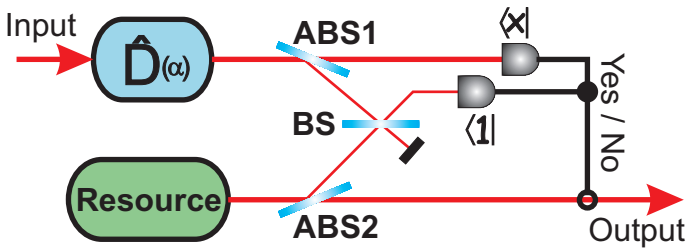

Fig. 6.1: Schematic overview of the Hadamard gate. The input CSS is displaced and afterwards a joint photon subtraction is carried out on the input and a resource, $|\alpha\rangle + |-\alpha\rangle$. The output is finally heralded on a successful quadrature measurement using homodyne detection.

state superposition $|\alpha\rangle + |-\alpha\rangle$, the output from this protocol can be shown to be

$$|\psi\rangle_{out,1} = \frac{1}{\sqrt{N_+}}\Big[u(|\alpha\rangle + |-\alpha\rangle) + Y_1(u + vZ)(|\alpha\rangle - |-\alpha\rangle)\Big], \tag{6.7}$$

with

$$Y_1 = \frac{t}{2r}, \quad Z = \frac{\langle x|\, 0\rangle}{\langle x|\, 2\alpha\rangle}. \tag{6.8}$$

If the conditions $Z \gg 1$ and $ZY_1 = 1$ are fulfilled, the output will match the normalization in Eq. 6.5, and thus a Hadamard transform has been implemented. Now, we can also redefine the Y_1-parameter according to

$$Y_2 = Y_1\sqrt{\frac{N_-}{N_+}}, \tag{6.9}$$

resulting in the output state

$$|\psi\rangle_{out,2} = u\frac{|\alpha\rangle + |-\alpha\rangle}{\sqrt{N_+}} + Y_2(u + vZ)\frac{|\alpha\rangle - |-\alpha\rangle}{\sqrt{N_-}}. \tag{6.10}$$

If the condition $ZY_2 \gg 1$ is now enforced, the normalization will match the one in Eq. (6.6). Now, the important thing being that the $Y_{1,2}$ and Z-parameters can be pre-set in the experiment based on the choice of normalization, enabling us to reach them both. Since this implementation of a Hadamard gate relies on heralding projective measurements it will by nature be probabilistic.

In Ch. 5 we saw how difficult it was to prepare the coherent state superpositions with good quality. So the resource needed for the Hadamard gate in this proposal is not easy to prepare. Instead, we decided to use another resource which is reminiscent of the even coherent state superposition. The squeezed vacuum state, Eq. (2.37) has

a large degree of overlap with the even CSS if $\alpha \lesssim 0.8$. Making this substitution the output will be given by

$$|\varphi\rangle_{out,2} = u\hat{S}(s)|0\rangle + Y_2(u+vZ)\hat{S}(s)|1\rangle, \tag{6.11}$$

where $s = |\zeta|$ is the absolute value of the complex squeezing parameter and Y_2 is now given by

$$Y_2 = -\frac{t\sinh(s)}{2r\alpha}. \tag{6.12}$$

where Y_2 has now been chosen to enforce the normalization in Eq. (6.6). The result in (6.12) is equivalent to the result in (6.10) since we can make the approximations

$$\hat{S}(s)|0\rangle \approx \frac{|\alpha\rangle + |-\alpha\rangle}{\sqrt{N_+}} \quad \vee \quad \hat{S}(s)|1\rangle \approx \frac{|\alpha\rangle - |-\alpha\rangle}{\sqrt{N_-}}. \tag{6.13}$$

By redefining the Y_2 parameter according to

$$Y_1 = Y_2\mathrm{sech}(s) = -\frac{t\tanh(s)}{2r\alpha}. \tag{6.14}$$

we will get another output given by

$$\begin{aligned}|\varphi\rangle_{out,1} = \mathrm{sech}(s)^{1/2}\Bigg[&u\sum_{n=0}^{\infty}\frac{\sqrt{(2n)!}}{n!}\left(-\frac{1}{2}\tanh(s)\right)^n|2n\rangle \\ &+Y_1(u+vZ)\sum_{n=0}^{\infty}\frac{\sqrt{(2n+1)!}}{n!}\left(-\frac{1}{2}\tanh(s)\right)^n|2n+1\rangle\Bigg],\end{aligned} \tag{6.15}$$

which has the same normalization as in Eq. (6.7). For this alternative resource the Z-parameter is the same as for the ideal resource. Using Eqs. (6.7)-(6.14), we can find the expected ideal average fidelity, the required squeezing and the appropriate choice of x-quadrature to use in $\langle x|$. The average fidelity is defined over the Bloch sphere according to the integral

$$F_{avg} = \frac{1}{4\pi}\int_{-\infty}^{\infty}\int_{-\infty}^{\infty}\langle\psi|_{ideal}|\psi\rangle_{out}\sin(\theta)d\varphi d\theta, \tag{6.16}$$

where $|\psi\rangle_{ideal}$ is found from Eqs. (6.5) and (6.6). The predicted average fidelity, the required squeezing and the optimal choice of x is plotted in Fig. 6.2 for a setting of the biasing of $|t|^2 = 0.25$. From the result, it is seen that for a size of the coherent

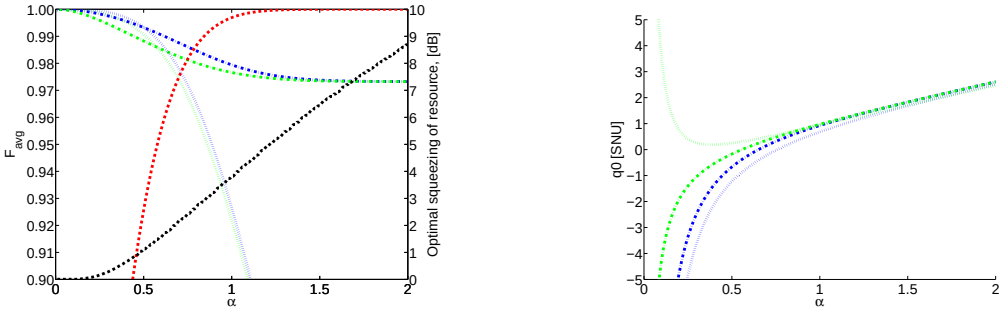

Fig. 6.2: Predicted ideal average fidelity F_{avg} (left) for ideal (dash-dot) and squeezed state (dotted) resource and for normalization according to Eq. (6.6) (blue) and according to Eq. (6.5) (green). The red dash-dot curve shows the average fidelity between the two normalizations and the black dash-dot curve shows the optimal squeezing. Everything is shown as a function of the the size of the coherent alphabet α. On the right, the optimal choice of heralding quadrature is shown, again for the ideal (dash-dot) and a squeezed resource (dotted) and for the two different normalizations (blue+green).

alphabet of $\alpha \lesssim 1.0$, the squeezed state can be regarded as a good substitute of the ideal resource, with an expected average fidelity of more than $F > 0.90$, with a squeezing degree of up to 4dB. This result is independent on the choice of normalization. In Sec. 4.7, in the description and characterization of our squeezer, it was shown that squeezing values of up to 2.5dB could be prepared and measured. This degree of squeezing matches the squeezing needed to approximate the gate operation for $\alpha \approx 0.75$, where the average fidelity to the ideal gate can be as high as $F \approx 0.97$. From this we concluded that an appropriate size of the coherent alphabet for our gate implementation would be $\alpha = 0.75$.

The practical implementation of the gate is very much similar to that of standard photon subtraction. We need to implement a joint biased photon subtraction from two states at the same time, and subsequently measure the two states with homodyne detectors, where one is measuring at a fixed phase and the other is scanned. The experimental setup is shown in Fig. 6.3. Most of the setup has already been described in detail in Ch. 4, so here we will only focus on the additions to the setup. First we need an input state to our gate. This input state is derived from the weak seed beam used to test the parametric amplification/de-amplification. This beam is attenuated to a level of $\beta = 1.6 \pm 0.2$, which corresponds roughly to 2α. In order to fully investigate the functionality of a quantum gate, it should be tested for an arbitrary superposition input. Since the preparation of an arbitrary coherent state superposition is a challenging task at best [154], we decided to only test the gate for the computational basis states $|\pm\alpha\rangle$. After the displacement of the input these states would be translated into $|0\rangle$, $|2\alpha\rangle$. This is easier to implement by blocking

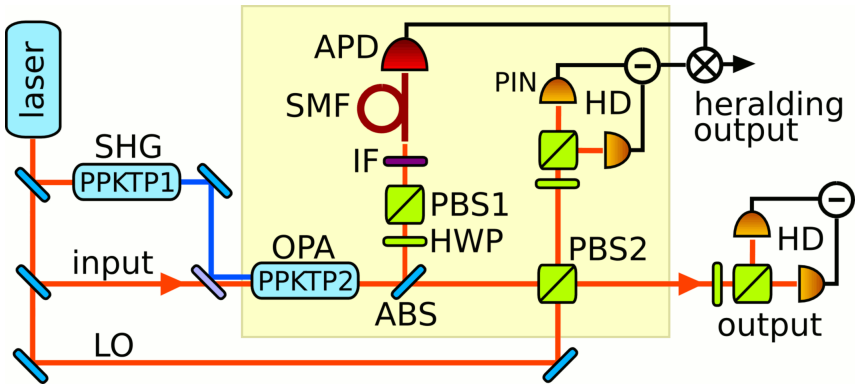

Fig. 6.3: Experimental setup for the Hadamard gate for coherent state qubits.

and unblocking the input state, and for this reason we could skip the displacement. The input coherent state is set to a horizontal polarization, meaning it will exhibit no parametric interaction with the pump in the down-conversion crystal. After the crystal the weakly reflecting mirror taps off the 7.8% of the squeezed state and approximately 1.5% of the input coherent state. The difference in reflection is due to the Fresnel reflection [137]. The biasing of the photon subtraction is achieved by a half-wave plate (HWP) and a polarizing beam splitter (PBS1) and is set to $|t|^2 = 0.25$ as is the case for the theoretical curves in Fig. 6.2. The rest of the subtraction arm, with the Fabry-Perot filter and the APD is the same as described in Ch. 4.

The subtracted states are split on another polarizing beam splitter (PBS2), so the input state with horizontal polarization goes to the homodyne detector for heralding, and the resource "leaves" the gate and is subject to full quantum state tomography on another homodyne detector. The heralding homodyne detector was set to measure the x-quadrature, corresponding to the direction of highest displacement of the input coherent state alphabet. This phase was fixed by manually scanning the LO piezo using a DC power supply to the phase where the amplitude of the measured coherent state was the greatest. The full phase scan of the output state for full state tomography was achieved by scanning the phase of the pump for the squeezing crystal.

6.3 Results and simulation

The first issue is setting the heralding quadrature of the heralding homodyne detector. Since we did not have the option of injecting an arbitrary coherent state

superposition, we could not investigate the influence of this setting. The simplest way to set it is by investigating the measurements of the coherent states $|\pm\alpha\rangle$. These states become $|0\rangle, |2\alpha\rangle$ in the homodyne detector. Then following the theory in Eqs. (6.11) and (6.12) a justified choice of the x in Eq. (6.8) would be the one equalizing the success probabilities. The success rates of the APD clicks were monitored during the experiment and were $P_{|0\rangle} = 9.3 \cdot 10^{-4}$ and $P_{|2\alpha\rangle} = 0.010$, thus a factor of 11.2 difference. From the marginal distributions for the x-quadrature, we can get an idea of where to find the optimal quadrature. In these results we first of all see the

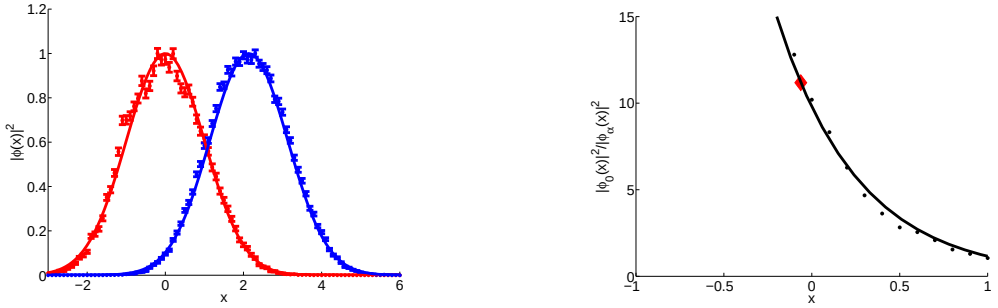

Fig. 6.4: On the left the quadrature distributions for the $|0\rangle$ (red) and $|2\alpha\rangle$ (blue) coherent state inputs. They are both normalized to 1 at the center. On the right the ratio between the two is shown. The red diamond marks the APD success ratio at the optimal heralding quadrature. The solid lines are fits according to theory.

clear Gaussian lumps representing the vacuum and coherent states. The heralding quadrature must be chosen in such a way so the probability ratio is 11.5 to 1 in favor of the vacuum state. Given the size of $\alpha \approx 0.83$ at the measurement station, the heralding quadrature can be found to be $x = -0.06$ with a heralding window of $\Delta x = 0.02$. This point is also marked with a red diamond on the right in Fig. 6.4. This point is seen to fall on the theoretical prediction, thus verifying our choice. The overall success probability with this choice of heralding quadrature is $P \approx 7.0 \cdot 10^{-6}$. The output was subject to full quantum state tomography and reconstructed using maximum likelihood. In the reconstruction we corrected for the total detection efficiency of the homodyne detector, which was estimated to be 0.77 ± 0.02, including efficiency of the diodes 0.93 ± 0.01, visibility 0.95 ± 0.01 and transmission efficiency 0.93 ± 0.02. The phase was inferred using the phase fitting method described in Sec. 5 and adding the optimization procedure also used in Sec. 5.3. The results are shown in Fig. 6.5. The reconstructed output states for both $|-\alpha\rangle$ and $|\alpha\rangle$ can be seen in Fig. 6.5. For the $|-\alpha\rangle$ input the gate yields a state which closely resembles a small odd CSS, which is what we expect from the gate operation. We found the fidelity between the prepared state and an ideal CSS, $(|\alpha\rangle - |-\alpha\rangle)/\sqrt{N_-}$, is maximized for

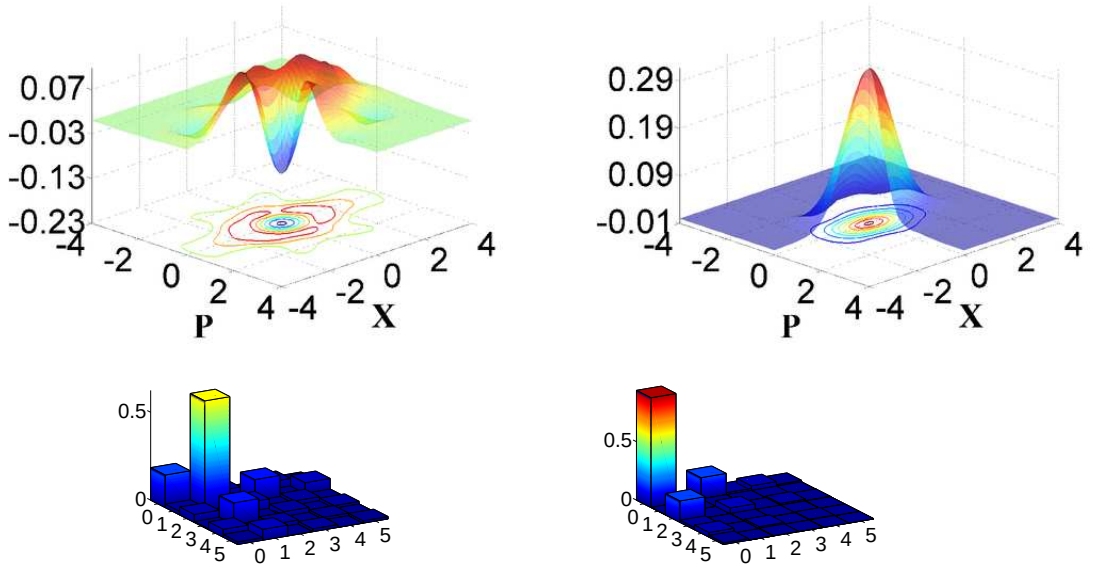

Fig. 6.5: Output states from the CSS Hadamard gate for an input alphabet with $\alpha \approx 0.8$. On the left the output Wigner distribution and density matrix for the $|-\alpha\rangle$ input and on the right for the $|\alpha\rangle$ input.

$\alpha = 0.75$ and reaches a value of $F_{-\alpha} = 0.65 \pm 0.04$. The non-classicality of the superposition state produced by the Hadamard gate can be seen from the negativity of the corresponding Wigner distribution, which is $W(0,0) = -0.11 \pm 0.02$, which is comparable to previous experiments where photon subtraction has been used to prepare non-Gaussian states [104, 51, 50, 113, 154, 89, 88]. The non-classical effects were also observed without correction, with a fidelity of $F_{-\alpha} = 0.55 \pm 0.04$ and a value at the origin of $W(0,0) = -0.05 \pm 0.02$. For the $|\alpha\rangle$ input the output state closely resembles a squeezed state, approximating a small CSS, $(|\alpha\rangle + |-\alpha\rangle)/\sqrt{N_+}$. The fidelity between the prepared state and the ideal CSS for $\alpha = 0.75$ was found to be $F_\alpha = 0.94 \pm 0.02$.

These experimental results only provide a partial test of the gate performance. In order to get information about this we would need to have access to arbitrary CSS' and test the gate for a series of input states. Since this was not experimentally feasible, we worked with Petr Marek from Olomouc on establishing a reliable model for the entire gate operation. We built a model based on the same ideas as in Ch. 3.2 and used it to simulate the gate for arbitrary input states, $u|\alpha\rangle + v|-\alpha\rangle$ with $u = \cos\theta$ and $v = \sin\theta e^{i\varphi}$. The Bloch sphere is then parametrized using $\theta \in [0, \pi/2]$ and $\varphi \in [0, 2\pi]$. With this parametrization the north (south) poles corresponds to the pseudo-orthogonal basis states, $|\alpha\rangle$ ($|-\alpha\rangle$).

Our simulation starts with an arbitrary qubit in the coherent state basis, $|\psi_{\text{in}}\rangle$, for which the global input state reads

$$\hat{\rho}_{\text{in}} = |\psi_{\text{in}}\rangle_1\langle\psi_{\text{in}}| \otimes |0\rangle_2\langle 0| \otimes |0\rangle_3\langle 0| \otimes \hat{\rho}_4^{\text{A}}, \tag{6.17}$$

where the subscripts are used to label the four participating modes and $\hat{\rho}^{\text{A}}$ represents the density matrix of a squeezed thermal state used as the ancillary resource. The action of the gate can now be represented by a unitary evolution of the linear optical elements, $\hat{U}$, followed by POVM elements of successful heralding events $\hat{\Pi}$, with the output state given by

$$\rho_{\text{out}} = \frac{1}{P_{\text{S}}}\text{Tr}_{123}(\hat{U}\hat{\rho}_{\text{in}}\hat{U}^{\dagger}\hat{\Pi}), \tag{6.18}$$

where $P_{\text{S}} = \text{Tr}(\hat{U}\rho_{\text{in}}\hat{U}^{\dagger}\hat{\Pi})$ is the success rate. $\hat{U} = \hat{U}_{23}(t_{\text{BS}})\hat{U}_{12}(t_{\text{ABS1}})\hat{U}_{34}(t_{\text{ABS2}})$ is composed of unitary beam splitter operations coupling the respective modes, and $\hat{\Pi} = \hat{\Pi}_1^{\text{HD}} \otimes \hat{\Pi}_3^{\text{APD}}$ describes the inefficient homodyne and APD measurements.
The predicted gate fidelities and success probabilities are shown in Fig. 6.6. This parameterization is mapped onto the Bloch spheres in Fig. 6.6, where the coloring is representing the value. The fidelity spans the range of $F \in [0.67 : 0.96]$ with an

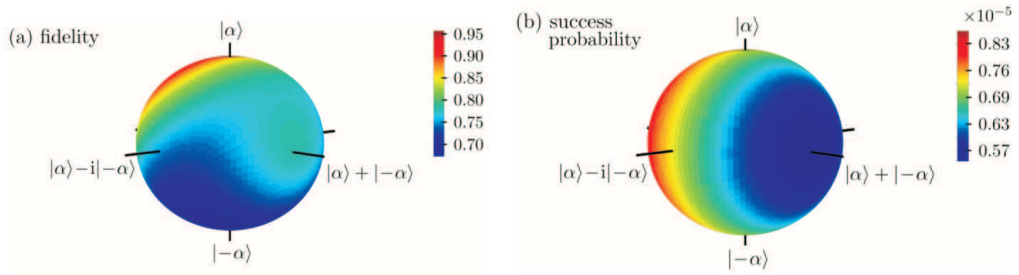

Fig. 6.6: Predicted fidelity a) and success probability b) for the implemented Hadamard gate. The fidelity attains values between 0.67 and 0.96 with the highest value around the north pole. The success probability spans values between $0.55 \cdot 10^{-5}$ and $0.85 \cdot 10^{-5}$ with a value at the poles of $0.72 \cdot 10^{-5}$.

average fidelity of $F_{avg} = 0.78$. Particularly, for the coherent states $|\alpha\rangle$ and $|-\alpha\rangle$ at the input, fidelities of 0.88 and 0.67 are predicted, respectively, which agrees well with the actually measured values. The success probabilities associated with $|\alpha\rangle$ and $|-\alpha\rangle$ are almost equal, thus confirming our choice of heralding quadrature. The average success probability is $P_{avg} = 7.2 \cdot 10^{-6}$.

Summary

In this chapter we presented and investigated a Hadamard gate for coherent state superpositions. We started out with some general discussion on the Hadamard transformation and the implementation for coherent state superpositions. This discussion focused on the consequences of the non-orthogonality of the basis states, and how this in principle results in an ill-defined Hadamard transformation. It was discussed how only certain features of the Hadamard transformation could be retained, except in the limit of $\alpha \to \infty$.

Then our practical implementation of the gate was presented. Here, the possibility to switch between the two choices of normalization, Eqs. (6.11) and (6.15), by setting experimental parameters were discussed. Finally, considerations regarding the alternative resource state were presented. The squeezed state resource was found to be a good substitute for the true CSS provided that $\alpha \leq 1$.

In the experimental implementation the main focus was on the changes compared to the setup presented in Ch. 4. Finally the experimental results and a theoretical model for predicting gate performance were discussed. The experimental results showed good agreement with the theoretical predictions, which gave an average gate-fidelity of 71%.

Chapter 7

Applications of coherent state superpositions

Having coherent state superpositions of sufficiently high quality available in an experimental setting enables the implementation of various interesting protocols. We have theoretically investigated some of these applications, and from this made predictions as to the feasibility of two main protocols.
The first protocol is a scheme for manipulating coherent state superpositions using Gaussian operations. The investigated protocol can be split into three different cases. The first case is a protocol which enables coherent attenuation of the CSS amplitude. The second case is a protocol for purifying a decohered CSS. The third case is a more general implementation of a phase rotation gate [43], which is capable of generating an arbitrary state on the Bloch-sphere.
The second protocol is a scheme for entanglement distillation using photon subtraction from a squeezed vacuum state. It is based on multiple subtractions and displacements and is reminiscent of a protocol suggested by Fiurášek [155]. We find that using single mode squeezed states as a resource it is, in principle, possible to outperform the protocol for two-mode squeezed states, in the limit of low gain.

7.1 Coherent attenuation of coherent state superpositions

Coherent state superpositions are extremely fragile in lossy conditions. Not only does the amplitude decrease in a lossy channel, but even worse is the loss of the internal quantum coherence of the superposition. Transmitting a CSS through a channel with a transmission of no more than 50% will almost completely destroy

all quantum coherence in the state. It will decohere into a mixture of itself and the orthogonal superposition

$$\begin{aligned} |\Psi\rangle_{in} &= |\alpha\rangle - |-\alpha\rangle \Rightarrow \\ \hat{\rho}_{out} &\approx \frac{1}{2}\left|\text{cat}\left(\frac{\alpha}{\sqrt{2}},0\right)\right\rangle\left\langle\text{cat}\left(\frac{\alpha}{\sqrt{2}},0\right)\right| + \frac{1}{2}\left|\text{cat}\left(\frac{\alpha}{\sqrt{2}},\pi\right)\right\rangle\left\langle\text{cat}\left(\frac{\alpha}{\sqrt{2}},\pi\right)\right| . \end{aligned} \quad (7.1)$$

Now, this will happen independently of the input CSS amplitude. If we further consider the fidelity as a function of loss for different input amplitudes, we notice a perhaps more problematic property of the CSS'. From Fig. 7.1 we have that the rate of decoherence is faster for increasing CSS amplitude. The rate of decoherence is approximately proportional to $(1-\eta)|\alpha|^2$ where $1-\eta$ is the loss. From this it is clear that as α increases, the more rapid the decoherence will destroy the state and render it useless in quantum information protocols. The apparent difference between the loss dependence for the even and odd CSS' is due to the structure of the states. For the even CSS the vacuum, $|0\rangle$, is a part of the initial state and will always remain, regardless of the strength of the loss. For losses higher than 50% the vacuum contribution will even start to dominate and be the lower limit for the fidelity. This is of no pratical importance, since it is not possible to extract any useful information from such a state. For the odd CSS the influence of loss is clearer. Here it is clearly seen how the decoherence is much faster for larger than for smaller amplitudes. Now, what can be done? If the loss is larger than 50%, then Fig. 7.1

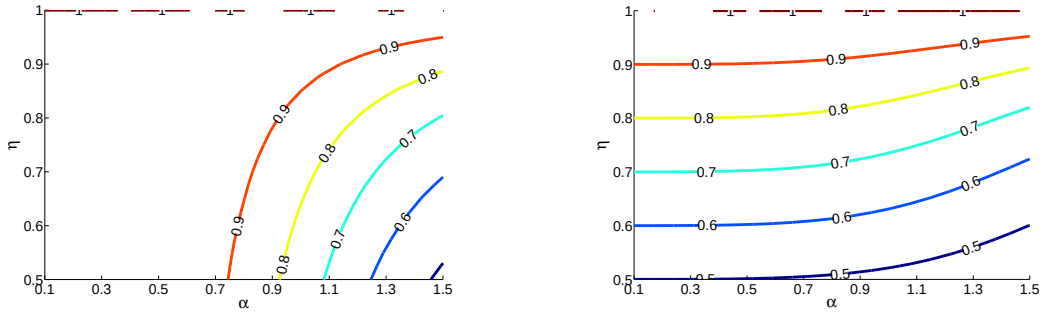

Fig. 7.1: Fidelity between input and output states with a even (left) and (odd) CSS through a lossy channel with transmission η.

seems to suggest that nothing can be done. But if the loss is lower than this, it would seem that it is better to send a CSS with a small rather than a large amplitude. So a solution could be to somehow reduce the amplitude of the CSS before transmitting it through the lossy channel. If we look at one of the intermediate calculations of the protocol for increasing the amplitude of the CSS, Eq. (3.21), it would appear that

this can be done using only Gaussian operations. By implementing an operation where a CSS input is mixed with vacuum on a beam splitter with transmittance, $|t|^2$, Fig. 7.2,

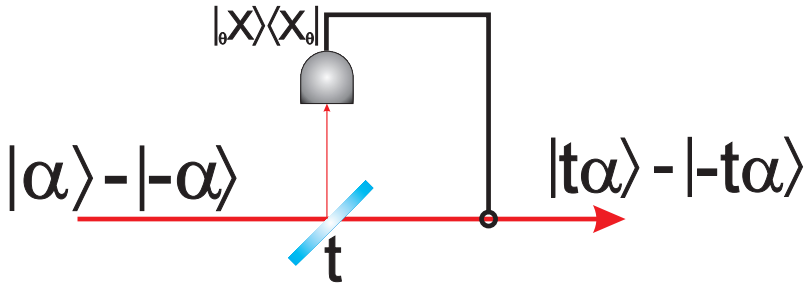

Fig. 7.2: Setup for manipulating coherent state superpositions using only Gaussian operations. An input CSS is split on a beam splitter and one part is measured using homodyne detection. Heralded on a specific quadrature the output CSS will have a reduced amplitude.

the pre-measurement state will be the entangled state

$$\begin{aligned} |\Psi_{in}\rangle &= |\alpha\rangle + e^{i\varphi}|-\alpha\rangle, \Rightarrow \\ |\Psi\rangle &= |t\alpha\rangle|r\alpha\rangle + e^{i\varphi}|-t\alpha\rangle|-r\alpha\rangle, \end{aligned} \tag{7.2}$$

where $r = \sqrt{1-|t|^2}$. If we are now able to implement a measurement, $\langle\hat{\Pi}|$, such that $\langle\hat{\Pi}|r\alpha\rangle = \langle\hat{\Pi}|-r\alpha\rangle$, the transmitted mode will be prepared in a CSS with smaller amplitude, $t\alpha$ while maintaining the parity phase, φ, of the input. Using Eq. (3.20) with $x = 0$, we find,

$$|\Psi_{out}\rangle = e^{-\frac{1}{2}e^{-2i\theta}(r\alpha)^2-\frac{1}{2}|r\alpha|^2}(|t\alpha\rangle + e^{i\varphi}|-t\alpha\rangle) \tag{7.3}$$

In this way we can prepare a CSS with a smaller amplitude, $t\alpha$, by performing homodyne detection on the reflected port and heralding on the value $x = 0$. The output will only have a global phase, which depends on the measured quadrature direction, θ. The protocol can be proven to be universal in the sense that it works regardless of the setting of θ. A more general description of a homodyne detector, where no determination is made on the phase would be

$$\hat{\Pi} = \int_{-\pi}^{\pi} |X_\theta\rangle\langle X_\theta| d\theta. \tag{7.4}$$

Using this in Eq. (7.2) we find

$$|\Psi_{out}\rangle = (|t\alpha\rangle + e^{i\varphi}|-t\alpha\rangle)\int_{-\pi}^{\pi} e^{-\frac{1}{2}e^{-2i\theta}r\alpha^2-\frac{1}{2}|r\alpha|^2}d\theta. \tag{7.5}$$

In this way it is possible to universally attenuate an input CSS with arbitrary strength. A somewhat peculiar behavior becomes apparent if we investigate the success probability and the mean number of photons as a function of attenuation and input CSS parity . The results are shown in Fig. 7.3. If one looks at the mean

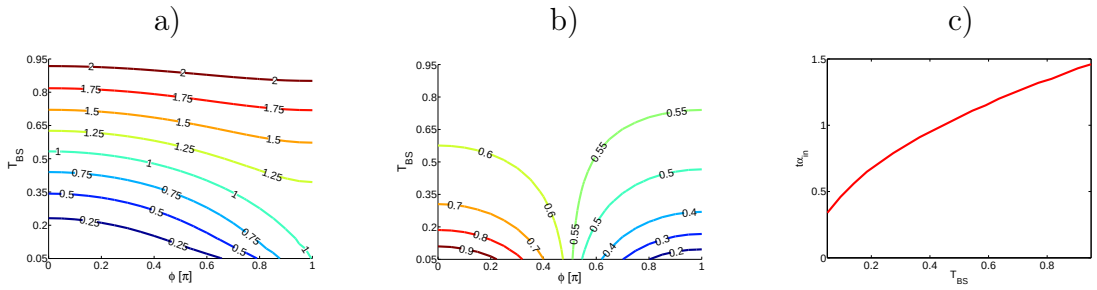

Fig. 7.3: a) The mean photon number, n, of the output state and b) the success probability P, both as function of T_{BS} and φ. c) the amplitude of the corresponding output CSS as a function of T_{BS}. The amplitude of the input CSS was set to $\alpha = 1.5$.

number of photons (a) and consider the case where $\varphi \rightarrow \pi$, the mean number of photons would appear to converge to one. This is the number of photons in an odd CSS where $\alpha \rightarrow 0$. In all other cases the mean number of photons vanishes. What happens is that the protocol collapses the excitation of the CSS into the lowest possible level, which for $\varphi = \pi$ is $|1\rangle$ and $|0\rangle$ otherwise. From Fig. 7.3 c) we can also see, that the amplitude of the output CSS scales like $\sqrt{T}$, as expected.

We built the experimental setup to such a condition that a preliminary experimental test could be carried out. This work was carried out in collaboration with Dr. Amine Laghaout. The experimental setup is the same as used for the Hadamard gate experiment, Fig. 6.3. We measured a series of photon subtracted states, all with a pump power of 4 mW. All settings were close to the parameters presented in Ch. 4. The attenuation beam splitter was implemented using PBS2. The attenuation was tuned using a half-wave plate in front of this PBS. The transmittance of the attenuation beam splitter was varied in 6 steps from $T \approx 1.00$ to $T = 0.62$. For each setting a series of 50 traces of 4000 quadratures was recorded. The two homodyne detectors, also used for the Hadamard gate experiment were sampled simultaneously at the same phase, θ. This phase was scanned 2π during the course of a single trace.

During the processing the first step was to infer the phase. This was done using the same technique as in Ch. 5. After this the heralding procedure was applied as post-selection. We heralded the attenuated CSS based on three different heralding windows, $\Delta x \approx, \pm 0.25, \pm 0.1$ and 0.025. In the reconstruction the effect of finite detection efficiency, $\eta = 0.73$, was taken into account. The slight decrease in

detection efficiency, compared to the previous cases, was caused by a slight decrease in visibility. The first preliminary results for the attenuation protocol are shown in Fig. 7.4. For each heralding window 6 different states were reconstructed, one for

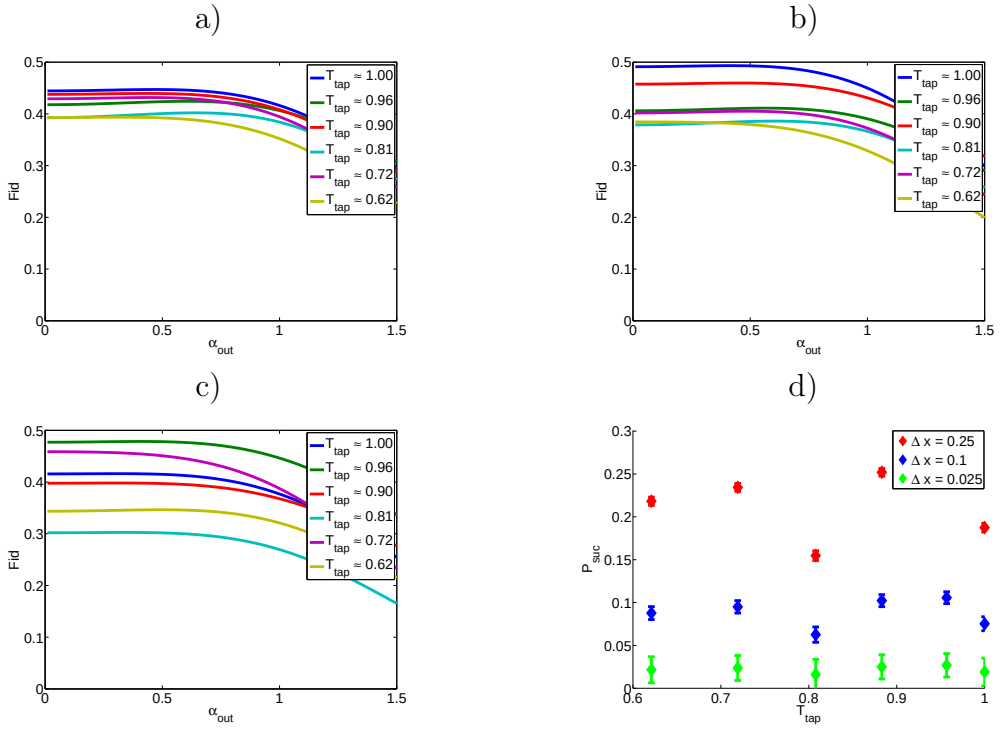

Fig. 7.4: Figs. a)-c) shows fidelity between the reconstructed output states and $|\alpha\rangle - |-\alpha\rangle$ as a function of α, for the different settings of tap-off ratio. Figs. a) is for a heralding window of $\Delta x = 0.25$, b) for $\Delta x = 0.1$ and c) $\Delta x = 0.025$. Fig. d) shows the success probability as a function of tap-off ratio for the different settings of heralding window.

each setting of the tap-off beam splitter. In Fig. 7.4 we show the fidelity between the reconstructed state and an odd CSS as a function of α

$$\frac{1}{N_-(\alpha)}(\langle\alpha| - \langle\alpha|)\hat{\rho}_{out}(|\alpha\rangle - |\alpha\rangle) \tag{7.6}$$

Now, we would expect the α value where this fidelity is peaking to decrease as the tap-off ration is increasing. These results, however, do not show a clear decrease in the CSS amplitude with increasing tap-off ratio. If anything, the amplitude is increasing when the tap-off ratio is increased. The results seem to be slightly better for a heralding window of $\Delta x = 0.1$, with the starting point, $T \approx 1$, almost reaching 50% fidelity. It is not yet clear why the fidelity for the $T \approx 1$ case shows a rather strong dependence on the width of the heralding window. In this case no correlations should be present in the pre-heralding state and thus no dependence on

heralding should be present. This is, however, the case. Looking at the rest of the results, we see that for increasing tap-off the peak fidelity is decreasing. For larger tap-offs it is somewhat difficult to deduce the α-value for the peak-fidelity and thus difficult to tell if the protocol is successful. Considering the success probability, Fig. 7.4 d), we see that it is virtually constant, $P \approx 0.2$ for $\Delta x = \pm 0.25$, $P \approx 0.1$ for $\Delta x = \pm 0.1$ and $P \approx 0.02$ for $\Delta x = \pm 0.025$. It is not entirely clear why the success probability sees a dip around $T = 0.8$, but from the fidelities we also see that the result for $T = 0.8$ is in no way following any expected behaviour. It is generally the tap-off that results in the largest amplitude of the output CSS, albeit with a fairly low fidelity. This fidelity is further more decreasing with narrowing window.

7.2 Purification of noisy coherent state superposition

The coherent state superpositions prepared in Ch. 5 are not of particular high quality. A protocol for partially "cleaning up" decohered CSS' have been proposed by Suzuki *et al.* [156]. The idea is to tap of a small fraction of the decohered CSS and measure it using homodyne detection. The protocol is dealing with the system shown in Fig. 7.5. Expressed in mathematical terms a decohered CSS

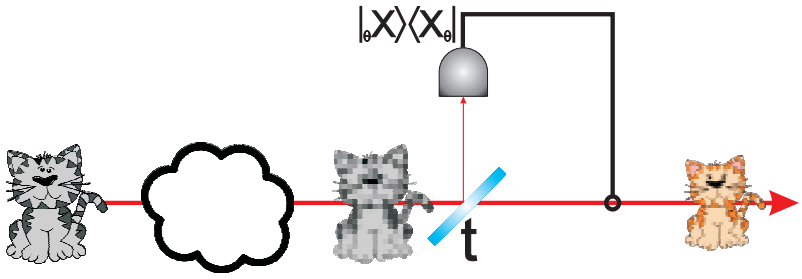

Fig. 7.5: An input CSS is decohered through a lossy channel and only a fraction of the original CSS remains. By tapping of a fraction and heralding a specific quadrature the output can be a partially "cleaned" up CSS, with a different parity phase.

$$\hat{\rho}_{\eta,in} = p(\eta)\hat{\rho}_{\eta\alpha,\varphi} + (1 - p(\eta))\hat{\rho}_0 \tag{7.7}$$

can be transformed into the state

$$\hat{\rho}_{out} = P\hat{\rho}_{t\eta\alpha,0} + (1 - P)\hat{\rho}_0, \tag{7.8}$$

where $p(\eta)$ is a constant depending on the loss $1-\eta$, $\rho_{\eta\alpha,\varphi}$ is the real CSS and $\rho_0 = 1/2\,|\eta\alpha\rangle\langle\eta\alpha| + 1/2\,|-\eta\alpha\rangle\langle-\eta\alpha|$. If the condition $P > p(\eta)$ can be obtained by an appropriate choice of operation, we would have increased the portion of pure CSS. The protocol works by tapping of a small fraction, $|r|^2$, of the CSS and measuring it using homodyne detection. By appropriate choice of heralding quadrature x and homodyne phase θ, the state in Eq. (7.8) can be prepared. The optimal phase space direction to measure along is depending on the parity, φ, of the input state according to $\theta + \varphi = 0$. From Eq. (7.8) a few things become apparent; First of all, the parity information of the input CSS is lost in the output CSS. Secondly, the state in Eq. (7.8) is mixture of two non-orthogonal states. In fact the fidelity between the two states approaches unity as $t\eta \to 0$. For this reason Suzuki *et al.* [156] did not use fidelity as a way to quantify the performance of the protocol. They simply considered the expansion coefficients, $p(\eta)$ and P, and found the conditions for which $P > p(\eta)$, and the content of pure CSS had been increased.
The decomposition in Eq. (7.7) works fine in theory. When the starting point is a pure CSS through a lossy channel, the theoretical description will yield that expression. When dealing with realistic states, the decohered mixture in Eq. (7.7) will not be able to perfectly describe the state. And since the two constituents of the mixture are non-orthogonal, it is difficult to find the coefficients in the decomposition. But we can use the fidelity, $F(\hat{\rho}_{out}, \hat{\rho}_{t\eta,in})$, to get an idea on the applicability of this purification protocol for our prepared photon subtracted states. Using the states prepared in Ch. 5 we have simulated the effect of the purification protocol. The graphs in Fig. 7.6 are simulations of the protocol performance for two different input states. The simulation is carried out for input states given by the photon sub-

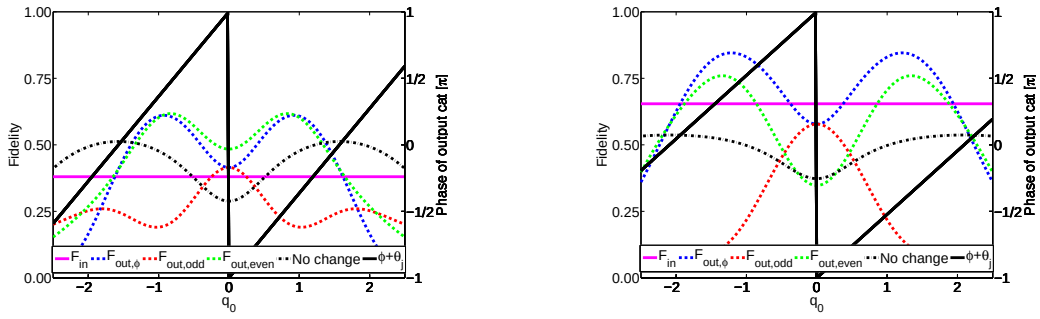

Fig. 7.6: Predicted fidelity for a potential purification protocol applied to some of our prepared photon subtracted states. On the left for the state presented in Fig. 5.7 and the right is for the odd CSS state prepared in the Hadamard gate experiment.

tracted state for 8mW pump power, Fig. 5.7, and for the, $|\alpha\rangle - |-\alpha\rangle$ state prepared

in the Hadamard gate experiment, Fig. 6.5. The tap-of fraction is set to 50%. Many curves are shown in this figure so we will list what they represent:

1) The horizontal magenta line, F_{in}, is the fidelity of our input state with an odd CSS with optimized amplitude.

2) The blue dashed line is the fidelity between the heralded state and an ideal CSS with parity given by the phase from the black solid line. This phase will depend on the heralding quadrature. Here the phase is set according to theory based on the heralding quadrature, the tap-of fraction and the fitted value for α for the ideal protocol, Eq. (7.8).

3) The dashed red line is the fidelity between the heralded state and an ideal odd CSS with appropriate amplitude. This fidelity will depend on the heralding quadrature and is seen to be maximized for a value around $q_0 \approx 0$.

4) The green dashed line is the fidelity between the heralded state and an ideal even CSS with appropriate amplitude. This fidelity will depend on the heralding quadrature and is seen to be maximized for a value around $q_0 \approx \pm 1$.

5) The black dash-dotted line is the fidelity between the unheralded state and an ideal CSS with phase given by the black line. Thus, the same benchmark as used for 2).

6) The solid black line is the predicted parity phase of the heralded output, φ_{out}, based on the ideal theory.

The goal of the protocol is to have higher fidelities at the output and, at the same time, maximize the distance between the black dash-dot line and the blue (or green) dashed lines. In both cases this is achieved at a heralding quadrature which will result roughly in a phase of the output CSS of $\theta = \pm\pi/2$. This is in contrast with the ideal protocol which should result in $\varphi = 0$. The reason for the discrepancy is not yet fully understood, but we believe it is not a failure of the model. The model is successful in predicting the behavior for an ideal input state as the one given in Eq. (7.7).

7.3 Preparation of arbitrary coherent state superpositions

So far we have dealt mostly with either the odd or the even coherent state superpositions. The main reason for this obviously being that the odd CSS is what is prepared by photon subtraction from squeezed vacuum. However, in order to verify the operation of gates and operations for CSS', such as the Hadamard gate in Ch. 6, arbitrary CSS' are generally needed. The only successful preparation of arbitrary CSS' was implemented by Neergaard-Nielsen *et al.* by combining the photon subtraction with displacement [154]. By displacing the state before subtraction they were able to prepare states on multiple positions on the Bloch-sphere. Here we present a different approach, where an already prepared known CSS' is rotated into a different CSS using only Gaussian operations. The protocol is similar to the gates proposed by Ralph *et al.* [43], but rely on a probabilistic Gaussian measurement instead of photon counters.

7.3.1 Arbitrary CSS using homodyne detection

The protocol is fairly simple and in reality just an extension of the two previously described protocols. A small fraction of a CSS is tapped off on a beam splitter and one part is detected using homodyne detection. The output will be given by

$$|\Psi_{out}\rangle \quad = \quad e^{-\frac{1}{2}x^2-\frac{1}{2}e^{-2i\theta}(r\alpha)^2-\frac{1}{2}|r\alpha|^2-\sqrt{2}e^{-i\theta}xr\alpha}(|t\alpha\rangle - |-t\alpha\rangle\, e^{2\sqrt{2}e^{-i\theta}xr\alpha}),$$

where we have assumed $\varphi_{in} = \pi$ as in our experimental case. Now by measuring a specific quadrature direction, θ, and heralding on a specific quadrature, x, any state on the CSS Bloch sphere can be reached.

$$\begin{aligned}
|\Psi_{out}\rangle &= |t\alpha\rangle - |-t\alpha\rangle\, e^{2\sqrt{2}(\cos\theta - i\sin\theta)xr\alpha} \\
&= |t\alpha\rangle - |-t\alpha\rangle\, e^{2\sqrt{2}\cos(\theta)xr\alpha}(\cos(2\sqrt{2}\sin(\theta)xr\alpha) - i\sin(2\sqrt{2}\sin(\theta)xr\alpha)) \\
&= |t\alpha\rangle - |-t\alpha\rangle\, e^{2\sqrt{2}\cos(\theta)xr\alpha}\cos(2\sqrt{2}\sin(\theta)xr\alpha) \\
&\quad + i\,|-t\alpha\rangle\, e^{2\sqrt{2}\cos(\theta)xr\alpha}\sin(2\sqrt{2}\sin(\theta)xr\alpha)
\end{aligned} \tag{7.9}$$

By tuning θ and x, any superposition of $|t\alpha\rangle$ and $|-t\alpha\rangle$ can be reached. First we fix the argument of the trigonometric functions by setting x

$$x \quad = \quad \frac{A_0}{2\sqrt{2}\sin(\theta)r\alpha}, \tag{7.10}$$

where A_0 is some arbitrary value desired for the argument of the trigonometric functions. Inserting this into Eq. (7.9) we find

$$|\Psi_{out}\rangle \quad = \quad |t\alpha\rangle - (\cos(A_0) - i\sin(A_0))e^{A_0\cot(\theta)}\,|-t\alpha\rangle\,. \tag{7.11}$$

From this we can see how, by varying A_0, we can move around the longitudes of the Bloch-sphere, while θ allows us to move up and down the latitudes. In Tab. 7.1 six particular cases are shown. From these it is seen that, if the phase space direction

A_0	θ	x	$\|\Psi_{out}\rangle$
$\frac{(4k+1)\pi}{2}$	$\frac{\pi}{2}$	$\frac{(4k+1)\pi}{4\sqrt{2}r\alpha}$	$\|t\alpha\rangle + i\,\|t\alpha\rangle$
$\frac{(4k-1)\pi}{2}$	$\frac{\pi}{2}$	$\frac{(4k-1)\pi}{4\sqrt{2}r\alpha}$	$\|t\alpha\rangle - i\,\|t\alpha\rangle$
$2k\pi$	$\frac{\pi}{2}$	$\frac{k\pi}{\sqrt{2}r\alpha}$	$\|t\alpha\rangle - \|-t\alpha\rangle$
$(2k+1)\pi$	$\frac{\pi}{2}$	$\frac{(2k+1)\pi}{2\sqrt{2}r\alpha}$	$\|t\alpha\rangle + \|-t\alpha\rangle$
$\to\ \infty$	$\neq\ \frac{\pi}{2}$	$\to \infty$	$\to\ \|-t\alpha\rangle$
$\to\ -\infty$	$\neq\ \frac{\pi}{2}$	$\to -\infty$	$\to\ \|t\alpha\rangle$

Tab. 7.1: Choices for A_0, θ and x for reaching the 6 "poles" of the Bloch sphere, $k \in \mathbb{Z}$.

conjugate to the CSS displacement direction, $\theta = \pi/2$, is measured, the traversing of heralding quadrature $x \in\ ]-\infty : \infty[$ will result in a movement around the equator of the Bloch sphere. If we measure a quadrature for which $\theta \neq \pi/2$, the same traversing will result in a spiraling motion from the south pole $|-t\alpha\rangle$ to the north pole $|t\alpha\rangle$, where $x = 0$, naturally is crossing the equator. This procedure is reminiscent of the one used in for instance [43].
The experimental investigation of this protocol, should be realisable using the same experimental system, as for the attenuation and purification experiments. This is a path currently being pursued in the laboratory. Protocols similar to this suggestion have been used to prepare small amplitude CSS' from Fock states [157, 158].

7.4 Entanglement distillation using squeezed vacuum

Entanglement is perhaps the most perplexing and least understood concept in quantum mechanics[1]. It is the property where a multipartite state cannot be described

[1]One could argue somewhat humorously, that due to our lack of understanding of quantum entanglement, the even less understood and more perplexing concept of quantum discord have been introduced [159].

fully by a multitude of local descriptions of individual sub-states. For pure states it means that a multipartite state on $\mathbb{H}_{AB} = \mathbb{H}_A \otimes \mathbb{H}_B$ cannot be described by a tensor product of states on individual subsystems, $\mathbb{H}_A$, $\mathbb{H}_B$:

$$\begin{aligned} |\Gamma\rangle &= \sum_i c_i \, |\psi_i\rangle_A \, |\varphi_i\rangle_B \\ &\neq \sum_i a_i \, |\psi_i\rangle_A \sum_j b_j \, |\varphi_j\rangle_B = |\Psi\rangle_A \, |\Phi\rangle_B . \end{aligned} \tag{7.12}$$

For mixed states described by the density matrix formalism the condition for being entangled (or inseparable) is that a multipartite state can not be written as a convex mixture of product states, [140],

$$\hat{\rho}_{AB} \neq \sum_i C_i \hat{\rho}_i^A \otimes \hat{\rho}_i^B. \tag{7.13}$$

Entanglement is a fragile resource and often the fragility is increasing with the amount of entanglement. For this reason much research is focused on the derivation and realization of protocols where a few highly entangled states are prepared from a larger ensemble of weakly entangled states. This is the idea by behind entanglement distillation.

7.4.1 Entanglement distillation

For Gaussian entanglement a no-go theorem exist saying that this cannot be done purely by local Gaussian operations and classical communication [31, 32]. However, by including non-Gaussian systems and operations it is still possible to distill entanglement from Gaussian states [160, 161, 162]. This has been demonstrated for non-local photon subtraction [40], non-Gaussian decoherence [163] and local non-Gaussian operations [41].

In 2000 Opatrný *et al.* showed that entanglement could be distilled from Gaussian states using local photon subtractions and classical communication [164]. Their starting point was the two-mode squeezed state,

$$|\zeta_2\rangle_{AB} = \sqrt{1-\gamma_2^2} \sum_{n=0}^{\infty} \gamma_2^n \, |n\rangle_A \, |n\rangle_B \tag{7.14}$$

In the limit of weak initial entanglement, $\gamma_2 \ll 1$, the protocol with two local

photon subtractions would prepare the entangled state,

$$|\psi^{\gamma_2}\rangle \approx |00\rangle + 2\gamma_2 |11\rangle \tag{7.15}$$

This approach could also be used to distill entanglement from Gaussian states under physically realistic conditions [165]. In 2011 Zhang and van Loock [166] found an optimized version of the protocol, where the amount of entanglement could be improved by local Gaussian operations. Their proposal was to apply local squeezing operations at A and B before the photon subtractions. Relating the local squeezing to the initial entanglement through $\gamma_{AB} = \tanh(r) = \sqrt{\gamma_2}$, the distilled entangled state would look like

$$|\psi^{\gamma_2}\rangle = \gamma_2(|00\rangle + |11\rangle) + O(\gamma_2^{3/2}), \tag{7.16}$$

which has larger degree of entanglement than the one in Eq. (7.15). Around the same time Fiurášek found an alternative protocol where the squeezing operations of Zhang and van Loock were exchanged with two local displacement operations [155]. Keeping the following relation between the initial degree of entanglement and the local displacements, $\alpha_A = -\alpha_B = \sqrt{\gamma_2}$, the distilled entangled state would be

$$|\psi^{\gamma_2}\rangle = \gamma_2^{3/2}(|10\rangle - |01\rangle) + O(\gamma_2^2). \tag{7.17}$$

This state has the same amount of entanglement as the one in Eq. (7.16), although in a different configuration. Common for both approaches is the distillation of a Bell state from an initial state with vanishing entanglement. The first protocol, resulting in Eq. (7.15), was experimentally demonstrated by Takahashi *et al.* in 2010 [41].
The proposals by Opatrný, Zhang and van Loock and Fiurášek all rely on the two-mode squeezed state, Eq. (7.14), as the initial entangled resource. It fulfills these relations between the two-mode quadratures,

$$\mathrm{Var}(\hat{x}_A + \hat{x}_B) = \frac{1}{2}e^{-2r}, \quad \mathrm{Var}(\hat{p}_A - \hat{p}_B) = \frac{1}{2}e^{-2r} \tag{7.18}$$

This state is the optimal among all Gaussian entangled states in terms of amount of entanglement as a function of resources needed. But the preparation of this state is a challenging task. Either two-mode squeezing must be prepared in a SPDC process which is often not a very efficient process. For this reason the usual approach is to mix two single-mode squeezed states on a balanced beam splitter which puts strong requirements on the initial squeezed states and the system stability.

Here we propose and investigate an alternative protocol, based on a more readily available Gaussian entangled state. Our starting point is the single-mode squeezed state, Eq. (2.37)

$$|\zeta_1\rangle \quad = \quad (1-\gamma_1^2)^{1/4} \sum_{n=0}^{\infty} \frac{\sqrt{(2n)!}}{n!} \left(\frac{\gamma_1}{2}\right)^n |2n\rangle \,, \tag{7.19}$$

which after splitting on a balanced beam splitter gives the entangled state

$$|\Psi\rangle_{AB} \quad \approx \quad |00\rangle + \frac{\gamma_1}{\sqrt{2}} \left(\frac{1}{2}|20\rangle + \frac{1}{\sqrt{2}}|11\rangle + \frac{1}{2}|02\rangle\right) + O(\gamma^2). \tag{7.20}$$

Here we have assumed a low degree of squeezing, $\gamma_1 \ll 1$. This state is entangled, although by a lower amount than the state in Eq. (7.14). Following the ideas by Opartný, Zhang and van Loock and Fiurášek, the aim is to remove the vacuum product, $|00\rangle$, since this contribution is highly undesirable when preparing entanglement. From Eq. (7.20) it is seen, that this can be accomplished simply by performing a photon subtraction on either mode A or B. The result would be

$$\begin{aligned} |\Psi\rangle_{AB} \quad &= \quad \hat{a}_A \otimes \mathbb{1}_B |\Psi\rangle_{AB} \\ &= \quad \frac{\gamma_1}{\sqrt{2}} \left(\frac{1}{\sqrt{2}}|10\rangle + \frac{1}{\sqrt{2}}|01\rangle\right), \end{aligned} \tag{7.21}$$

which is maximally entangled state. This process is fully equivalent to subtracting a single photon from a squeezed vacuum and subsequently splitting the result on beam splitter. In the weak squeezing limit, this will result in this de-localized photon. From Eq. (7.21) it is clear that performing subtractions on both modes at the same time, $\hat{a}_A \otimes \hat{a}_B$, will not result in any improvement. But following the idea by Fiurášek we got the idea to investigate the behavior when local displacements were allowed. The full operation on the state will then be given by,

$$\begin{aligned} \hat{F}_{AB} \quad &= \quad (\hat{D}_A^\dagger(\alpha)\hat{a}_A\hat{D}_A(\alpha)) \otimes (\hat{D}_B^\dagger(\beta)\hat{a}_B\hat{D}_B(\beta)) \\ &= \quad (\hat{a}_A\hat{a}_B + \alpha\hat{a}_B + \beta\hat{a}_A + \alpha\beta) \end{aligned} \tag{7.22}$$

Applying this operator to the state in Eq. (7.20) we find

$$|\Psi\rangle \quad = \quad \left(\alpha\beta + \frac{\gamma_1}{\sqrt{2}}\right)|00\rangle + \frac{\gamma_1}{\sqrt{2}}(\beta+\alpha)\frac{|10\rangle + |01\rangle}{\sqrt{2}}$$

$$+\frac{\gamma_1}{\sqrt{2}}\alpha\beta\left(\frac{1}{2}|20\rangle+\frac{1}{\sqrt{2}}|11\rangle+\frac{1}{2}|02\rangle\right)+O(\gamma_1^2). \tag{7.23}$$

Now the vacuum product can be removed by setting

$$\alpha \;=\; -\beta \;=\; \sqrt{\frac{\gamma_1}{2}}, \tag{7.24}$$

resulting in the state

$$|\Psi\rangle \;=\; -\frac{\gamma^2}{2\sqrt{2}}\left(\frac{1}{2}|20\rangle+\frac{1}{\sqrt{2}}|11\rangle+\frac{1}{2}|02\rangle\right)+O(\gamma^3), \tag{7.25}$$

which is a de-localized two-photon Fock state. Evaluating the entanglement of this state in terms of the logarithmic negativity [167, 168, 169, 170, 140] it is found to be more entangled than the state prepared by the previously suggested protocols, $E_N \approx 1.54$ [2]. Comparing the success probability of the different suggested protocols, the Opartný protocol scales as γ_2^2, the Fiurášek protocol as γ_2^3 and our proposal as γ_1^4. For low gains, $\gamma_1, n \ll 1$, this means scaling with mean number of photons, n, for Opartný, with $n^{3/2}$ for Fiurášek and with n^2 for our proposal. We compared our protocol with the Fiurášek protocol in terms of amount of entanglement as a function of mean number of photons in the initial entangled resource and found the result shown in Fig. 7.7. Looking at the results it is clear that our protocol yields more

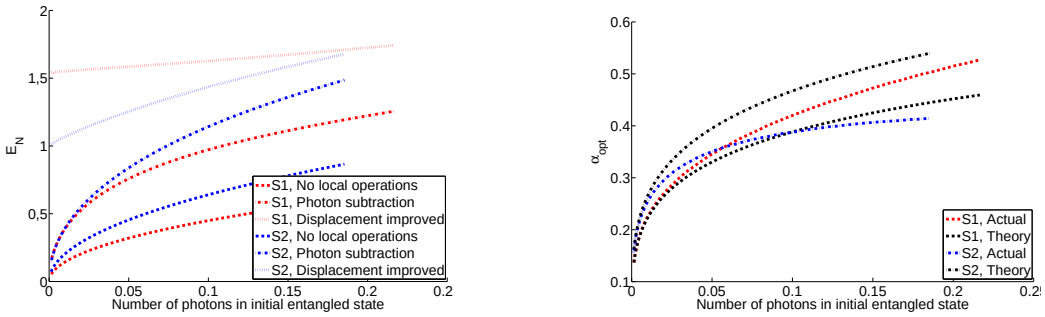

Fig. 7.7: Degree of entanglement (in terms of logarithmic negativity) for the Fiurášekprotocol (blue) and our proposal (red). The dashed lines are for no local operations, the dash-dotted line is for local subtractions and the dotted line is for subtractions with optimal displacements. On the right the optimal displacements (blue and red) compared to the theoretical low-gain predictions.

[2] The notion that the state in Eq. (7.25) is more entangled than the on in Eq. (7.17) is somewhat ambiguous. It is more entangled in terms of the logarithmic negativity which is a measure defined for the density matrix. But the Hilbert space for the state in Eq. (7.25) is in principle larger than for the state in Eq. (7.17). The latter is in fact the maximally entangled state for a Hilbert space of $\dim(\mathbb{H}) = 2\times 2$, while the state resulting from our proposal is in fact not the maximally entangled state for a Hilbert space of $\dim(\mathbb{H}) = 3\times 3$.

entanglement in the low gain regime, $n \ll 1$. However, when the gain increases, the performance of the Fiurášek protocol quickly surpasses our suggestion. But the low-gain regime is often of interest, since entanglement in this region is fairly easy to prepare, manipulate and maintain.

Summary

In this chapter we presented 4 ideas for further experimental investigations, which could potentially be carried out in our present system, only with small modifications. The first proposal was a protocol for coherently decreasing the amplitude of a coherent state superposition. This protocol was motivated by the fragility of large-amplitude CSS's. The protocol works by tapping of a fraction of a CSS and detecting it using homodyne detection. The protocol is currently being investigated in the laboratory and the first preliminary results were presented.
The second protocol was a purification protocol put forward by Suzuki *et al.* and further elaborated on this thesis. It was a simple feasibility study of a protocol presented by Suzuki *et al.* [156] based on our prepared photon subtracted states. We found that the protocol should be able to purify our CSS's to fidelities of more than 50%, however with the cost of reduced size and loss of parity phase.
The third protocol was a generalized version of the previous two. Here the tap-off from a CSS and subsequent homodyne detection is intended to be used for preparation of arbitrary CSS's for testing quantum gates. It was found that any point on the Bloch sphere could potentially be reached using this technique.
Finally an idea for an entanglement distillation protocol was discussed. The idea is closely related to the work by Opatrný *et al.* [164], Zhang and Loock [166] and Fiurášek [155]. Instead of the two-mode squeezed state used in previous protocols, we propose to use a simple single-mode squeezed state split on a beam splitter as the initial entangled state. We find that this can in principle produce a more entangled state in the limit of low gain.

Chapter 8

Conclusion and outlook

In this thesis we set out to implement a protocol for preparing small amplitude CSS' by photon subtraction from squeezed states. We did this by first trying to establish a model for the photon subtraction experiment. Using this model we could make predictions regarding the limitations on the quality of the prepared states. Then we designed and thoroughly investigated the experimental setup for preparing the photon subtracted states. Finally we carried out a series of photon subtraction experiments and reconstructed the prepared states using maximum likelihood.
After this, we implemented a Hadamard gate for coherent state superpositions. This gate was based on a proposal by Marek and Fiurášekand was successfully implemented with average gate fidelities of more than 50%.

8.1 The preliminary work

8.1.1 Modelling the experiment

In Ch. 3 we established a model for predicting the the experimental quality of any prepared states in a photon subtraction experiment. From this model we found that squeezing purities should be higher than 90%, if the resource was supposed to be applicable in photon subtraction experiments. This model was expanded in order to investigate if the prepared states could potentially be used in a protocol, where two CSS' with small amplitude were mixed and the output was projectively measured in order to prepare a CSS with larger amplitude.

8.1.2 The experimental setup

In Ch. 4 a detailed discussion of the experimental setup built so far was carried out. We investigated the SHG system and found results which were in line with previous experiments on pulsed SHG. For the tight focusing of the fundamental beam near the Boyd-Kleinman optimum, the conversion efficiency was found to increase rapidly for low pump powers. But for higher pump powers the behaviour of dropping conversion efficiency was observed. These result motivated us to reduce the focusing strength of the fundamental beam. This reduced focusing resulted in slightly lower conversion efficiency for lower pump powers, but no drop in the conversion efficiency was observed. Furthermore the conversion efficiency was always below the saturation point for the measured input powers.

Then we performed a detailed analysis of the parametric downconversion crystal. First we tested the system for parametric interaction between a weak seed beam and a strong pump. We observed amplification/de-amplification values of the weak seed beam of about 0.4/4.5. A model was utilized in an attempt to predict the behaviour of the amplification/de-amplification, Eq. (4.7). This model was unable to replicate the measured values, if the expected experimental parameters were used. If instead a tighter focusing of the pump beam in the model was assumed, it was possible to make the model fit to the experimental data. The possibility of having a tighter focusing of the pump beam than expected was discussed. We believe that a tighter focusing could be a possibility, since we did not have any way of deducing it precisely under the experimental conditions.

We also did a thorough investigation of the system needed for the subtraction of photons. We did a theoretical investigation of the spectra of the downconverted field and from this made estimates of the quality of the filtering. From these calculations it was found that the spectral filtering would result in a limitation on the homodyne efficiency of about 0.8. For this reason we are now trying to implement shorter crystals in the system, since these should give a better spectral purity.

The homodyne detector needed for the characterization of the prepared coherent state superpositions was also investigated in detail. We investigated the gain, filtering, noise characteristics and linearity of the detector. We believe we have found an acceptable compromise between high gain, good noise properties and linearity, which enables the detector to be used in our experiment. We also presented a discussion on the details of pulsed homodyne detection regarding the setting of integration window and optimization of the signal-to-noise ratio.

Finally we presented some experimental results from a squeezing measurement. We

measured squeezing value of up to about 3.0 ± 0.02 dB without any loss-correction. Based on these squeezing measurements we made predictions using our model. From these results we could see that we would need the modal purity to be more than 0.8 in order to have any hopes of observing negativities in the Wigner distribution.

8.2 The results

8.2.1 Photon subtracted states

In Ch. 5 we presented a series of measurements of photon subtracted squeezed states with pump powers of 1, 2, 4, 6 and 8 mW's. Initially we presented a way to infer the phase of the local oscillator needed for the reconstruction. We inferred the phase based on the noise of the measured quantum state by assuming a noise dependence equivalent to that of a squeezed state. This assumption was motivated by the fact that our experimental system should not be able to alter the phase dependence of the noise. We were able to fit the expression in Eq. (5.1) to the noise of our time-traces and from this infer the phase.

Based on this phase inference we carried out the reconstructions for the different measurements. In all reconstructions we took into account the effect of finite homodyne detection efficiency. But even with this correction the states for the lower pump powers did not show any negativity around the origin of the Wigner distribution as expected. This negativity does, however, show up for higher pump powers. We also noticed how the reconstructed states were not elliptical in phase space, but would present a series of kinks and strange peaks.

In order to get rid of these peaks we modified the phase fitting to allow for some optimization. This would remove the kinks and peaks in the Wigner distribution, thus yielding a more clean elliptical shape. Another effect resulting from this was a small increase in the negativity of the Wigner distribution origin. The deepest value observed for these states was $(0,0) = -0.05 \pm 0.01$ after correction for the finite detection efficiency.

8.2.2 Hadamard gate for coherent state superpositions

After this investigation of a series of photon subtracted states we presented a detailed theoretical and experimental investigation of a Hadamard gate for coherent state superpositions. We considered the consequences resulting from the non-orthogonality of the basis states and how this would give rise to a series of Hadamard transforms.

Then we did an investigation of the consequences related to the change of the intrinsic resource of the Hadamard gate to the readily available squeezed state. It was found that for CSS amplitudes, $\alpha \lesssim 1$, the squeezed state would be a good candidate for an alternate resource, with average gate fidelities of more than 90%. Then an experimental investigation was presented. The gate was implemented and tested for the computational basis states $|\pm\alpha\rangle$. The outputs were found to have fidelities of more than 50% with the intended targets, thus confirming the quantum nature of the operation. Then, in order to get information about the gate functionality for arbitrary input we utilized a model built in collaboration with Petr Marek from Olomouc. This model was capable of predicting the gate behaviour for all states on the bloch sphere. The model was capable of making fairly accurate predictions of the results for the input states used to experimentally test the gate, so we believe predictions for other input states can be expected to be accurate as well.

8.2.3 Applications of coherent state superpositions

Finally we presented an investigation and discussion of a number of different protocols for manipulating coherent state superpositions. We presented a protocol for protecting CSS' against decoherence in lossy channels. The protocol was based on a coherent attenuation of the CSS amplitude to an almost vanishing level. The protocol was motivated by the fact that CSS' decohere faster for increasing amplitude, thus making them more vulnerable. Also a first preliminary experimental test of the protocol was presented. The results did quite show the expected behaviour of decreasing amplitude with increasing attenuation. It was however found that the fidelity of the prepared states and an ideal CSS' could remain fairly constant for increasing attenuation. Thus by conditional measurements on the "environment" it is at least possible to prevent the decoherence of the coherent state superpositions. A second protocol under investigation was a protocol for conditionally increasing the content of pure CSS in a decohered mixture. It was found theoretically that the protocol should be capable of "cleaning" up our prepared coherent state superpositions to fidelities well above 50%. The drawbacks of the protocol was also discussed. The most significant drawback is the loss of CSS parity in the protocol. Finally a protocol for transforming an input CSS to an arbitrary state on the Bloch-sphere was presented. Combining these 3 protocols for manipulating coherent state superpositions could potentially open up for the possibility to transmit coherent state superpositions across lossy environments.
As a last idea, a new protocol for entanglement distillation using photon subtraction

was presented. The protocol was based on simple single-mode squeezed states for preparing the initial entangled state. By splitting such a squeezed state on beam splitter a weakly entangled state can be prepared. We found that by performing local displacements and photon subtractions it should be possible to distill states with more entanglement than the standard Bell states.

8.3 Potential routes in the current system

Having discussed the current status of the work relating to our photon subtraction activities we will present a discussion on the potential routes to explore in the immediate future.

8.3.1 Optimizing the purity

In Sec. 4.4 we saw how, by using shorter crystals we should be able to prepare photon subtracted states with higher spectral purity. In Fig. 4.6 it was shown how, going from a 3.0 mm to a 1.5 mm crystal could potentially increase the spectral purity of the prepared signal state from $\approx$ 0.8 to more than 0.9, corresponding to a potential increase in homodyne detection efficiency from 0.9 to more than 0.95. At the same time the spectral overlap with the local oscillator can potentially be increased to almost 1.0 from a current value of less than 0.85. In total we believe this to give a potential increase in homodyne detection efficiency from approximately 0.7 to about 0.9.
A new crystal has recently been installed in the setup and investigations are currently being carried out. Preliminary result suggest that at least the quality of the squeezed states have improved significantly with squeezing/anti-squeezing values of approximately -1.95dB/2.30dB. This should in itself improve the potential quality of any photon-subtracted states.

8.3.2 Testing the suggested protocols

Following a successful implementation of the new crystal and the expected quality improvement of our photon subtracted states, an obvious route of further investigations is the implementation of the protocols suggested in Ch. 7. The first experimental test of the attenuation protocol has already been carried out. These results indicate that the CSS can be manipulated using only Gaussian operations. The next

step will be to improve the quality of this experiment and conclusively show that a CSS can be coherently attenuated.
Then, in the same setup the protocols for purification and rotation of the CSS can be implemented. The main challenge in relation to this is a way to effectively set the phase of local oscillator, since this is a key part in realizing these protocols. Different methods of implementing this are currently being considered and an implementation can potentially begin in the near future.

8.4 Potential routes for expansion of the system

Having a functioning protocol for photon subtraction a natural next step would be the extension with a second subtraction channel. Adding a second APD and a set of displacements would allow for the implementation of the entanglement distillation protocol suggested in Ch. 7. This system would also allow for the potential preparation of coherent state superpositions with larger amplitude as discussed in Ch. 3. The only difference between the two protocols is the choice of the displacements involved.

8.4.1 System for distributing coherent state superpositions

Having coherent state superpositions available a potential experiment would be a combined system with both attenuation, purification and rotations. Such a system could be used to demonstrate a network for distribution of high-quality coherent state superpositions over large distances. This network would be based on preparation, distribution, purification and Bloch-sphere rotations in order to prepare CSS' at distant locations. Such a protocol would need to be combined with a system for increasing the amplitude of the CSS. This could be either based on the protocol investigated in Ch. 3 or the noiseless amplifier suggested by Zavatta *et al.* [171]. This protocol relies on a combination of photon subtrations and additions, thus it would be necessesary to implement a photon addition operation.

8.4.2 Adding single photons to squeezed states

From the work by E. Sudarshan [68] and R. Glauber [69] we have that any classical state can be expressed as a mixture of coherent states. From this it also follows that any classical state will always have a finite vacuum content, unless the excitation tends to infinity. Thus, any state with no vacuum content is a definite non-classical

state. From Eq. (2.21) we have that the $\hat{a}^\dagger$ operator will remove any vacuum content from a state, thus preparing a highly non-classical state. The ability of this operation to turn classical states into non-classical states has been demonstrated for the thermal state [172].
Thus, building a system for adding photons to quantum states is another way to gain access to highly non-classical states. Also, such a system could allow for the implementation of a noiseless amplifier for the coherent state superpositions. Combining this amplifier with the CSS distribution network described before could pave the way for the distribution of large amplitude coherent state superpositions.

8.5 Final remarks

In conclusion this work constitutes an important step towards the potential demonstration of quantum information processing using coherent state superpositions. Combining the results of this work with the constant progress within the field of non-Gaussian states could pave the way to realizing all optical quantum information processing networks and allow for new investigations into the fundamentals of quantum mechanics.

References

[1] E. Schrödinger, "Der stetige Übergang von der Mikro- zur Makromechanik," Die Naturwissenschaften, vol. 14, pp. 664–666, July 1926.

[2] A. Einstein, B. Podolsky, and N. Rosen, "Can Quantum-Mechanical Description of Physical Reality Be Considered Complete?," Physical Review, vol. 47, pp. 777–780, May 1935.

[3] M. D. Reid, P. D. Drummond, E. Cavalcanti, P. K. Lam, H. a. Bachor, U. L. Andersen, and G. Leuchs, "Colloquium: The Einstein-Podolsky-Rosen paradox: From concepts to applications," Reviews of Modern Physics, vol. 81, pp. 1727–1751, Dec. 2009.

[4] D. P. DiVincenzo, "Quantum Computation," Science, vol. 270, pp. 255–261, Oct. 1995.

[5] N. Gisin, G. Ribordy, W. Tittel, and H. Zbinden, "Quantum cryptography," Reviews of Modern Physics, vol. 74, pp. 145–195, Mar. 2002.

[6] V. Giovannetti, S. Lloyd, and L. Maccone, "Advances in quantum metrology," Nature Photonics, vol. 5, pp. 222–229, Apr. 2011.

[7] L. M. K. Vandersypen, M. Steffen, G. Breyta, C. S. C. S. Yannoni, M. H. Sherwood, and I. L. Chuang, "Experimental realization of Shor's quantum factoring algorithm using nuclear magnetic resonance," Nature, vol. 414, no. 6866, pp. 883–887, 2001.

[8] F. Schmidt-Kaler, H. Häffner, M. Riebe, S. Gulde, G. P. T. Lancaster, T. Deuschle, C. Becher, C. F. Roos, J. Eschner, and R. Blatt, "Realization of the Cirac-Zoller controlled NOT- quantum gate," Nature, vol. 422, pp. 408–411, Mar. 2003.

[9] L. Childress, J. Taylor, A. Sørensen, and M. Lukin, "Fault-Tolerant Quantum Communication Based on Solid-State Photon Emitters," Physical Review Letters, vol. 96, p. 070504, Feb. 2006.

[10] B. E. Kane, "A silicon-based nuclear spin quantum computer," Nature, vol. 393, no. 6681, pp. 133–137, 1998.

[11] I. Chiorescu, Y. Nakamura, C. J. P. M. Harmans, and J. E. Mooij, "Coherent quantum dynamics of a superconducting flux qubit.," Science (New York, N.Y.), vol. 299, pp. 1869–71, Mar. 2003.

[12] J. I. Cirac, L. M. Duan, and P. Zoller, "Quantum optical implementation of quantum information processing," arXiv, p. 0405.030, May 2004.

[13] J. L. O'Brien, G. J. Pryde, A. G. White, T. C. Ralph, and D. Branning, "Demonstration of an all-optical quantum controlled-NOT gate," Nature, vol. 426, pp. 264–267, Nov. 2003.

[14] C.-Y. Lu, X.-Q. Zhou, O. Gühne, W.-B. Gao, J. Zhang, Z.-S. Yuan, A. Goebel, T. Yang, and J.-W. Pan, "Experimental entanglement of six photons in graph states," Nature Physics, vol. 3, pp. 91–95, Jan. 2007.

[15] W. Wieczorek, R. Krischek, N. Kiesel, P. Michelberger, G. Tóth, and H. Weinfurter, "Experimental Entanglement of a Six-Photon Symmetric Dicke State," Physical Review Letters, vol. 103, p. 020504, July 2009.

[16] X.-C. Yao, T.-X. Wang, P. Xu, H. Lu, G.-S. Pan, X.-H. Bao, C.-Z. Peng, C.-Y. Lu, Y.-A. Chen, and J.-W. Pan, "Observation of eight-photon entanglement," Nature Photonics, Feb. 2012.

[17] L.-A. Wu, H. J. Kimble, J. Hall, and H. Wu, "Generation of Squeezed States by Parametric Down Conversion," Physical Review Letters, vol. 57, pp. 2520–2523, Nov. 1986.

[18] H. Vahlbruch, M. Mehmet, S. Chelkowski, B. Hage, A. Franzen, N. Lastzka, S. Goßler, K. Danzmann, and R. Schnabel, "Observation of Squeezed Light with 10-dB Quantum-Noise Reduction," Physical Review Letters, vol. 100, no. January, p. 033602, 2008.

[19] Y. Takeno, M. Yukawa, H. Yonezawa, and A. Furusawa, "Observation of -9 dB quadrature squeezing with improvement of phase stability in homodyne measurement," Optics Express, vol. 15, p. 4321, Apr. 2007.

[20] R. Dong, J. Heersink, J. F. Corney, P. D. Drummond, U. L. Andersen, and G. Leuchs, "Experimental evidence for Raman-induced limits to efficient squeezing in optical fibers," Optics Letters, vol. 33, p. 116, Jan. 2008.

[21] M. G. Paris, "Displacement operator by beam splitter," Physics Letters A, vol. 217, pp. 78–80, July 1996.

[22] S. Lloyd, "Coherent quantum feedback," Physical Review A, vol. 62, p. 022108, July 2000.

[23] S. Scheel, W. J. Munro, J. Eisert, K. Nemoto, and P. Kok, "Feed-forward and its role in conditional linear optical quantum dynamics," Physical Review A, vol. 73, p. 034301, Mar. 2006.

[24] H. M. Wiseman and G. J. Milburn, "Quantum theory of optical feedback via homodyne detection," Physical Review Letters, vol. 70, pp. 548–551, Feb. 1993.

[25] A. Furusawa, S. L. Braunstein, J. L. Sørensen, C. a. Fuchs, H. J. Kimble, and E. S. Polzik, "Unconditional Quantum Teleportation," Science, vol. 282, pp. 706–709, Oct. 1998.

[26] F. Grosshans, G. Van Assche, J. Wenger, R. Brouri, N. J. Cerf, and P. Grangier, "Quantum key distribution using gaussian-modulated coherent states.," Nature, vol. 421, pp. 238–41, Jan. 2003.

[27] U. L. Andersen, V. Josse, and G. Leuchs, "Unconditional Quantum Cloning of Coherent States with Linear Optics," Physical Review Letters, vol. 94, p. 240503, June 2005.

[28] A. M. Lance, T. Symul, W. P. Bowen, B. Sanders, T. Tyc, T. C. Ralph, and P. K. Lam, "Continuous-variable quantum-state sharing via quantum disentanglement," Physical Review A, vol. 71, p. 033814, Mar. 2005.

[29] R. Ukai, N. Iwata, Y. Shimokawa, S. Armstrong, A. Politi, J.-i. Yoshikawa, P. van Loock, and A. Furusawa, "Demonstration of Unconditional One-Way Quantum Computations for Continuous Variables," Physical Review Letters, vol. 106, p. 240504, June 2011.

[30] C. Weedbrook, S. Pirandola, R. García-Patrón, N. J. Cerf, T. C. Ralph, J. H. Shapiro, and S. Lloyd, "Gaussian Quantum Information," arXiv, p. 1110.3234, Oct. 2011.

[31] J. Eisert, S. Scheel, and M. B. Plenio, "Distilling Gaussian States with Gaussian Operations is Impossible," Physical Review Letters, vol. 89, p. 137903, Sept. 2002.

[32] J. Fiurášek, "Gaussian Transformations and Distillation of Entangled Gaussian States," Physical Review Letters, vol. 89, p. 137904, Sept. 2002.

[33] G. Giedke and J. Ignacio Cirac, "Characterization of Gaussian operations and distillation of Gaussian states," Physical Review A, vol. 66, p. 032316, Sept. 2002.

[34] J. Niset, J. Fiurášek, and N. J. Cerf, "No-Go Theorem for Gaussian Quantum Error Correction," Physical Review Letters, vol. 102, p. 120501, Mar. 2009.

[35] J. Bell, Speakable and Unspeakable in Quantum Mechanics. Cambridge University Press, 1987.

[36] S. Lloyd and S. L. Braunstein, "Quantum Computation over Continuous Variables," Physical Review Letters, vol. 82, pp. 1784–1787, Feb. 1999.

[37] M. Ohliger, K. Kieling, and J. Eisert, "Limitations of quantum computing with Gaussian cluster states," Physical Review A, vol. 82, p. 042336, Oct. 2010.

[38] L. Magnin, F. Magniez, A. Leverrier, and N. J. Cerf, "Strong no-go theorem for Gaussian quantum bit commitment," Physical Review A, vol. 81, p. 010302, Jan. 2010.

[39] N. Menicucci, P. van Loock, M. Gu, C. Weedbrook, T. C. Ralph, and M. a. Nielsen, "Universal Quantum Computation with Continuous-Variable Cluster States," Physical Review Letters, vol. 97, p. 110501, Sept. 2006.

[40] A. Ourjoumtsev, R. Tualle-brouri, P. Grangier, and A. Dantan, "Increasing entanglement between Gaussian states by coherent photon subtraction," Physical Review Letters, vol. 98, p. 030502, Jan. 2007.

[41] H. Takahashi, J. S. Neergaard-Nielsen, M. Takeuchi, M. Takeoka, K. Hayasaka, A. Furusawa, and M. Sasaki, "Entanglement distillation from Gaussian input states," Nature Photonics, vol. 4, pp. 178–181, Feb. 2010.

[42] M. Lassen, M. Sabuncu, A. Huck, J. Niset, G. Leuchs, N. J. Cerf, and U. L. Andersen, "Quantum optical coherence can survive photon losses using

a continuous-variable quantum erasure-correcting code," Nature Photonics, vol. 4, pp. 700–705, July 2010.

[43] T. C. Ralph, A. Gilchrist, G. J. Milburn, W. J. Munro, and S. Glancy, "Quantum computation with optical coherent states," Physical Review A, vol. 68, p. 042319, Oct. 2003.

[44] A. P. Lund, H. Jeong, T. C. Ralph, and M. Kim, "Conditional production of superpositions of coherent states with inefficient photon detection," Physical Review A, vol. 70, p. 020101, Aug. 2004.

[45] A. Gilchrist, K. Nemoto, W. J. Munro, T. C. Ralph, S. Glancy, S. L. Braunstein, and G. J. Milburn, "Schrödinger cats and their power for quantum information processing," Journal of Optics B: Quantum and Semiclassical Optics, vol. 6, pp. S828–S833, Aug. 2004.

[46] T. C. Ralph, "Quantum error correction of continuous-variable states against Gaussian noise," Physical Review A, vol. 84, p. 022339, Aug. 2011.

[47] R. García-Patrón, J. Fiurášek, N. J. Cerf, J. Wenger, R. Tualle-Brouri, and P. Grangier, "Proposal for a Loophole-Free Bell Test Using Homodyne Detection," Physical Review Letters, vol. 93, p. 130409, Sept. 2004.

[48] A. Mandilara and N. J. Cerf, "Quantum bit commitment under Gaussian constraints," arXiv, p. 1105.2140, May 2011.

[49] A. Lvovsky, H. Hansen, T. Aichele, O. Benson, J. Mlynek, and S. Schiller, "Quantum State Reconstruction of the Single-Photon Fock State," Physical Review Letters, vol. 87, p. 50402, July 2001.

[50] A. Ourjoumtsev, R. Tualle-Brouri, J. Laurat, and P. Grangier, "Generating optical Schrödinger kittens for quantum information processing.," Science, vol. 312, pp. 83–6, Apr. 2006.

[51] J. S. Neergaard-Nielsen, B. Nielsen, C. Hettich, K. Mø lmer, and E. S. Polzik, "Generation of a Superposition of Odd Photon Number States for Quantum Information Networks," Physical Review Letters, vol. 97, p. 83604, Aug. 2006.

[52] M. Dakna, T. Anhut, T. Opatrný, L. Knöll, and D.-G. Welsch, "Generating Schrödinger-cat-like states by means of conditional measurements on a beam splitter," Physical Review A, vol. 55, pp. 3184–3194, Apr. 1997.

[53] L. Ballentine, "The Statistical Interpretation of Quantum Mechanics," Reviews of Modern Physics, vol. 42, pp. 358–381, Oct. 1970.

[54] L. E. Ballentine, Quantum Mechanics, A Modern Development. World Scientific, 1st ed., 1998.

[55] C. Helstrom, Quantum Detection and Estimation Theory. Academic Press, New York, 1976.

[56] R. Jozsa, "Fidelity for Mixed Quantum States," Journal of Modern Optics, vol. 41, pp. 2315–2323, Dec. 1994.

[57] R. Loudon, The Quantum Theory of Light. Oxford Science Publications, Oxford Univeristy Press, 3rd ed., 2000.

[58] J. J. Sakurai, Modern Quantum Mechanics Revised Edition. Addison-Wesley Publishing Company, Inc., 1994.

[59] G. Christiansen, E. Both, and P. s. Sørensen, Mekanik. Institut for Fysik, Danmarks Tekniske Universitet, 2002.

[60] E. Wigner, "On the Quantum Correction For Thermodynamic Equilibrium," Physical Review, vol. 40, pp. 749–759, June 1932.

[61] J. Bertrand and P. Bertrand, "A tomographic approach to Wigner's function," Foundations of Physics, vol. 17, pp. 397–405, Apr. 1987.

[62] S. L. Braunstein and P. van Loock, "Quantum information with continuous variables," Reviews of Modern Physics, vol. 77, pp. 1–65, Oct. 2004.

[63] H. Benichi, S. Takeda, N. Lee, and A. Furusawa, "Quantum teleportation of nonclassical wave packets: An effective multimode theory," Physical Review A, vol. 84, p. 012308, July 2011.

[64] U. Leonhardt, Measuring the Quantum State of Light. Cambridge University Press, 1997.

[65] J. S. Neergaard-Nielsen, Generation of single photons and Schrödinger kitten states of light Ph PhD thesis, 2008.

[66] M. Mehmet, H. Vahlbruch, N. Lastzka, K. Danzmann, and R. Schnabel, "Observation of squeezed states with strong photon-number oscillations," Physical Review A, vol. 81, p. 013814, Jan. 2010.

[67] R. Filip and L. Mišta, "Detecting Quantum States with a Positive Wigner Function beyond Mixtures of Gaussian States," Physical Review Letters, vol. 106, p. 200401, May 2011.

[68] E. Sudarshan, "Equivalence of Semiclassical and Quantum Mechanical Descriptions of Statistical Light Beams," Physical Review Letters, vol. 10, pp. 277–279, Apr. 1963.

[69] R. Glauber, "Coherent and Incoherent States of the Radiation Field," Physical Review, vol. 131, pp. 2766–2788, Sept. 1963.

[70] P. Schleich, Quantum Optics in Phase Space. Wiley-VCH Verlag Berlin GmbH, Berlin, 2001.

[71] R. Hudson, "When is the wigner quasi-probability density non-negative?," Reports on Mathematical Physics, vol. 6, pp. 249–252, Oct. 1974.

[72] A. Zavatta, S. Viciani, and M. Bellini, "Tomographic reconstruction of the single-photon Fock state by high-frequency homodyne detection," Physical Review A, vol. 70, p. 053821, Nov. 2004.

[73] A. Ourjoumtsev, R. Tualle-Brouri, and P. Grangier, "Quantum Homodyne Tomography of a Two-Photon Fock State," Physical Review Letters, vol. 96, p. 213601, June 2006.

[74] E. Schrödinger, "Die gegenäwrtige Situation in der Quantenmechanik," Die Naturwissenschaften, vol. 23, pp. 807–812, Nov. 1935.

[75] H. Yuen and J. Shapiro, "Optical communication with two-photon coherent states–Part I: Quantum-state propagation and quantum-noise," IEEE Transactions on Information Theory, vol. 24, pp. 657–668, Nov. 1978.

[76] B. Yurke and D. Stoler, "Generating quantum mechanical superpositions of macroscopically distinguishable states via amplitude dispersion," Physical Review Letters, vol. 57, no. 1, p. 13, 1986.

[77] D. J. Griffths, Introduction to Electrodynamics. Prentice Hall, third edit ed., 1999.

[78] P. N. Butcher and D. Cotter, The Elements of Nonlinear Optics. Cambrigde Studies in Modern Optics, Cambridge University Press, 1990.

[79] R. D. L. Kronig, "On the Theory of Dispersion of X-Rays," Journal of the Optical Society of America, vol. 12, p. 547, June 1926.

[80] J. Toll, "Causality and the Dispersion Relation: Logical Foundations," Physical Review, vol. 104, pp. 1760–1770, Dec. 1956.

[81] G. D. Boyd and D. A. Kleinman, "Parametric Interaction of Focused Gaussian Light Beams," Journal of Applied Physics, vol. 39, no. 8, p. 3597, 1968.

[82] A. Bahabad, A. Ganany-Padowicz, and A. Arie, "Engineering two-dimensional nonlinear photonic quasi-crystals.," Optics letters, vol. 33, pp. 1386–8, June 2008.

[83] A. Bahabad, N. Voloch-Bloch, and A. Arie, "Analysis of Colinear Quasi-Phase-Matching in Nonlinear Photonic Crystals," IEEE Journal of Quantum Electronics, vol. 44, pp. 638–644, July 2008.

[84] a. Bahabad, R. Lifshitz, N. Voloch-Bloch, and A. Arie, "Nonlinear photonic quasicrystals for novel optical devices," Philosophical Magazine, vol. 88, pp. 2285–2293, May 2008.

[85] R. Lifshitz, A. Arie, and A. Bahabad, "Photonic Quasicrystals for Nonlinear Optical Frequency Conversion," Physical Review Letters, vol. 95, p. 133901, Sept. 2005.

[86] K. Fradkin-Kashi, A. Arie, P. Urenski, and G. Rosenman, "Multiple Nonlinear Optical Interactions with Arbitrary Wave Vector Differences," Physical Review Letters, vol. 88, p. 023903, Dec. 2001.

[87] A. Arie, N. Habshoosh, and A. Bahabad, "Quasi phase matching in two-dimensional nonlinear photonic crystals," Optical and Quantum Electronics, vol. 39, pp. 361–375, June 2007.

[88] T. Gerrits, S. Glancy, T. Clement, B. Calkins, A. Lita, A. Miller, A. Migdall, S. W. Nam, R. P. Mirin, and E. Knill, "Generation of optical coherent-state superpositions by number-resolved photon subtraction from the squeezed vacuum," Physical Review A, vol. 82, p. 31802, Sept. 2010.

[89] N. Namekata, Y. Takahashi, G. Fujii, D. Fukuda, S. Kurimura, and S. Inoue, "Non-Gaussian operation based on photon subtraction using a photon-number-resolving detector at a telecommunications wavelength," Nature Photonics, vol. 4, pp. 655–660, July 2010.

[90] A. Lvovsky and M. G. Raymer, "Continuous-variable optical quantum-state tomography," Reviews of Modern Physics, vol. 81, pp. 299–332, Mar. 2009.

[91] H.-A. Bachor and T. C. Ralph, A Guide to Experiments in Quantum Optics. Wiley-VCH Verlag Berlin GmbH, Berlin, 2004.

[92] K. Vogel and H. Risken, "Determination of quasiprobability distributions in terms of probability distributions for the rotated quadrature phase," Physical Review A, vol. 40, pp. 2847–2849, Sept. 1989.

[93] Z. Hradil, "Quantum-state estimation," Physical Review A, vol. 55, pp. R1561–R1564, Mar. 1997.

[94] K. Banaszek, G. D'Ariano, M. Paris, and M. Sacchi, "Maximum-likelihood estimation of the density matrix," Physical Review A, vol. 61, p. 010304, Dec. 1999.

[95] M. Ježek, J. Fiurášek, and Z. Hradil, "Quantum inference of states and processes," Physical Review A, vol. 68, p. 012305, July 2003.

[96] A. Lvovsky, "Iterative maximum-likelihood reconstruction in quantum homodyne tomography," Journal of Optics B: Quantum and Semiclassical Optics, vol. 6, pp. S556–S559, June 2004.

[97] J. Fiurášek, "Maximum-likelihood estimation of quantum measurement," Physical Review A, vol. 64, p. 024102, July 2001.

[98] J. Řeháček, Z. Hradil, E. Knill, and A. Lvovsky, "Diluted maximum-likelihood algorithm for quantum tomography," Physical Review A, vol. 75, p. 042108, Apr. 2007.

[99] R. W. Boyd, "Order-of-magnitude estimates of the nonlinear optical susceptibility," Journal of Modern Optics, vol. 46, pp. 367–378, Mar. 1999.

[100] H. Chrzanowski, J. Bernu, B. Sparkes, B. Hage, A. P. Lund, T. C. Ralph, P. K. Lam, and T. Symul, "Photon-number discrimination without a photon counter and its application to reconstructing non-Gaussian states," Physical Review A, vol. 84, p. 050302, Nov. 2011.

[101] H. Jeong, A. P. Lund, and T. C. Ralph, "Production of superpositions of coherent states in traveling optical fields with inefficient photon detection," Physical Review A, vol. 72, p. 013801, July 2005.

[102] A. P. Lund and T. C. Ralph, "Coherent-state linear optical quantum computing gates using simplified diagonal superposition resource states," Physical Review A, vol. 71, p. 032305, Mar. 2005.

[103] S. R. Huisman, N. Jain, S. A. Babichev, F. Vewinger, A. N. Zhang, S. H. Youn, and a.I. Lvovsky, "Instant single-photon Fock state tomography," Optics Letters, vol. 34, p. 2739, Sept. 2009.

[104] J. Wenger, R. Tualle-Brouri, and P. Grangier, "Non-Gaussian Statistics from Individual Pulses of Squeezed Light," Physical Review Letters, vol. 92, p. 153601, Apr. 2004.

[105] R. Tualle-Brouri, A. Ourjoumtsev, A. Dantan, P. Grangier, M. Wubs, and A. S. Sørensen, "Multimode model for projective photon-counting measurements," Physical Review A, vol. 80, p. 013806, July 2009.

[106] T. Bröcker and R. F. Werner, "Mixed states with positive Wigner functions," Journal of Mathematical Physics, vol. 36, no. 1, p. 62, 1995.

[107] a. Mandilara, E. Karpov, and N. Cerf, "Extending Hudson's theorem to mixed quantum states," Physical Review A, vol. 79, p. 062302, June 2009.

[108] A. La Porta and R. Slusher, "Squeezing limits at high parametric gains," Physical Review A, vol. 44, pp. 2013–2022, Aug. 1991.

[109] M. Kim, E. Park, P. Knight, and H. Jeong, "Nonclassicality of a photon-subtracted Gaussian field," Physical Review A, vol. 71, p. 043805, Apr. 2005.

[110] S. Suzuki, K. Tsujino, F. Kannari, and M. Sasaki, "Analysis on generation schemes of Schrödinger cat-like states under experimental imperfections," Optics Communications, vol. 259, pp. 758–764, Mar. 2006.

[111] K. Mølmer, "Non-Gaussian states from continuous-wave Gaussian light sources," Physical Review A, vol. 73, p. 063804, June 2006.

[112] A. Ourjoumtsev, Étude Théorique et Expérimentale de Superpositions Quantiques Cohérentes PhD thesis, 2007.

[113] K. Wakui, H. Takahashi, A. Furusawa, and M. Sasaki, "Photon subtracted squeezed states generated with periodically poled KTiOPO_4," Optics Express, vol. 15, p. 3568, Mar. 2007.

[114] A. Nielsen and K. Mølmer, "Transforming squeezed light into a large-amplitude coherent-state superposition," Physical Review A, vol. 76, p. 043840, Oct. 2007.

[115] H. Takahashi, K. Wakui, S. Suzuki, M. Takeoka, K. Hayasaka, A. Furusawa, and M. Sasaki, "Generation of Large-Amplitude Coherent-State Superposition via Ancilla-Assisted Photon Subtraction," Physical Review Letters, vol. 101, p. 233605, Dec. 2008.

[116] J. Brask, I. Rigas, E. Polzik, U. L. Andersen, and A. Sø rensen, "Hybrid Long-Distance Entanglement Distribution Protocol," Physical Review Letters, vol. 105, p. 160501, Oct. 2010.

[117] A. Zavatta, S. Viciani, and M. Bellini, "Non-classical field characterization by high-frequency, time-domain quantum homodyne tomography," Laser Physics Letters, vol. 3, pp. 3–16, Jan. 2006.

[118] H. Hansen, T. Aichele, C. Hettich, P. Lodahl, A. Lvovsky, J. Mlynek, and S. Schiller, "Ultrasensitive pulsed, balanced homodyne detector: application to time-domain quantum measurements," Optics Letters, vol. 26, p. 1714, Nov. 2001.

[119] Y.-M. Chi, B. Qi, W. Zhu, L. Qian, H.-K. Lo, S.-H. Youn, A. Lvovsky, and L. Tian, "A balanced homodyne detector for high-rate Gaussian-modulated coherent-state quantum key distribution," New Journal of Physics, vol. 13, p. 013003, Jan. 2011.

[120] J. Comly and E. Garmire, "Second Harmonic Generation from Short Pulses," Applied Physics Letters, vol. 12, no. 1, pp. 7–9, 1968.

[121] a. M. Weiner, a. M. Kan'an, and D. E. Leaird, "High-efficiency blue generation by frequency doubling of femtosecond pulses in a thick nonlinear crystal.," Optics letters, vol. 23, pp. 1441–3, Sept. 1998.

[122] J. Armstrong, N. Bloembergen, J. Ducuing, and P. Pershan, "Interactions between Light Waves in a Nonlinear Dielectric," Physical Review, vol. 127, pp. 1918–1939, Sept. 1962.

[123] K. Kato and E. Takaoka, "Sellmeier and thermo-optic dispersion formulas for KTP," Applied Optics, vol. 41, pp. 5040–5044, Aug. 2002.

[124] D. Guzun, Y.-q. Li, and M. Xiao, "Blue light generation in single-pass frequency doubling of femtosecond pulses in KNbO3," Optics Communications, vol. 180, pp. 367–371, June 2000.

[125] J. Wenger, R. Tualle-Brouri, and P. Grangier, "Pulsed homodyne measurements of femtosecond squeezed pulses generated by single-pass parametric deamplification," Optics Letters, vol. 29, p. 1267, June 2004.

[126] B. Yurke, P. Grangier, R. Slusher, and M. Potasek, "Generating and detecting short-duration pulses of squeezed light," Physical Review A, vol. 35, pp. 3586–3589, Apr. 1987.

[127] R. Slusher, P. Grangier, A. LaPorta, B. Yurke, and M. J. Potasek, "Pulsed Squeezed Light," Physical Review Letters, vol. 59, pp. 2566–2569, Nov. 1987.

[128] J. P. Gordon, W. Louisell, and L. Walker, "Quantum Fluctuations and Noise in Parametric Processes. II," Physical Review, vol. 129, pp. 481–485, Jan. 1963.

[129] W. Wagner and R. Hellwarth, "Quantum Noise in a Parametric Amplifier with Lossy Modes," Physical Review, vol. 133, pp. A915–A920, Feb. 1964.

[130] R. Byer and S. Harris, "Power and Bandwidth of Spontaneous Parametric Emission," Physical Review, vol. 168, pp. 1064–1068, Apr. 1968.

[131] C. Kim, R.-D. Li, and P. Kumar, "Deamplification response of a traveling-wave phase-sensitive optical parametric amplifier," Optics Letters, vol. 19, p. 132, Jan. 1994.

[132] M. Werner, M. Raymer, M. Beck, and P. Drummond, "Ultrashort pulsed squeezing by optical parametric amplification," Physical Review A, vol. 52, pp. 4202–4213, Nov. 1995.

[133] E. M. Daly and a. I. Ferguson, "Spatial and temporal dependence of single-pass parametric gain," Journal of Modern Optics, vol. 48, pp. 729–744, Mar. 2001.

[134] M. Milton and T. McIlveen, "A high-gain diffraction-limited lithium niobate optical parametric amplifier," Optics Communications, vol. 82, pp. 153–161, Apr. 1991.

[135] J. G. Rarity, P. R. Tapster, J. a. Levenson, J. C. Garreau, I. Abram, J. Mertz, T. Debuisschert, A. Heidmann, C. Fabre, and E. Giacobino, "Quantum correlated twin beams," Applied Physics B Photophysics and Laser Chemistry, vol. 55, pp. 250–257, Sept. 1992.

[136] T. Hirano, K. Kotani, T. Ishibashi, S. Okude, and T. Kuwamoto, "3 dB squeezing by single-pass parametric amplification in a periodically poled KTiOPO4 crystal," Optics Letters, vol. 30, p. 1722, July 2005.

[137] B. E. A. Saleh and M. C. Teich, Fundamentals of Photonics. Wiley Series in Pure and Applied Optics, Wiley Interscience, 1991.

[138] T. Aichele, a.I. Lvovsky, and S. Schiller, "Optical mode characterization of single photons prepared by means of conditional measurements on a biphoton state," The European Physical Journal D - Atomic, Molecular and Optical Physics, vol. 18, pp. 237–245, Feb. 2002.

[139] a. B. U'Ren, K. Banaszek, and I. a. Walmsley, "Photon engineering for quantum information processing," arXiv, p. 0305.192, May 2003.

[140] R. Horodecki, M. Horodecki, and K. Horodecki, "Quantum entanglement," Reviews of Modern Physics, vol. 81, pp. 865–942, June 2009.

[141] J. Appel, D. Hoffman, E. Figueroa, and A. Lvovsky, "Electronic noise in optical homodyne tomography," Physical Review A, vol. 75, p. 035802, Mar. 2007.

[142] R. Kumar, E. Barrios, A. MacRae, E. Cairns, E. H. Huntington, and A. Lvovsky, "Versatile Wideband Balanced Detector for Quantum Optical Homodyne Tomography," arXiv, p. 1111.4012, Nov. 2011.

[143] S. M. Lea, Mathematics for Physicists. Brooks/Cole-Thomson Learning, 2004.

[144] M. Bellini, A. S. Coelho, S. N. Filippov, V. I. Man'ko, and A. Zavatta, "Towards higher precision and operational use of optical homodyne tomograms," arXiv, p. 1203.2974, Mar. 2012.

[145] A. P. Lund, T. C. Ralph, and H. Haselgrove, "Fault-Tolerant Linear Optical Quantum Computing with Small-Amplitude Coherent States," Physical Review Letters, vol. 100, p. 30503, Jan. 2008.

[146] P. Kok, K. Nemoto, T. C. Ralph, J. P. Dowling, and G. J. Milburn, "Linear optical quantum computing with photonic qubits," Reviews of Modern Physics, vol. 79, pp. 135–174, Jan. 2007.

[147] R. Raussendorf and H. J. Briegel, "A One-Way Quantum Computer," Physical Review Letters, vol. 86, pp. 5188–5191, May 2001.

[148] R. Raussendorf, D. E. Browne, and H. J. Briegel, "Measurement-based quantum computation on cluster states," Physical Review A, vol. 68, p. 22312, Aug. 2003.

[149] E. Knill, R. Laflamme, and G. J. Milburn, "A scheme for efficient quantuim computation with linear optics," Nature, vol. 409, pp. 46–52, Jan. 2001.

[150] R. Ukai, J.-i. Yoshikawa, N. Iwata, P. van Loock, and A. Furusawa, "Universal linear Bogoliubov transformations through one-way quantum computation," Physical Review A, vol. 81, p. 032315, Mar. 2010.

[151] R. Ukai, S. Yokoyama, J.-i. Yoshikawa, P. van Loock, and A. Furusawa, "Demonstration of a Controlled-Phase Gate for Continuous-Variable One-Way Quantum Computation," Physical Review Letters, vol. 107, p. 250501, Dec. 2011.

[152] P. Marek and J. Fiurášek, "Elementary gates for quantum information with superposed coherent states," Physical Review A, vol. 82, p. 14304, July 2010.

[153] A. Tipsmark, R. Dong, A. Laghaout, P. Marek, M. Ježek, and U. L. Andersen, "Experimental demonstration of a Hadamard gate for coherent state qubits," Physical Review A, vol. 84, p. 050301, Nov. 2011.

[154] J. S. Neergaard-Nielsen, M. Takeuchi, K. Wakui, H. Takahashi, K. Hayasaka, M. Takeoka, and M. Sasaki, "Optical Continuous-Variable Qubit," Physical Review Letters, vol. 105, p. 053602, July 2010.

[155] J. Fiurášek, "Improving entanglement concentration of Gaussian states by local displacements," Physical Review A, vol. 84, p. 012335, July 2011.

[156] S. Suzuki, M. Takeoka, M. Sasaki, U. L. Andersen, and F. Kannari, "Practical purification scheme for decohered coherent-state superpositions via partial homodyne detection," Physical Review A, vol. 73, p. 042304, Apr. 2006.

[157] S. A. Babichev, B. Brezger, and A. Lvovsky, "Remote Preparation of a Single-Mode Photonic Qubit by Measuring Field Quadrature Noise," Physical Review Letters, vol. 92, p. 047903, Jan. 2004.

[158] A. Ourjoumtsev, H. Jeong, R. Tualle-Brouri, and P. Grangier, "Generation of Optical "Schrï¿½dinger Cats" from Photon Number Stataes," Nature, vol. 448, pp. 784–786, Aug. 2007.

[159] H. Ollivier and W. H. Zurek, "Quantum Discord: A Measure of the Quantumness of Correlations," Physical Review Letters, vol. 88, p. 017901, Dec. 2001.

[160] J. Fiurášek, L. Mišta, and R. Filip, "Entanglement concentration of continuous-variable quantum states," Physical Review A, vol. 67, p. 022304, Feb. 2003.

[161] J. Eisert, D. E. Browne, S. Scheel, and M. B. Plenio, "Distillation of continuous-variable entanglement with optical means," Annals of Physics, vol. 311, pp. 431–458, June 2004.

[162] J. Eisert, M. B. Plenio, D. E. Browne, S. Scheel, and a. Feito, "On the experimental feasibility of continuous-variable optical entanglement distillation," Optics and Spectroscopy, vol. 103, pp. 173–177, Aug. 2007.

[163] R. Dong, M. Lassen, J. Heersink, C. Marquardt, R. Filip, G. Leuchs, and U. L. Andersen, "Experimental entanglement distillation of mesoscopic quantum states," Nature Physics, vol. 4, pp. 919–923, Nov. 2008.

[164] T. Opatrný, G. Kurizki, and D.-G. Welsch, "Improvement on teleportation of continuous variables by photon subtraction via conditional measurement," Physical Review A, vol. 61, p. 032302, Feb. 2000.

[165] S. L. Zhang and P. van Loock, "Distillation of mixed-state continuous-variable entanglement by photon subtraction," Physical Review A, vol. 82, p. 062316, Dec. 2010.

[166] S. Zhang and P. van Loock, "Local Gaussian operations can enhance continuous-variable entanglement distillation," arXiv, p. 1103.4500, Mar. 2011.

[167] K. Å»yczkowski, A. Sanpera, and M. Lewenstein, "Volume of the set of separable states," Physical Review A, vol. 58, pp. 883–892, Aug. 1998.

[168] G. Vidal and R. F. Werner, "Computable measure of entanglement," Physical Review A, vol. 65, p. 032314, Feb. 2002.

[169] M. B. Plenio, "Logarithmic Negativity: A Full Entanglement Monotone That is not Convex," Physical Review Letters, vol. 95, p. 090503, Aug. 2005.

[170] M. B. Plenio and S. Virmani, "An introduction to entanglement measures," arXiv, p. 0504.163, Apr. 2005.

[171] A. Zavatta, J. Fiurášek, and M. Bellini, "A high-fidelity noiseless amplifier for quantum light states," Nature Photonics, vol. 5, pp. 52–60, Nov. 2010.

[172] A. Zavatta, S. Viciani, and M. Bellini, "Quantum-to-classical transition with single-photon-added coherent states of light.," Science, vol. 306, pp. 660–2, Oct. 2004.

Appendix A

Appendix

A.1 The homodyne detector

A.1.1 Filter functions

The design of the high-pass and low-pass filters for the homodyne detector are depicted in Fig. A.1.1

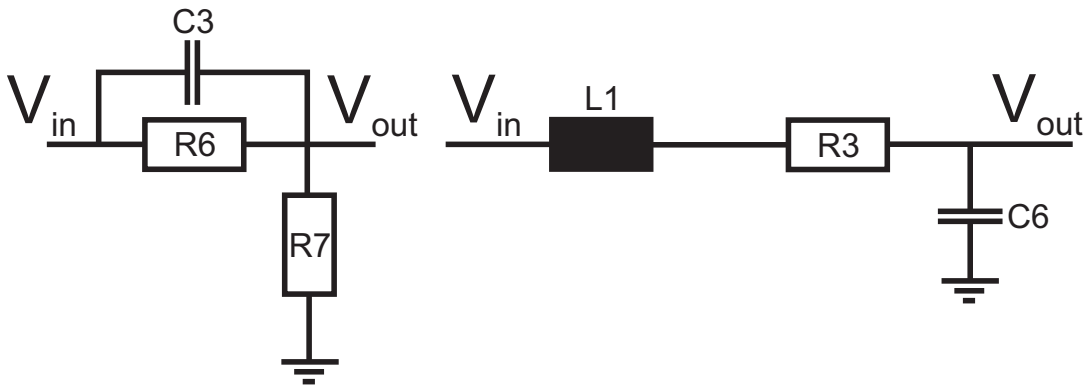

From Fig. A.1.1 we can derive functions for the filter performance based on ideal AC components. The filter function for the high-pass filter is Eq. (A.1).

$$\eta_{HP} = \frac{R_7}{\sqrt{\left(R_7 + \frac{1}{R_6\left(\frac{1}{R_6^2}+\omega^2 C_3^2\right)}\right)^2 + \frac{\omega^2 C^2}{\left(\frac{1}{R_6^2}+\omega^2 C_3^2\right)^2}}} \tag{A.1}$$

The filter function for the low-pass filter is Eq. (A.2).

$$\eta_{LP} = \frac{1}{\omega C_6 \sqrt{R_3^2 + \left(\omega L_1 - \frac{1}{\omega C_3}\right)^2}} \tag{A.2}$$

The curves depicted in Fig. 4.8 are calculated for various component configurations. The component configurations and their corresponding 3-dB frequencies are listed in Tables A.1 and A.2 The complete detector circuit is shown in Fig. A.1.1.

	$R_7 = 1\text{k}\Omega$	$R_7 = 4.7\text{k}\Omega$
$C_3 = 150\text{pF}$	$f_c = 600\text{kHz}$	$f_c = 150\text{kHz}$
$C_3 = 470\text{pF}$	$f_c = 200\text{kHz}$	$f_c < 100\text{kHz}$

Tab. A.1: Component values and resulting 3-dB cut-off frequencies for the high-pass filter. The last resistor is kept constant, $R_6 = 3.3\text{M}\Omega$

	$L_1 = 47\mu\text{H}$	$L_1 = 22\mu\text{H}$
$C_6 = 150\text{pF}$	$f_c = 2.5\text{MHz}$	$f_c = 3\text{MHz}$
$C_6 = 470\text{pF}$	$f_c = 1\text{MHz}$	$f_c = 1\text{MHz}$

Tab. A.2: Component values and resulting 3-dB cut-on frequencies for the low-pass filter. The last resistor is kept constant, $R_3 = 680\Omega$

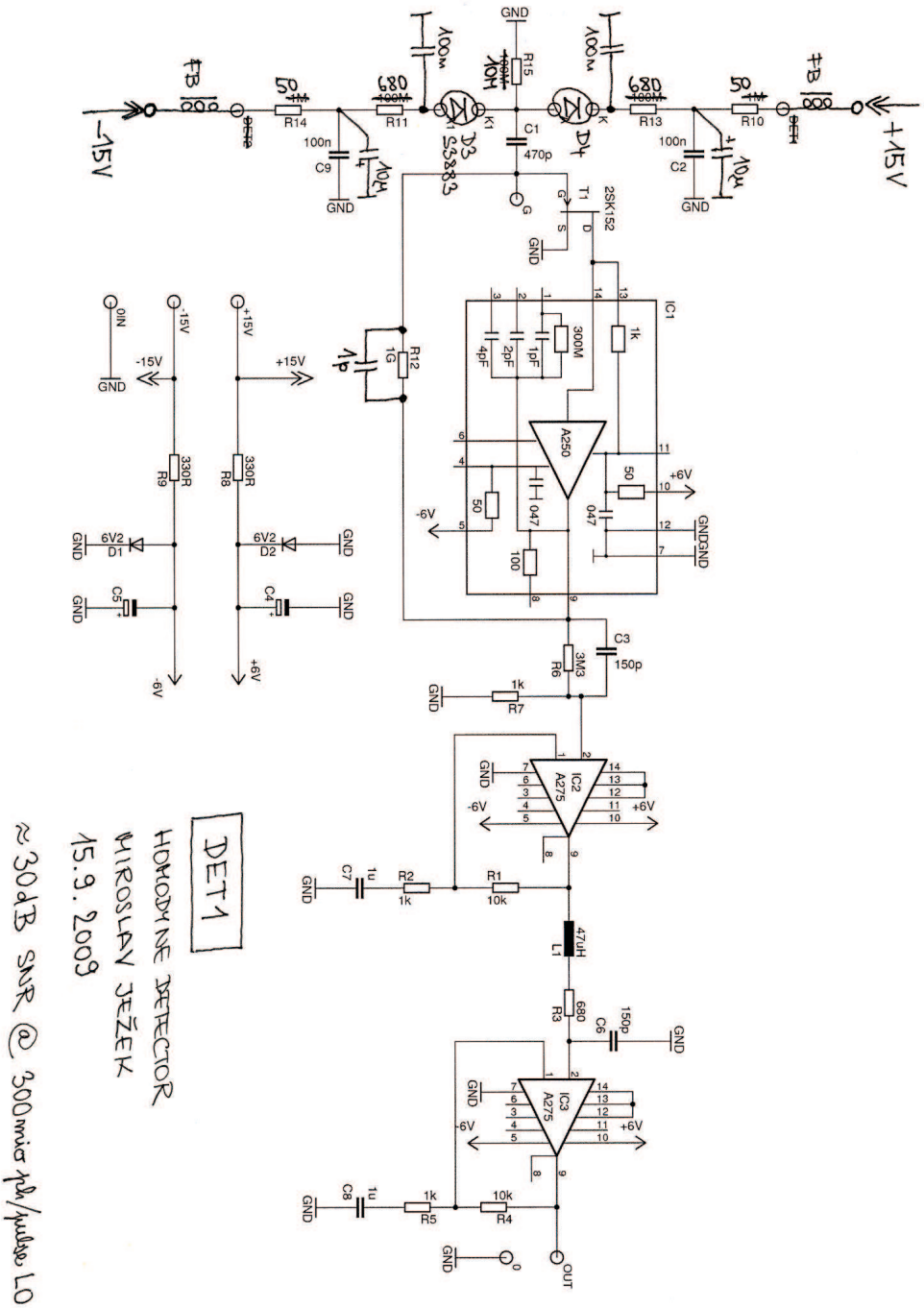
DET1
HOMODYNE DETECTOR
MIROSLAV JEŽEK
15.9.2009
≈30dB SNR @ 300mio ph/pulse LO
-15V
+15V
GND
R14
R11
R15
R13
R10
C9
C2
C1
470p
D3
D4
T1
2SK152
IC1
A250
R12
1G
300M
4pF
2pF
1pF
1k
50
100
047
+6V
-6V
R9
330R
R8
330R
D1
D2
6V2
C5
C4
R6
3M3
C3
150p
R7
IC2
A275
C7
1u
R2
1k
R1
10k
L1
47uH
R3
680
C6
IC3
C8
R5
R4
OUT